ISAS - INTERNATIONAL SCHOOL
FOR ADVANCED STUDIES

MOLECULAR DYNAMICS STUDIES OF GOLD: BULK, DEFECTS, SURFACES AND CLUSTERS

Thesis submitted for the degree of
"Doctor Philosophiae"

CANDIDATE
Furio Ercolessi

SUPERVISORS
Prof. Erio Tosatti
Prof. Michele Parrinello

December 1987

TRIESTE

SISSA - SCUOLA
INTERNAZIONALE
SUPERIORE
STUDI AVANZATI
TRIESTE
Strada Costiera 11

International School for Advanced Studies
Trieste

MOLECULAR DYNAMICS STUDIES OF GOLD: BULK, DEFECTS, SURFACES AND CLUSTERS

Thesis submitted for the degree of
"Doctor Philosophiae"

CANDIDATE
Furio Ercolessi

SUPERVISORS
Prof. Erio Tosatti
Prof. Michele Parrinello

December 1987

Contents

Introduction

In recent years, computer simulation methods have provided much insight into several structural, dynamical and thermal properties of solids and liquids. Computational methods are particularly well suited to the study of low symmetry systems (e.g., defects, surfaces, clusters), where the complexity of analytical treatments may become overwhelming, and of systems at finite temperature.

The key ingredients in computer simulations are interatomic forces. The problem we wish to solve can be simply stated as follows: given a set of N atoms having some positions $r_1 \dots r_N$ and linear momenta $p_1 \dots p_N$, what forces will they experience ? Calculating these forces *ab initio* is a very difficult task. Even if we are not interested in the electronic properties of the system, but only in ionic properties (e.g., vibrations, equilibrium structures, etc.), we must generally take into full account the electronic aspect of the problem.

In the Born-Oppenheimer adiabatic approximation [1], the forces can be obtained by considering the nuclei as fixed and searching for the minimum energy state of the electronic system. This may be done using the Hartree-Fock approximation, or in a density functional theory framework. The force acting on a nucleus is then determined as the gradient of the total energy respect to a displacement of that nucleus. After all nuclei have been moved accordingly to the forces computed in this way, the whole process may be iterated for the new configuration, thus performing a dynamical calculation. This approach, however, is computationally extremely expensive, and not feasible when the number of particles is of the order of ten or more.

Much effort is presently being spent in devising more efficient first-principle schemes. One of them is the recently appeared Car-Parrinello method [2]. In this scheme, the time evolution of a system containing nuclei and electrons is followed by using an unified Lagrangian equation of motion where the electrons are treated within the frame of density functional theory. However, even using present-day supercomputers, it is not possible to follow this approach in problems involving a large number of particles (of the order of several hundreds or thousands) or long simulation times (of the order of 10^{-9} s), due to the great amount of computations required for each configuration. This is especially true for transition or noble metals, where the simultaneous presence of core, valence and conduction electrons calls for a very finely grained mesh to represent adequately the rapid variations of the electron density in the material.

Therefore, there is still a need for simple empirical calculational schemes, where the atoms are treated as points interacting through some total potential energy function

$$V = V(\vec{r}_1, \vec{r}_2, \ldots, \vec{r}_N).$$

Here, the electrons do not appear explicitly, but of course their presence is reflected in the form of V.

The simplest choice consist of writing V as a sum of pairwise interactions between the atoms. The simplicity of two-body forces makes them particularly appealing for use in computer simulations, and in fact a very large number of "computer experiments" with pairwise interactions have been performed in the last two decades.

Two-body interactions, however, are able to model reasonably well only a limited class of materials, namely rare gas solids and simple metals. In other materials, like covalent solids and noble metals, many-body effects are extremely important, and should be accounted for by any realistic empirical force scheme. This is particularly true in presence of surfaces or defects, where electron redistribution effects produce forces on the ions which cannot be mimicked by pair potentials.

In this thesis, I will describe an empirical many-body force scheme,

named the "glue" model, which we have developed in an attempt to make feasible large-scale simulations of metallic systems. In this scheme, the two-body term in V is supplemented by a many-body term (the "glue"), which acts to keep the coordination of the atoms as close as possible to its bulk value. This gives rise to additional forces, which are particularly strong where the coordination is poor (surfaces, clusters, etc.).

In spite of the many-body character, the forces are calculated only from the knowledge of the distances between pair of atoms. The computational effort is thus comparable with that required by two-body potentials, meaning that simulations including several thousands of atoms can be easily performed.

This model is well suited to noble metals, where the very important cohesive contribution from the (nearly) filled d-band seems expressible in terms of atomic coordination. We have focused in particular on gold, which is unique among all noble metals in exhibiting reconstructions (i.e., the atomic arrangement on the surface is not a simple projection of the bulk crystal structure) on *all* its low-index surfaces, notably Au(100), Au(110) and Au(111). It turns out that the simple "glue" mechanism is able to explain the occurrence of these reconstructions simply as the result of a tendency to increase surface packing. Gold also has other peculiar properties, as listed in Chapter 1, none of which has been described microscopically before.

This thesis is organized as follows. Chapter 1 introduces the model, and presents several analytical relations which connect the Hamiltonian with physical properties of the real material. In Chapter 2, the procedure used to fit the model to gold, involving computer simulations at finite temperature, is described in detail. Some details on the implementation of glue forces in a molecular dynamics program are given in the Appendix. The results of molecular dynamics studies of bulk properties (thermal expansion, melting, liquid structure and thermodynamics, vacancies) are reported in Chapter 3. A detailed investigation of the structural properties of the gold surfaces at $T = 0$ (surface reconstructions) is given in Chapter 4. Chapter 5 describes an extensive molecular

dynamics study of the Au(111) surface at high temperature, aimed at detecting the possible existence of surface melting. Finally, a study of the structural properties of gold clusters, containing a number of atoms in the range 100–1000, is detailed in Chapter 6. Chapter 7 concludes the thesis with a summary of the main results.

Parts of the results presented in this thesis have been, or are being published in the papers in Ref. [3].

Chapter 1

The glue model

1.1 Failures of pair potentials in metallic materials

In almost all the empirical schemes used in the past for computer simulations of condensed matter systems, the total potential energy V is written as a sum of pairwise interactions between the particles:

$$V = \frac{1}{2} \sum_{\substack{i,j=1 \\ (j \neq i)}}^{N} \phi(r_{ij}) \tag{1.1}$$

where r_{ij} is the distance between nuclei i and j, and the factor $\frac{1}{2}$ avoids double counting. All the physical information on the system under study is completely embodied in $\phi(r)$. This is of course an enormous simplification in the description of a material, which allows to perform simulations very easily. However, we should consider now in which cases this approximation can be justified.

In rare gas solids, cohesion is due to the van der Waals attractive forces which do not exactly have a two-body nature, but can be treated as such to a good approximation. It is in fact well known that this kind of materials can in practice be described quite accurately using pair potentials, such as the Lennard-Jones potential [4].

On the other hand, the properties of a metal are dominated by the conduction electrons. How these electrons respond to ionic motions

determines the form of the atomic interactions. Our problem is whether it is possible to describe these interactions in terms of two-body forces between ions or not.

Metals can be divided in two general classes: simple and non-simple. Simple metals, like sodium, can be thought of as non-overlapping ions immersed in a sea of nearly-free conduction electrons. Each ion consists of a nucleus surrounded by closed shells of tightly bound core electrons. In pseudopotential theory [5] the ions, treated as point charges, are screened by the conduction electrons which tend to follow the ions adiabatically. The result is that for several purposes the metal can be described by effective pairwise forces between the ions [6].

Non-simple metals, like transition metals, are more subtle. The free atoms contain partially filled shells of d-electrons, and s and p valence electrons. When the atoms are brought together to form the metal, a rather complex band structure appears, with d-bands and sp-bands above and below the Fermi level. How crystal cohesion can be microscopically understood in these cases has been described in the literature [7,8]. If we displace an ion, the rearrangement of the electrons cannot be described as a cloud of charge following the ion. Therefore, it is clear that the pairwise approximation will generally not work in the case of transition metals [6], although it may still serve for some particular study, e.g., bulk phonons. In any case, extracting an effective pair potential from first principles is difficult, and the usual choice consists in building it empirically by fitting known bulk properties of the material, such as the lattice constant, the cohesive energy, the phonon frequencies and so on.

There are however some serious intrinsic drawbacks in the pair potential approach which prevent an accurate description of several classes of materials. In the case of noble metals, and focusing particularly on gold which is the subject of the present work, the most important failures of two-body interactions can be summarized as follows:

1. Let us define the dimensionless ratio $C = \epsilon_c/k_B T_m$, where ϵ_c is the cohesive energy, T_m the melting temperature and k_B the Boltz-

Material	ϵ_c	T_m	C	S_m	$\Delta V/V_s$
Ne	0.02	24	9.7	1.64	15.3
Ar	0.080	84	11.1	1.69	14.4
Kr	0.116	117	11.5	1.69	15.1
Xe	0.17	161	12.3	1.71	15.1
Al	3.34	933	41.5	1.39	6.5
Pb	2.04	601	39.4	0.96	3.6
Ni	4.435	1728	29.8	1.22	5.4
Pd	3.936	1825	25.0	1.13	5.9
Pt	5.852	2042	33.3	1.16	6.6
Cu	3.50	1357	29.9	1.16	4.2
Ag	2.96	1234	27.8	1.10	3.8
Au	3.78	1336	32.8	1.13	5.2

Table 1.1:

Cohesive energies (in eV/atom), melting temperatures (in degrees Kelvin), ratios $C = \epsilon_c/k_B T_m$, entropy changes on melting S_m (in k_B/atom) and volume changes on melting $\Delta V/V_s$ (in %) for several f.c.c. solids. Cohesive energies are from Ref. [9], all other data from Ref. [10].

mann constant. We can see from Table 1.1 that C is about 10 in rare gas solids, but around 30 in metals.

Using two-body forces, the cohesive energy is simply due to the bonds that must be broken to remove an atom, and can be easily calculated for a given crystal structure. For example, for a first-neighbour potential we have

$$\epsilon_c = -\frac{\mathcal{N}}{2}\phi(d)$$

where d is the first neighbour distance and $\mathcal{N}$ the coordination number (12 for the f.c.c. structure). The melting temperature can be extracted from computer simulations (with the molecular dynamics technique). It turns out that in two-body systems C

is usually of the order of 10. This implies that in metals ϵ_c and T_m cannot be reproduced simultaneously using pair potentials. A system with the correct cohesion is stiff compared to the real material and melts at a much higher temperature, while a system with a nearly correct T_m has a cohesion too low [11].

2. Table 1.1 shows also that metals have a low entropy change and volume change on melting when compared with rare gas solids. Again, these characteristics are not well reproduced by pairwise forces. For example, a system described by the Lennard-Jones potential has, at the triple point, $C = 12.8$, $S_m = 2.16\, k_B$/atom, $\Delta V/V_s = 17.7\%$ [12].

3. Another difficulty with two-body potentials is that the vacancy formation energy ϵ_v^F is nearly equal to the cohesive energy ϵ_c. In fact, the energy required to create a vacancy is given by

$$\epsilon_v^F = E_N^v - E_N$$

where E_N is the total energy of a system with N particles in N crystal sites (no vacancy), and E_N^v is the total energy of a system with N particles in $N+1$ crystal sites, i.e. with a vacancy. In the pairwise scheme, if we neglect the effect of atom relaxations around the vacancy (which is usually rather small, see e.g. Ref. [13] for the Lennard-Jones system), we have

$$E_N^v - E_{N+1} = -\mathcal{N}\phi(d)$$

$$E_{N+1} - E_N = -\epsilon_c = \frac{\mathcal{N}}{2}\phi(d)$$

and therefore

$$\epsilon_v^F = -\frac{\mathcal{N}}{2}\phi(d) = \epsilon_c$$

On the other hand, Table 1.2 shows that in metals ϵ_v^F/ϵ_c is in the range 0.25–0.35. The fact that it is relatively easy to create defects in the material is of course connected with the low melting temperature [18].

Material	ϵ_c	ϵ_v^F	ϵ_v^F/ϵ_c	Ref.
Ne	0.02	0.021	1.05	[14]
Ar	0.080	0.076	0.95	[14]
Kr	0.116	0.077	0.66	[14]
Al	3.34	0.76	0.23	[15]
Pb	2.04	0.49	0.24	[16]
Ni	4.435	1.39	0.31	[17]
Pt	5.852	1.51	0.26	[15]
Cu	3.50	1.14	0.33	[15]
Ag	2.96	1.08	0.36	[15]
Au	3.78	0.95	0.25	[15]

Table 1.2:

Vacancy formation energies (in eV) and their ratios to the cohesive energies for several f.c.c. solids.

4. Another discrepancy between two-body and metallic systems is related to the so-called "Cauchy relation" between two of the three independent elastic constants in a cubic crystal:

$$C_{12} = C_{44} \tag{1.2}$$

Its validity is a mathematical consequence of using pairwise central forces [19,20], but, as Table 1.3 shows, it is far from being satisfied in metals. In noble metals the ratio C_{12}/C_{44} is around 2, reaching a spectacularly high 3.7 in Au. The low value of C_{44}, which is one of the shear moduli, is related to the high ductility and malleability of gold.

5. Surface properties are also a quite severe test for the validity of interatomic forces. For example, it can be shown [22,23] that a two-body potential without oscillations, such as the classical Lennard-Jones or Morse potentials, always leads to an outward relaxation of the first surface layer (i.e., the distance between the first and

Material	C_{11}	C_{12}	C_{44}	C_{12}/C_{44}	Ref.
Ne	0.0166	0.0086	0.0095	0.9	[21]
Ar	0.042	0.024	0.022	1.1	[21]
Kr	0.051	0.028	0.027	1.0	[21]
Xe	0.053	0.028	0.030	0.9	[21]
Al	1.143	0.619	0.316	2.0	[9]
Pb	0.555	0.454	0.194	2.3	[9]
Ni	2.612	1.508	1.317	1.2	[9]
Pd	2.341	1.761	0.712	2.5	[9]
Cu	1.762	1.249	0.818	1.5	[9]
Ag	1.315	0.973	0.511	1.9	[9]
Au	2.016	1.697	0.454	3.7	[9]

Table 1.3:

Elastic constants at $T = 0$ (in $10^{12}\,\mathrm{dyne/cm^2}$), and ratios C_{12}/C_{44}, for several f.c.c. solids. A ratio C_{12}/C_{44} greater than 1 indicates presence of many-body effects.

the second layer exceeds the bulk interplanar distance) [1]. On the other hand, metals usually exhibit an inward relaxation of the first layer [25]. As shown by Finnis and Heine [26], this contraction can be understood in terms of electrostatic forces. Moreover, surface reconstructions (which occur on many-metal surfaces) cannot be explained by two-body schemes (unless, of course, a *different* potential is used for surface atoms [27]).

Another, perhaps more serious problem which occurs at surfaces of two-body systems is an unrealistically high evaporation rate near the melting point, as seen from molecular dynamics simulations [28,29], clearly caused by the low $\epsilon_c/k_B T_m$ ratio. This results in a very high value for the vapour tension. Again, this is a situation typical, for example, of rare gas solids but not of metal surfaces, where the evaporation rate is so low that no atoms leaving the surface should be seen at reasonable temperatures on the size and time scales used in computer simulations (of course, this is another aspect of the impossibility of obtaining at the same time a good cohesive energy and a good melting temperature). In summary, the surface properties predicted by two-body potentials are generally vastly different from those of the real metal.

Some of the difficulties described above can be avoided by adding a volume-dependent term to the total potential energy [30]. In its simple form, this correction contains a term linear in the volume:

$$V = \frac{1}{2} \sum_{\substack{i,j=1 \\ (j \neq i)}}^{N} \phi(r_{ij}) + p_0 \Omega \tag{1.3}$$

where p_0 is a constant and Ω the total volume of the system. In particular, it can be shown that by choosing

$$p_0 = \frac{1}{2}(C_{12} - C_{44}) \tag{1.4}$$

[1] Inward relaxations can be predicted, however, by potentials with an oscillatory tail [23,24]

we obtain correct values for the elastic constants, i.e. the Cauchy relation no longer holds. For this reason, the quantity $(C_{12} - C_{44})/2$ is called the "Cauchy pressure". While this approach may be helpful for a better representation of the bulk, it raises new problems when applied on surfaces (external or internal, as in vacancies, cracks, ...), where the volume is not unambiguously defined [31,32]. Here, an adequate modelling can be achieved only by introducing *local* many-body contributions.

Therefore, one is led to the conclusion that a scheme based on pair interactions does not describe a metal in an adequate way, in particular when surface properties are considered. An empirical many-body force scheme able to overcome all the difficulties mentioned above, named the "glue" model, will be introduced in Sec. 1.3.

1.2 The role of coordination

Electronic cohesion in noble and near-noble metals is largely due to the d-electrons, which form very broad, filled d-bands. How does an ion immersed in this electron sea move ? In particular, how can we express the forces acting on the ion in terms of the positions of the other ions ? In attempting to model this situation, the key variable to consider is the local atomic coordination. A filled d-band has no possibility to rehybridize to form directional "bonds". Yet its energy is lowered, roughly proportionally to the d-bandwidth, once an atom is surrounded by many other identical atoms. The same reasoning, based just on coordination, would not work for an sp-bonded material, or for a partly filled d-band metal, where the role of directional chemical bonding should become crucial.

Therefore, assuming that the number of neighbours of a given noble metal ion represents in some way the amount of local electronic density, we can take the coordination as characterizing the environment in which our ion is situated. Schematically, then, when the coordination of an ion remains nearly constant during the motion, the ion interacts with

the others essentially through an effective two-body potential (for a discussion on this point, see Ref. [6]). On the other hand, motions which tend to change the coordination appreciably are greatly discouraged by their high energetic cost. Such motions easily occur in proximity of surfaces or defects, and the extreme case consists of pulling an atom out of the system.

This mechanism cannot be modelled by two-body forces, for one simple reason: a two-body scheme implies a *linear* dependence of the energy of an atom upon its coordination. The strength of any alternative scheme should be based on the *non-linearity* of this dependence. Let us consider, for example, the formation of a vacancy. In an f.c.c. crystal structure, it implies the change in coordination of the 12 neighbouring atoms from 12 to 11. In our picture, this change is rather small and leaves almost unchanged the local environment, so the vacancy formation energy will be low. On the other hand, extracting a single atom from the system implies changing its coordination from 12 to 0. This is a dramatic change, and the associated energy cost (which is the cohesive energy) will be high. It is evident here that the difference between ϵ_v^F and ϵ_c is an expression of the non-linearity of the energy of an atom as a function of its coordination.

1.3 The glue Hamiltonian

These concepts can be expressed in mathematical form by writing the total potential energy of a system of N atoms as

$$V = \frac{1}{2} \sum_{\substack{i,j=1 \\ (j \neq i)}}^{N} \phi(r_{ij}) + \sum_{i=1}^{N} U(n_i) \tag{1.5}$$

A standard two-body part is still present, together with the new many-body term which replaces the volume-dependent term in Eq. (1.3). Here, n_i is the coordination of atom i, and the function $U(n)$ associates an energy value to this coordination, thereby including the previously discussed "gluing" effects of the conduction electrons. For this reason, $U(n)$

has been nicknamed the "glue", and Eq. (1.5) the "glue Hamiltonian" [33,34,35].

It is natural to impose

$$U(0) = 0 \tag{1.6}$$

In this way, the total energy is referred to that of a system of N atoms at rest, infinitely far each from the other. Of course, we expect $U(n)$ to be negative in the coordination range of our interest.

In order to use Eq. (1.5) in computer simulations, we need a procedure to compute n_i for each atom in the system. The simplest choice consists in building n_i as a superposition of contributions from the neighbouring atoms:

$$n_i = \sum_{\substack{j=1 \\ (j \neq i)}}^{N} \rho(r_{ij}) \tag{1.7}$$

where $\rho(r)$ is a short-ranged, monotonically decreasing function of distance. Equation (1.7) essentially counts the number of neighbours of atom i. This is done in a continuous way, so that nearby atoms give a larger contribution to n_i than more remote atoms. The final result for n_i is a real number that generalizes the usual idea of coordination.

The units for ρ (and n) are arbitrary, because they are only auxiliary quantities in this scheme. In particular, given $\rho(r)$ and $U(n)$, the new pair

$$\begin{aligned} \tilde{\rho}(r) &= c\rho(r) \\ \tilde{U}(n) &= U(n/c) \end{aligned} \tag{1.8}$$

describes the same physics, i.e., it gives rise to the same forces for an arbitrary value of c. So we have the freedom to define a scale for n. A convenient choice is to make it coincident with the ordinary coordination number for a bulk atom. Assuming an f.c.c. (or h.c.p.) crystal structure, this means that we are free to fix arbitrarily, but suggestively,

$$n_0 = 12 \tag{1.9}$$

where n_0 indicates the result of applying eq. (1.7) to a bulk atom in an undistorted lattice. When $\rho(r)$ has a range limited to the first neighbours, it is $n_0 = 12\rho(d)$ where d is the first-neighbour distance, and

therefore condition (1.9) becomes simply

$$\rho(d) = 1 \tag{1.10}$$

This normalization will be adopted from now on.

The glue Hamiltonian is particularly convenient from the computational point of view, since the atomic positions appear only in the form of distances between pairs. In spite of the intrinsic many-body character of the glue, there are no explicit three-body or more complex terms in the expressions for the forces [2]. In fact, the force $\vec{F}_i$ acting on a particle i is given by the following formula, obtained by derivation of eq. (1.5) (and using (1.7)):

$$\vec{F}_i = -\sum_{j\neq i}\Big(\phi'(r_{ij}) + [U'(n_i) + U'(n_j)]\rho'(r_{ij})\Big)\frac{\vec{r}_{ij}}{r_{ij}} \tag{1.11}$$

where $\vec{r}_{ij} = \vec{r}_i - \vec{r}_j$ and the prime indicates derivation. The extension of a standard molecular dynamics (MD) program to include the glue forces is relatively easy to accomplish, and is discussed in the Appendix.

Finally, let us note that the form of Hamiltonian (1.5) allow us to assign an energy ϵ_i to each atom i in the system:

$$\epsilon_i = \frac{1}{2}\sum_{\substack{j=1\\(j\neq i)}}^{N} \phi(|\vec{r}_i - \vec{r}_j|) + U(n_i) \tag{1.12}$$

so that $V = \sum_{i=1}^{N} \epsilon_i$. This equation is often used to study how the energy is distributed between different parts of the system.

1.4 Other many-body force schemes

We have introduced the glue Hamiltonian from a purely empirical point of view. At least two other families of similar approaches can be found in literature: one, similar in spirit to the glue scheme, is in connection with the tight-binding model, the other, called "embedded-atom-method"

[2] Three-body terms *do* appear, however, in the force constants, as will be shown in Sec. 1.6.

(EAM), leads to the same form for the Hamiltonian by starting from first principles considerations.

The former approach has been proposed by Finnis and Sinclair [36] for use in b.c.c. transition metals. In their Hamiltonian, the glue function is fixed to be $U(n) = -A\sqrt{n}$, while $\phi(r)$ and $\rho(r)$ are built empirically. This particular form for $U(n)$ comes from the second moment approximation to the tight-binding model [7,37].

In the "embedded-atom-method", introduced by Daw and Baskes [38,39], each atom of the metal is seen as an "impurity" embedded in a host system consisting of all other atoms. In the density-functional theory framework, using the uniform density approximation [40,41], the energy of this impurity can be written as a function of the host electron density (i.e., before the introduction of the impurity) $n_h(\vec{r})$ at the impurity site $\vec{R}$:

$$E_{imp} = F(n_h(\vec{R}))$$

Starting from this observation, Daw and Baskes take the following *ansatz* for the total energy of the system:

$$E_{tot} = \sum_i F(n_i)$$

where n_i is the electron density at the site of atom i of a system in which atom i is missing.

Two further assumptions are required:

- A two-body part is also needed to account for the core-core repulsion. The potential is assumed to be purely repulsive.
- n_i can be approximatively constructed as a superposition of atomic densities:

  $$n_i = \sum_j \rho(r_{ij})$$

  Here, $\rho(r)$ is the electron density distribution of a free atom, taken from Hartree-Fock calculations.

The resulting Hamiltonian is thus formally identical to the glue Hamiltonian. Here, n is directly interpreted as the electronic density

(while in the glue scheme it is simply an auxiliary variable, not identified with a precise physical quantity), and the function $\rho(r)$ is fixed to be the electronic density of an isolated atom, taken from Hartree-Fock calculations [42].

In a recent reformulation of this type of scheme, named the "effective medium" theory [43], the "embedding energy" $F(n)$, and the electronic density around an atom $\rho(r)$, are self-consistently calculated for an atom in a homogeneous electron gas within the local density approximation.

For d-band metals, however, owing to the large number of approximations involved, connections with first principles cannot be of too much practical help in finding the optimal functions, so that usually it remains necessary to resort to an empirical fit procedure. For this reason, we find it desirable to leave *all* the three functions ϕ, U and ρ undetermined at the onset, but instead available for the fit. We have used this additional freedom to characterize well the thermal behaviour and the surface properties of the system, as discussed later.

1.5 An invariance property in the glue Hamiltonian

In some of the "first principles" derivations described above, the glue part supplies the electronic cohesion while the two-body potential simulates the core-core repulsion between the ions. While this physical distinction seems appealing, no such distinction really exists when considering the glue Hamiltonian in practice, because of the existence of a peculiar invariance property: a glue Hamiltonian defined by $\phi(r)$, $U(n)$, $\rho(r)$ remains unchanged when these functions are replaced by $\hat{\phi}(r)$, $\hat{U}(n)$, $\rho(r)$, where

$$\begin{aligned} \hat{\phi}(r) &= \phi(r) + 2\lambda\rho(r) \\ \hat{U}(n) &= U(n) - \lambda n \end{aligned} \tag{1.13}$$

and λ is an arbitrary real number. In fact, in going from ϕ, U, ρ to $\hat{\phi}$, $\hat{U}$, ρ, we add and subtract the same quantity in the two terms in eq. (1.5).

This has some practical consequences. First of all, a glue term which is a linear function of coordination is equivalent to a two-body term (in fact, it can be eliminated by choosing λ appropriately); the physical meaning of this statement has been already discussed. Less trivially, there is no unique choice for ϕ and U, since a term linear in the coordination can be transferred from the two-body part to the glue part and vice versa without any change in the physics. For instance, one may have a system where the two-body potential is purely repulsive and all the attraction is supplied by the glue; at the equilibrium lattice spacing, these two forces balance exactly. But with the appropriate transformation it is also possible to construct a completely equivalent Hamiltonian where both the two-body part alone and the glue part alone predict the same, equilibrium lattice spacing.

Therefore, in spite of the physical reasoning which led us to conceive the glue $U(n)$ and the glue Hamiltonian, we are not able to attach a physical meaning to either $U(n)$ or $\rho(r)$ when considered separately. Of course, only quantities that are invariant with respect to (1.13) can be connected to physical properties. Some examples of invariant quantities are $\rho(r)$ itself, the second derivative of the glue $U''(n)$, the "effective potential" [35,36,38]

$$\psi(r,n) = \phi(r) + 2U'(n)\rho(r) \tag{1.14}$$

Another obvious consequence of this invariance property is that a condition can be arbitrarily imposed, thereby removing the ambiguity. A particularly convenient choice, in that it makes the fitting process easier, is

$$U'(n_0) = 0 \tag{1.15}$$

where n_0 is the bulk coordination (Eq. (1.9)). In particular, as it will be shown in the next Section, with this choice the transverse phonon frequencies depend only on the two-body potential. From now on, condition (1.15) will be assumed to hold.

1.6 Lattice dynamics in the glue model

1.6.1 Force constants

In this Subsection and in the following, some basic lattice dynamics relations will be quickly recalled for clarity of exposition. The reader may consult Ref. [1] for a full general treatment.

Let us consider a system of N particles in an equilibrium configuration, so that the force acting on each particle is zero. The total potential energy V can be expanded in powers of the atomic displacements $\vec{u}_m$ from equilibrium. The first order terms vanish around the equilibrium position, so that we obtain

$$V = V_0 + \frac{1}{2} \sum_{m\alpha n\beta} C_{mn}^{\alpha\beta} u_m^\alpha u_n^\beta + \dots \tag{1.16}$$

where V_0 is the equilibrium energy of the system, indexes m and n run on the particles, and α and β on the three cartesian directions. In the harmonic approximation we neglect all third or higher order terms, so that the vibrational properties of the system are completely characterized by the force constants

$$C_{mn}^{\alpha\beta} = \left. \frac{\partial^2 V}{\partial u_m^\alpha \partial u_n^\beta} \right|_0 \tag{1.17}$$

The requirement that the total potential energy should not change when we displace rigidly the whole system leads to the condition

$$\sum_{n\beta} C_{mn}^{\alpha\beta} = 0 \tag{1.18}$$

Let us suppose now that the particles are interacting through the glue potential (1.5). An explicit expression for the force constants can be obtained straightforwardly by applying Eq. (1.17) to (1.5). The result has the form

$$C_{mn}^{\alpha\beta} = \delta_{mn} \sum_i D_{mi}^{\alpha\beta} - D_{mn}^{\alpha\beta} \tag{1.19}$$

with $D_{mn}^{\alpha\beta}$ given by

$$D_{mn}^{\alpha\beta} = \Phi_{mn}^{\alpha\beta} + \Psi_{mn}^{\alpha\beta} + \Gamma_{mn}^{\alpha\beta} \tag{1.20}$$

where

$$\Phi_{mn}^{\alpha\beta} = \left(\phi''(r_{mn}) - \frac{\phi'(r_{mn})}{r_{mn}}\right)\frac{r_{mn}^{\alpha} r_{mn}^{\beta}}{r_{mn}^2} + \delta_{\alpha\beta}\frac{\phi'(r_{mn})}{r_{mn}} \tag{1.21}$$

$$\Psi_{mn}^{\alpha\beta} = [U'(n_m) + U'(n_n)]\left\{\left(\rho''(r_{mn}) - \frac{\rho'(r_{mn})}{r_{mn}}\right)\frac{r_{mn}^{\alpha} r_{mn}^{\beta}}{r_{mn}^2} + \delta_{\alpha\beta}\frac{\rho'(r_{mn})}{r_{mn}}\right\} \tag{1.22}$$

$$\Gamma_{mn}^{\alpha\beta} = \sum_l (t_{mln}^{\alpha\beta} + t_{lnm}^{\alpha\beta} - t_{mnl}^{\alpha\beta}) \tag{1.23}$$

where the coefficients $t_{mnl}^{\alpha\beta}$ are defined as

$$t_{mnl}^{\alpha\beta} \equiv U''(n_l)\rho'(r_{ml})\rho'(r_{nl})\frac{r_{ml}^{\alpha} r_{nl}^{\beta}}{r_{ml} r_{nl}} \tag{1.24}$$

if $m \neq l$ and $n \neq l$, and

$$t_{mnm}^{\alpha\beta} = t_{mnn}^{\alpha\beta} = 0 \tag{1.25}$$

Let us note the following points:

- The form (1.19) of the force constants guarantees that the translational invariance condition (1.18) is satisfied.
- The quantities $D_{mm}^{\alpha\beta}$ (and therefore $\Phi_{mm}^{\alpha\beta}$, $\Psi_{mm}^{\alpha\beta}$, $\Gamma_{mm}^{\alpha\beta}$) have no physical effect, since they cancel away in the expression (1.19) for the force constants $C_{mm}^{\alpha\beta}$. Only the terms $D_{mn}^{\alpha\beta}$ with $m \neq n$ are important.
- In a system with pairwise interactions only, $\Psi_{mn}^{\alpha\beta} = \Gamma_{mn}^{\alpha\beta} = 0$. $\Phi_{mn}^{\alpha\beta}$ is therefore the two-body part of $D_{mn}^{\alpha\beta}$.
- The form of $\Psi_{mn}^{\alpha\beta}$ resembles that of $\Phi_{mn}^{\alpha\beta}$. To understand this term, note that if $U(n) = \lambda n$, then $\Gamma_{mn}^{\alpha\beta} = 0$ and $\Psi_{mn}^{\alpha\beta}$ is the entire glue contribution. But we have already noted in Sec. 1.5 that in this case the glue term is completely equivalent to a two-body potential. Therefore, $\Psi_{mn}^{\alpha\beta}$ should be regarded as another two-body part, coming from the glue term. The part which is really many-body is $\Gamma_{mn}^{\alpha\beta}$, and $\Phi_{mn}^{\alpha\beta} + \Psi_{mn}^{\alpha\beta}$ is the "effective two-body part".

- $\Gamma^{\alpha\beta}_{mn}$ is a sum of "triplet" terms. In the glue model two-particle terms are sufficient to construct the forces (first order derivatives), but three-particle terms are required for the force constants (second order derivatives), and in general $(n+1)$-particle terms are required for n-th order derivatives. This makes the glue model somewhat less attractive for lattice dynamics calculations, compared with Monte Carlo and molecular dynamics.

Up to now, we did not make any particular assumption on the symmetry of the system, so that the formulas we have written can be applied to infinite crystals as well as to less symmetric situations such as systems with defects, surfaces, clusters or amorphous structures. If we now assume that the atoms are arranged in an infinite crystal with one atom per unit cell, some simplifications can be made. First, all atoms must have the same coordination:

$$n_m = \sum_{n \neq m} \rho(r_{mn}) = n_0 \tag{1.26}$$

Let us assume that (1.15) is satisfied:

$$U'(n_0) = 0$$

(if it is not so, a transformation of the form (1.13) can be applied), and let us call

$$U''(n_0) \equiv U''_0 \tag{1.27}$$

With condition (1.15), $\Psi^{\alpha\beta}_{mn}$ vanishes. Moreover, since for symmetry reasons

$$\sum_{l \neq n} \frac{\rho'(r_{ln})}{r_{ln}} r^{\beta}_{ln} = 0 \tag{1.28}$$

for all n and β, it is easy to show that $\Gamma^{\alpha\beta}_{mn}$ becomes simply

$$\Gamma^{\alpha\beta}_{mn} = -U''_0 \sum_{l} \frac{\rho'(r_{ml})}{r_{ml}} \frac{\rho'(r_{nl})}{r_{nl}} r^{\alpha}_{ml} r^{\beta}_{nl} \tag{1.29}$$

1.6.2 Bulk phonons in a perfect crystal

In the harmonic limit, as follows by Eq. (1.16), the equations of motion of the atoms in the lattice are

$$M\ddot{u}_m^\alpha = -\sum_{n\beta} C_{mn}^{\alpha\beta} u_n^\beta \tag{1.30}$$

where M is the mass of an atom. If we choose a solution of the form

$$u_m^\alpha(t) = \frac{1}{\sqrt{M}} e^\alpha \exp(-i\omega t + i\vec{k}\cdot\vec{r}_{m0}) \tag{1.31}$$

and substitute it into (1.30), we find that

$$M\omega^2 e^\alpha = \sum_\beta D^{\alpha\beta}(\vec{k}) e^\beta \tag{1.32}$$

where $D^{\alpha\beta}(\vec{k})$ is the *dynamical matrix* and is connected to the force constants $C_{mn}^{\alpha\beta}$ by

$$D^{\alpha\beta}(\vec{k}) = \sum_n C_{mn}^{\alpha\beta} \exp(i\vec{k}\cdot\vec{r}_{nm}) \tag{1.33}$$

or to the related quantities $D_{mn}^{\alpha\beta}$ (using (1.19)) by

$$D^{\alpha\beta}(\vec{k}) = \sum_{n\neq m} D_{mn}^{\alpha\beta} \left(1 - \exp(i\vec{k}\cdot\vec{r}_{nm})\right) \tag{1.34}$$

$D^{\alpha\beta}(\vec{k})$ does not depend on m as a consequence of the periodicity of the lattice. As Eq. (1.32) shows, the bulk phonon dispersion $\omega(\vec{k})$ is then straightforwardly obtained by diagonalization of the 3×3 dynamical matrix.

Assuming now a glue-type interaction, the dynamical matrix can be separated in two parts:

$$D^{\alpha\beta}(\vec{k}) = \Phi^{\alpha\beta}(\vec{k}) + \Gamma^{\alpha\beta}(\vec{k}) \tag{1.35}$$

where

$$\Phi^{\alpha\beta}(\vec{k}) = \sum_{n\neq m} \Phi_{mn}^{\alpha\beta} \left(1 - \exp(i\vec{k}\cdot\vec{r}_{nm})\right) \tag{1.36}$$

and

$$\Gamma^{\alpha\beta}(\vec{k}) = \sum_{n \neq m} \Gamma^{\alpha\beta}_{mn} \left(1 - \exp(i\vec{k} \cdot \vec{r}_{nm})\right) \tag{1.37}$$

with $\Phi^{\alpha\beta}_{mn}$ and $\Gamma^{\alpha\beta}_{mn}$ supplied respectively by (1.21) and (1.29). With a little manipulation, the result can be written as

$$\Phi^{\alpha\beta}(\vec{k}) = 2 \sum_{\vec{R} \neq 0} \sin^2\left(\frac{\vec{k} \cdot \vec{R}}{2}\right) \left[\left(\phi''(R) - \frac{\phi'(R)}{R}\right) \frac{R^\alpha R^\beta}{R^2} + \delta_{\alpha\beta} \frac{\phi'(R)}{R}\right] \tag{1.38}$$

$$\Gamma^{\alpha\beta}(\vec{k}) = U_0'' \left[\sum_{\vec{R} \neq 0} \sin(\vec{k} \cdot \vec{R}) \frac{\rho'(R)}{R} R^\alpha\right] \left[\sum_{\vec{R} \neq 0} \sin(\vec{k} \cdot \vec{R}) \frac{\rho'(R)}{R} R^\beta\right] \tag{1.39}$$

where the sums run on the lattice vectors.

1.7 Connection with physical properties

In this Section, we derive some relations connecting the glue Hamiltonian with a certain number of physical quantities. These relations will be useful in building ϕ, U, ρ by fitting these quantities to the experimental values for a given material. We assume:

- an f.c.c. crystal structure
- a first-neighbour range for $\phi(r)$ and $\rho(r)$
- the normalizations (1.9) and (1.10) for n and ρ: $n_0 = 12$, $\rho(d) = 1$
- condition [3] (1.15): $U'(n_0) = 0$

These restrictions allow us to write simple formulas, which will be used in Chapter 2 to fit the Hamiltonian to the experimental data for gold. To simplify the notations, we shall often omit the arguments of the functions ϕ, ρ, U or of their derivatives, being implicit that ϕ and ρ are to be evaluated in $r = d$, and U in $n = n_0$. More general formulas can be found in Refs. [35] and [38].

[3] If this condition does not hold, all the following results are still valid if the two-body potential $\phi(r)$ is replaced by the "effective potential" (1.14) calculated for $n = n_0$.

1.7.1 Cohesive energy, bulk modulus, vacancy and surface energy

Let us consider the potential energy per atom in a perfect lattice where R is the first-neighbour distance:

$$\epsilon(R) = \frac{12}{2}\phi(R) + U(12\rho(R)) \tag{1.40}$$

In the general case the system is not in equilibrium, so that there is a net pressure

$$p(R) = -\frac{d\epsilon}{d\Omega_0} = -\frac{\sqrt{2}}{3R^2}\frac{d\epsilon}{dR} = -\frac{2\sqrt{2}}{R^2}\Big(\phi'(R)+2\rho'(R)U'(12\rho(R))\Big) \tag{1.41}$$

where $\Omega_0 = R^3/\sqrt{2}$ is the volume occupied by an atom. Of course, when R is equal to the equilibrium distance d this pressure vanishes:

$$p(d) = -\frac{2\sqrt{2}}{d^2}\Big(\phi'(d) + 2\rho'(d)U'(n_0)\Big) = 0 \tag{1.42}$$

(by definition, $n_0 = 12\rho(d)$). Since $U'(n_0) = 0$, this condition reduces to the ordinary equilibrium condition for two-body potentials

$$\phi'(d) = 0 \tag{1.43}$$

$\epsilon(R)$ has a minimum for $R = d$, which is, apart of the sign, the cohesive energy:

$$\epsilon_c = -\epsilon(d) = -\Big[6\phi(d) + U(n_0)\Big] \tag{1.44}$$

The bulk modulus of the system

$$B = -\Omega_0\frac{dp}{d\Omega_0} = \Omega_0\frac{d^2\epsilon}{d\Omega_0^2} = \frac{\sqrt{2}}{9d}\left.\frac{d^2\epsilon}{dR^2}\right|_{R=d} \tag{1.45}$$

is given by

$$B = \frac{1}{d\sqrt{2}}\Big[\frac{4}{3}\phi''(d) + 32[\rho'(d)]^2U''(n_0)\Big] \tag{1.46}$$

Equations (1.43), (1.44) and (1.46) give us three relations that can be used in the fit.

The glue Hamiltonian solves the problem of the low vacancy formation energy compared to the cohesive energy. In fact the former,

neglecting relaxations, is the energy associated with the breaking of 12 bonds, and the change of coordination of the 12 neighbour atoms from 12 to 11:

$$\epsilon_v^F = -6\phi(d) + 12[U(11) - U(12)] \tag{1.47}$$

while the latter is given by (1.44). The two quantities differ by virtue of the non-linearity of the glue.

Finally, the surface energy per atom on a (111) unrelaxed f.c.c. face is obtained by removing 3 bonds and changing the coordination from 12 to 9:

$$\epsilon_s = -\frac{3}{2}\phi(d) + U(9) - U(12) \tag{1.48}$$

Of course, ϵ_v^F and ϵ_s will be further lowered by relaxation effects, as will be discussed in detail later on.

1.7.2 Phonon frequencies

In an f.c.c. structure, the 12 first neighbours lattice vectors are

$$\{\vec{R}\} = \frac{a}{2}\begin{pmatrix}\pm 1\\ \pm 1\\ 0\end{pmatrix}, \frac{a}{2}\begin{pmatrix}0\\ \pm 1\\ \pm 1\end{pmatrix}, \frac{a}{2}\begin{pmatrix}\pm 1\\ 0\\ \pm 1\end{pmatrix} \tag{1.49}$$

Eq. (1.38) and (1.39) for the two-body and the many-body part of the dynamical matrix can therefore be explicitly written:

$$\Phi^{\alpha\beta}(\vec{k}) = 2\phi'' \sum_{\vec{R}\in\{\vec{R}\}} \sin^2\left(\frac{\vec{k}\cdot\vec{R}}{2}\right)\frac{R^\alpha R^\beta}{R^2} =$$

$$= \begin{cases} 4\phi'' - 2\phi''\cos\frac{k^\alpha a}{2}\left(\sum_\gamma \cos\frac{k^\gamma a}{2} - \cos\frac{k^\alpha a}{2}\right) & \text{if } \alpha = \beta \\ 2\phi''\sin\frac{k^\alpha a}{2}\sin\frac{k^\beta a}{2} & \text{if } \alpha \neq \beta \end{cases} \tag{1.50}$$

and

$$\Gamma^{\alpha\beta}(\vec{k}) = U''\rho'^2\left[\sum_{\vec{R}\in\{\vec{R}\}} \sin(\vec{k}\cdot\vec{R})\frac{R^\alpha}{R}\right]\left[\sum_{\vec{R}\in\{\vec{R}\}} \sin(\vec{k}\cdot\vec{R})\frac{R^\beta}{R}\right] =$$

$$= 8U''\rho'^2 f^\alpha(\vec{k}) f^\beta(\vec{k}) \tag{1.51}$$

$\Gamma = (0,0,0)$	$M\omega^2 = 0$
$X = \frac{2\pi}{a}(1,0,0)$	$M\omega_L^2 = 8\phi''$ $M\omega_T^2 = 4\phi''$
$W = \frac{2\pi}{a}(1,\frac{1}{2},0)$	$M\omega_\Pi^2 = 6\phi''$ $M\omega_\Lambda^2 = 4\phi''$
$K = \frac{3\pi}{2a}(1,1,0)$	$M\omega_L^2 = (4+\sqrt{2})\phi'' + 2(6-4\sqrt{2})U''\rho'^2$ $M\omega_{T_1}^2 = (4+2\sqrt{2})\phi''$ $M\omega_{T_2}^2 = (2+\sqrt{2})\phi''$
$L = \frac{\pi}{a}(1,1,1)$	$M\omega_L^2 = 8\phi''$ $M\omega_T^2 = 2\phi''$

Table 1.4:
Relations for the phonon frequencies at some points of the Brillouin zone, for a first-neighbour glue Hamiltonian and an f.c.c. crystal structure. ϕ'' and ρ' are evaluated at the first-neighbour distance $r = d$, U'' at the bulk coordination $n = n_0$.

where

$$f^\alpha(\vec{k}) = \sin\frac{k^\alpha a}{2}\left(\sum_\gamma \cos\frac{k^\gamma a}{2} - \cos\frac{k^\alpha a}{2}\right) \tag{1.52}$$

These equations can be used to evaluate phonon frequencies at particular $\vec{k}$ points. Some frequencies are reported in Table 1.4. Two important points must be noted [35]:

- the glue term does not have any effect on the transverse phonon frequencies: that are completely determined by the two-body potential.

- even in longitudinal modes, the glue term does not have any effect in many $\vec{k}$ points that lie on the Brillouin zone boundaries. Among them, points X, W, L, the whole Π and Λ branches. Therefore, all the phonon frequencies at these points depend only on the two-body potential.

This facts can be intuitively understood by noting that the atomic density (or the coordination in our scheme) remains roughly constant in a transverse or stationary mode, while it is strongly modulated in a longitudinal, propagating mode. The phonon spectrum is therefore largely controlled by the two-body term.

It follows that, with a first-neighbour cutoff, all the transverse phonon branches depend on a single parameter, namely $\phi''(d)$. Clearly, some kind of compromise must be adopted when fitting the Hamiltonian to the vibrational properties, as will be discussed in Chapter 2.

1.7.3 Elastic constants

The elastic constants can be easily obtained from the phonon dispersions in the acoustic ($\vec{k} \to 0$) limit. The results for an f.c.c. structure and first-neighbour ranged functions are the following:

$$C_{11} = \frac{1}{a}(2\phi'' + 32U''\rho'^2) \tag{1.53}$$

$$C_{12} = \frac{1}{a}(\phi'' + 32U''\rho'^2) \tag{1.54}$$

$$C_{44} = \frac{1}{a}\phi'' \tag{1.55}$$

$$\frac{1}{2}(C_{11} - C_{12}) = \frac{1}{a}\frac{\phi''}{2} \tag{1.56}$$

The expressions obtained for the shear moduli C_{44} and $(C_{11} - C_{12})/2$ are those typical of two-body systems [44,45]. In fact, shear deformations are associated to transverse waves, which are not affected by the glue term as discussed in the previous Subsection.

On the other hand, the "Cauchy pressure" (Eq. (1.4)) depend only on the many-body part:

$$\frac{1}{2}(C_{12} - C_{44}) = \frac{1}{a}16U''\rho'^2 \tag{1.57}$$

Therefore, the glue Hamiltonian removes the Cauchy discrepancy in the elastic constants which occurs in two-body systems. It may be noted here that a system based *exclusively* on many-body forces of the glue

type would have $C_{44} = 0$, $C_{11} = C_{12}$, and therefore it would be unstable under shear deformations: two-body forces remain essential for a faithful description of the physical system.

Finally, let us note that the expression (1.46) for the bulk modulus B, previously obtained by applying an external pressure to the system, is recovered if we calculate B by combining the elastic constants derived in this Subsection from the dispersion relations:

$$B = \frac{1}{3}(C_{11} + 2C_{12}) = \frac{1}{a}\left(\frac{4}{3}\phi'' + 32U''\rho'^2\right) \qquad (1.58)$$

1.8 The lack of angular forces

It follows from the results of the previous Section that from the point of view of fitting the lattice vibration spectrum a glue Hamiltonian is not substantially better than a two-body description.

Such limitations in modelling the vibrational spectrum might be intrinsic of the glue Hamiltonian. The glue term is by nature non-directional, i.e., the glue energy depends only on the number of neighbours around an atom and their distance from it, while the distribution of the relative bond angles is not relevant. On the other hand, we expect that in real materials different angular arrangements of the atoms should make a significant difference to the energy. This picture is supported by the fact that it is possible to obtain an excellent agreement between the calculated and the experimental phonon dispersion relations by using three-body force constants with an angular dependence [46,47].

Another consequence of the lack of angular forces in the glue scheme is that, if the interaction range is limited to the first or second neighbours, the f.c.c. and h.c.p. crystal structures are predicted to have the same energy. This is due to the fact that in these crystal structures the first two shells contain the same number of neighbours (respectively 12 and 6) at the same distances. On the other hand, there is a difference in the *angular* disposition of the second neighbours, and from a physical point of view this, rather than the different number of third neighbours, is likely to be the origin of the f.c.c.-h.c.p. energy difference [31].

This spherical symmetry is perhaps the most important limitation of the glue Hamiltonian when compared to other empirical many-body schemes. However, the simplification, resulting in a saving of computing power for a molecular dynamics or Monte Carlo simulation, is enormous, and should not be underestimated.

Chapter 2

Fitting the glue scheme to gold

2.1 The necessity of stringent tests

There is a large amount of arbitrariness in the glue Hamiltonian, which has so far been specified by three continuous *functions*, rather than by a handful of parameters. In the previous Chapter, we have shown some simple relations connecting the functions in the Hamiltonian with various physical quantities, such as lattice spacing, cohesive energy, defects or surface energies, elastic constants, phonon frequencies, etc. Such relations provide some fitting points for $\phi(r)$, $U(n)$, $\rho(r)$ or their derivatives at certain fixed values of the arguments, but there remains a large freedom in the shape of the functions far from these points. Therefore, it is possible to construct many different triplets of functions ϕ, U, ρ, all of which fit the same quantities, yet describe different physical systems. It may be said that in this freedom lie both the strength and the weakness of the glue Hamiltonian. One can confidently hope to find in the large space of all the possible choices a realization with overall properties similar to those of the real material. However, in order to restrict the number of candidates, some powerful selective tests need to be introduced. These tests, of course, should be able to extract new information from the Hamiltonian by probing more properties than those

that have been fitted.

Thermal properties constitute a useful test bench. In fact, when the atoms vibrate they sample wide regions of the three functions ϕ, U, ρ, so that the behaviour of the system depends on their whole shape, even relatively far from the fit points. The "thermal test" is particularly severe at high temperatures, where anharmonic effects play an important role. Properties like the thermal expansion coefficient or the melting temperature are very sensitive to tiny details in the shape of ϕ, U and ρ. For instance, the slope of the core region in the two-body potential turns out to be crucial in determining the melting temperature. Moreover, a crystal structure which is found to be stable at $T = 0$ with a certain glue Hamiltonian, may, if allowed to, undergo a transition towards another structure at a finite temperature. If this is not the case for the real material, such a Hamiltonian must be rejected. Of course, investigating the thermal properties requires the use of a molecular dynamics or Monte Carlo simulation during the glue Hamiltonian construction phase itself, just to try out successive realizations and discard the bad ones.

Another stringent test for a glue Hamiltonian is the accurate description of surface properties. The interactions between surface atoms are very different from those between bulk atoms, because the coordination is lower and therefore a different part of $U(n)$ becomes relevant. The resulting relaxation effects tend usually to reduce the bond lengths, so that also the behaviour of $\phi(r)$ and $\rho(r)$ at distances lower than the bulk first neighbour distance is important in determining the final structure. For example, the amount of first-layer contraction, when experimentally known, may be another independent quantity that can be fitted. In materials which exhibit surface reconstructions, like gold, the reconstructed surface should have a surface energy lower than the non-reconstructed surface; and the contrary should occur in materials whose surfaces do *not* reconstruct.

Thermal and surface properties depend on the details of the glue Hamiltonian in a complex way, so they are not easy to fit. However, by using molecular dynamics (MD) and a trial-and-error approach, it is possible to reproduce them rather accurately. This work requires

a suitable parametrization of ϕ, U, ρ, flexible enough to allow shape variations of the functions within the constraints given by the fit points. It should be emphasized that we are generally unable (and unwilling) to determine an "optimal" realization of the glue. The search for a Hamiltonian terminates when a satisfactory realization is found; i.e., when some previously defined "design goals" have been attained within a reasonable margin. In particular, the three functions are not expected to be meaningful for values of their arguments outside the range sampled in simulations (e.g., r deep in the core region, n near 0 or extremely large, etc.).

2.2 Details of the fit

A set of functions $\phi(r)$, $\rho(r)$, $U(n)$ aimed at reproducing gold properties as closely as possible, has been constructed accordingly to the guidelines discussed in the previous Section.

The conditions listed at the beginning of Sec. 1.7 have been adopted, so that all the relations there presented can be applied. It should be noted that

- an f.c.c. crystal structure is assumed as a starting point, but its stability is not *a priori* guaranteed and therefore it must be verified *a posteriori*.
- limiting the range of both $\phi(r)$ and $\rho(r)$ to the first neighbours proved to be a valid choice in the case of gold; but this does not imply of course that such a short range is adequate for other materials.

The following experimental data have been fitted exactly :

- $T = 0$ lattice parameter a_0.
- Cohesive energy ϵ_c.
- Surface energy σ. A $T = 0$ estimate for an "average crystal face" [48] has been fitted on a not reconstructed but relaxed (111) face.

This case has been considered to be quite typical in the case of gold, where all surfaces reconstruct in order to achieve a closely-packed structure.

- Bulk modulus B.
- Frequency of the transverse phonons at point X of the Brillouin zone $\nu_T(X)$.

Moreover, we have attempted to reproduce at least reasonably (as explained in the previous Section) the following quantities:

- Vacancy formation energy ϵ_v^F.
- Thermal expansion coefficient $\alpha = (1/a)(\partial a/\partial T)$.
- Melting temperature T_m.
- Instability of the ideal (100) surface structure, which in Au reconstructs (see Sec. 4.3).

The following analytical forms based on polynomials have been used for the three functions ϕ, ρ and U:

$$\phi(r) = \begin{cases} a_4^I(r-d)^4 + a_3^I(r-d)^3 + a_2^I(r-d)^2 \\ \quad + a_1^I(r-d) + a_0^I & \text{if } r < d \\ a_6^{II}(r-d)^6 + a_5^{II}(r-d)^5 + a_4^{II}(r-d)^4 \\ \quad + a_3^{II}(r-d)^3 + a_2^{II}(r-d)^2 + a_1^{II}(r-d) + a_0^{II} & \text{if } d \le r < r_c \\ 0 & \text{if } r_c \le r \end{cases} \tag{2.1}$$

$$\rho(r) = \begin{cases} b_3^I(r-d)^3 + b_2^I(r-d)^2 + b_1^I(r-d) + b_0^I & \text{if } r < d \\ b_3^{II}(r-d)^3 + b_2^{II}(r-d)^2 + b_1^{II}(r-d) + b_0^{II} & \text{if } d \le r < r_b \\ b_3^{III}(r-r_m)^3 + b_2^{III}(r-r_m)^2 + b_1^{III}(r-r_m) \\ \quad + b_0^{III} & \text{if } r_b \le r < r_m \\ 0 & \text{if } r_m \le r \end{cases} \tag{2.2}$$

d	$+0.2878207442141723 \times 10^{1}$	r_b	$+0.3500000000000000 \times 10^{1}$	n_0	$+0.1200000000000000 \times 10^{2}$
r_c	$+0.3700000000000000 \times 10^{1}$	r_m	$+0.3900000000000000 \times 10^{1}$	n_s	$+0.9358157767784574 \times 10^{1}$
a_0^I	$-0.8000000000000000 \times 10^{-1}$	b_0^I	$+0.1000000000000000 \times 10^{1}$	c_0^I	$-0.2793388616771698 \times 10^{1}$
a_1^I	$+0.0000000000000000$	b_1^I	-0.6800000000000000	c_1^I	-0.3420000000000000
a_2^I	$+0.7619231375231362$	b_2^I	$+0.7500000000000000$	c_2^I	$+0.3902327808424106 \times 10^{-1}$
a_3^I	-0.8333333333333333	b_3^I	$-0.1333333333333333 \times 10^{1}$	c_3^I	$+0.7558829951858879 \times 10^{-2}$
a_4^I	-0.1211483464993159	b_0^{II}	$+0.1000000000000000 \times 10^{1}$	c_4^I	$+0.3090472511796849 \times 10^{-3}$
a_0^{II}	$-0.8000000000000000 \times 10^{-1}$	b_1^{II}	-0.6800000000000000	c_0^{II}	$-0.3300000000000000 \times 10^{1}$
a_1^{II}	$+0.0000000000000000$	b_2^{II}	$+0.7500000000000000$	c_1^{II}	$+0.0000000000000000$
a_2^{II}	$+0.7619231375231362$	b_3^{II}	$-0.1527241171296038 \times 10^{1}$	c_2^{II}	$+0.8618226772941980 \times 10^{-1}$
a_3^{II}	-0.8333333333333333	b_0^{III}	$+0.0000000000000000$	c_3^{II}	$+0.4341701445034724 \times 10^{-2}$
a_4^{II}	$-0.1096009851140349 \times 10^{1}$	b_1^{III}	$+0.0000000000000000$	c_4^{II}	$-0.3044398779375916 \times 10^{-3}$
a_5^{II}	$+0.2158417178555998 \times 10^{1}$	b_2^{III}	$+0.5578188675490974 \times 10^{1}$	c_0^{III}	$-0.3300000000000000 \times 10^{1}$
a_6^{II}	-0.9128915709636862	b_3^{III}	$+0.6132971688727435 \times 10^{1}$	c_1^{III}	$+0.0000000000000000$
				c_2^{III}	$+0.8618226772941980 \times 10^{-1}$
				c_3^{III}	$+0.4325981467602070 \times 10^{-2}$

Table 2.1:
Parameters characterizing the glue Hamiltonian for gold.

$$U(n) = \begin{cases} c_4^I(n-n_s)^4 + c_3^I(n-n_s)^3 + c_2^I(n-n_s)^2 \\ \quad + c_1^I(n-n_s) + c_0^I & \text{if } n < n_s \\ c_4^{II}(n-n_0)^4 + c_3^{II}(n-n_0)^3 + c_2^{II}(n-n_0)^2 \\ \quad + c_1^{II}(n-n_0) + c_0^{II} & \text{if } n_s \le n < n_0 \\ c_3^{III}(n-n_0)^3 + c_2^{III}(n-n_0)^2 + c_1^{III}(n-n_0) \\ \quad + c_0^{III} & \text{if } n_0 \le n \end{cases} \tag{2.3}$$

The coefficients and the other parameters d, r_c, r_b, r_m, n_s, n_0 are given in Table 2.1. As will be discussed in detail in the three following Subsections, some parameters have been determined by the fit points, some by requiring continuity at the junctions, and the remaining (a dozen), controlling the shape of the functions, by the MD-based procedure discussed above.

The fit of the phonons deserves some comments. As explained previously, the phonon dispersion relations can be fitted only in an approximate way, because only two parameters are available with our first-neighbour choice. One parameter ($\phi''(d)$) is related to the two-body part, the other (the product $U''(n_0)[\rho'(d)]^2$) to the many-body part. It

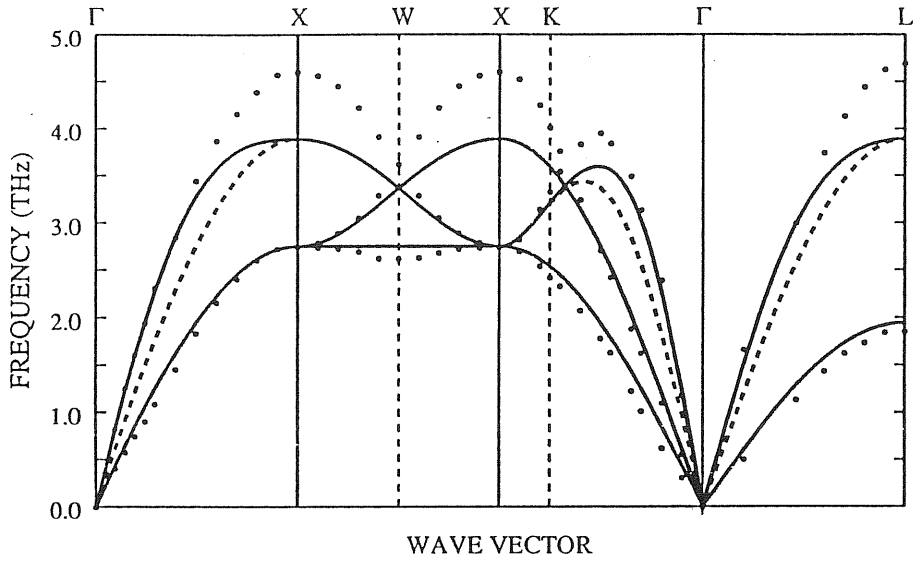

Figure 2.1:
Phonon dispersion of Au as predicted by the glue Hamiltonian, with (solid lines) and without (dashed lines) the many-body term, compared with experimental data (dots) [49]. As discussed in 1.7.2, it can be seen that the glue term affects only the longitudinal branches, and its contribution vanishes at the Brillouin zone boundary.

has been chosen to fit them to the bulk modulus and to the transverse phonon frequency at the X point, to reproduce accurately the lattice vibrations where the density of states is larger. In gold, the overall compromise turns out to be quite acceptable, as shown by the phonon dispersion in Fig. 2.1 and by Table 2.2. Clearly, a better phonon fit would have been obtained if a larger interaction range for $\phi(r)$ had been used. Attempts in this direction, however, turned out to make fitting of other properties more difficult, if not impossible.

In the following three Subsections, the details of the fit procedure are discussed for each of the three functions ϕ, ρ and U. It should be

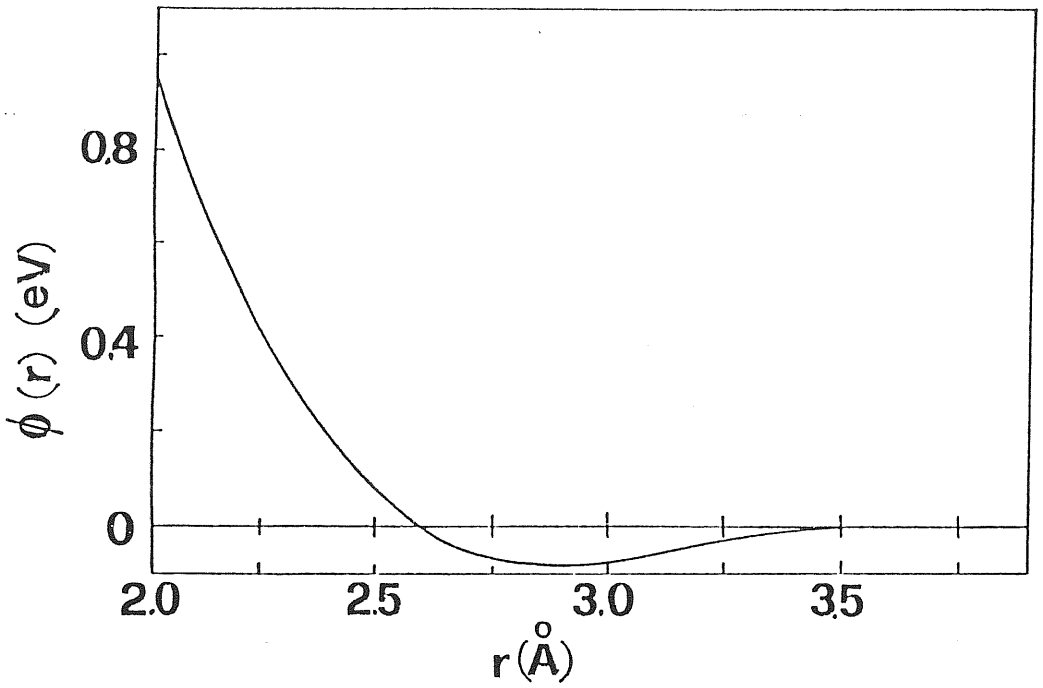

Figure 2.2:
The pair potential $\phi(r)$.

kept in mind that these details are generally dependent on the material which we are trying to reproduce, so that different materials may require a different procedure and/or different analytic forms.

2.2.1 Construction of the pair potential $\phi(r)$

The pair potential $\phi(r)$, defined by Eq. (2.1) with the parameters given in Table 2.1, is shown on Fig. 2.2.

The 12 coefficients appearing in Eq. (2.1) have been determined by the following conditions:

- $\phi(d) = \phi_0$ (supplied)
- $\phi'(d) = 0$ (lattice parameter, Eq. (1.43))

- $\phi''(d) = M\omega_T^2(X)/4$ (transverse phonons, Table 1.4)
- $\phi'''(d) = \phi'''_d$ (supplied)
- $\phi(r^*) = 1\,\mathrm{eV}$ (supplied)
- $\phi(r_c) = 0$ (going to zero smoothly at $r = r_c$)
- $\phi'(r_c) = 0$ (going to zero smoothly at $r = r_c$)
- $\phi''(r_c) = 0$ (going to zero smoothly at $r = r_c$)
- $\phi(r)$ continuous in $r = d$
- $\phi'(r)$ continuous in $r = d$
- $\phi''(r)$ continuous in $r = d$
- $\phi'''(r)$ continuous in $r = d$

Four parameters are supplied externally: ϕ_0, r_c, r^* and ϕ'''_d. ϕ_0 is the depth of the potential, which (under the condition given by Eq. (1.15)) determines the partition of the cohesion between the two-body part and the glue part. It also determines, to some extent, the anharmonicity of the potential: due to the first-neighbour constraint, a deep potential is more harmonic than a shallow one. This has visible effects, for instance, in the thermal expansion coefficient. Once ϕ_0 has been fixed, there is a very narrow range of possible values for the range r_c if wild oscillations of the derivatives of $\phi(r)$ are to be avoided. The last two parameters control the shape of the core region, which has a deep influence on melting and on surface properties. This point is discussed further in Subsection 2.2.3.

2.2.2 Construction of the function $\rho(r)$

The function $\rho(r)$, defined by Eq. (2.2) with the parameters given in Table 2.1, is shown on Fig. 2.3.

The 12 coefficients appearing in Eq. (2.2) have been determined by the following conditions:

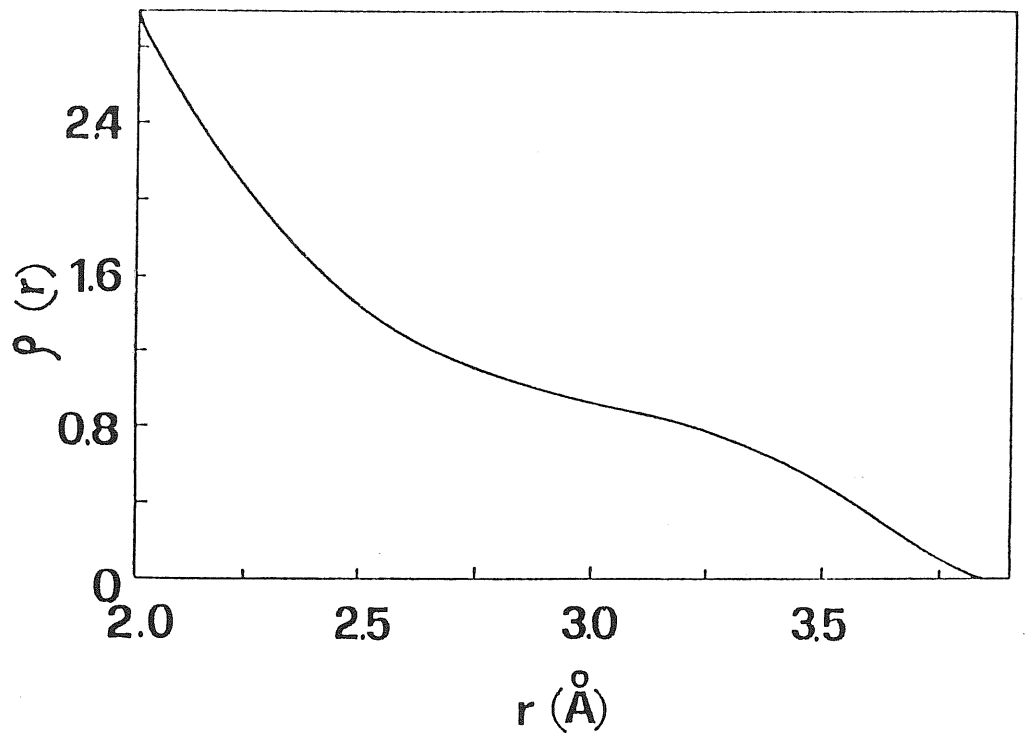

Figure 2.3:

The function $\rho(r)$.

- $\rho(d) = 1$ (normalization, Eq. (1.10))
- $\rho'(d) = \rho'_d$ (supplied)
- $\rho''(d) = \rho''_d$ (supplied)
- $\rho'''(d) = \rho'''_d$ (for $r < d$) (supplied)
- $\rho(r_b) = \rho_b$ (supplied)
- $\rho(r_m) = 0$ (going to zero smoothly at $r = r_m$)
- $\rho'(r_m) = 0$ (going to zero smoothly at $r = r_m$)
- $\rho(r)$ continuous in $r = d$
- $\rho'(r)$ continuous in $r = d$
- $\rho''(r)$ continuous in $r = d$
- $\rho(r)$ continuous in $r = r_b$
- $\rho'(r)$ continuous in $r = r_b$

Here, six parameters are supplied externally: r_m, r_b, ρ_b, ρ'_d, ρ''_d, and ρ'''_d. This leaves a great freedom in determining the shape of this function.

It is worthwhile to note that $\rho(r)$ itself cannot fit any physical property, since it operates "within" $U(n)$ in the hamiltonian. Only suitable combinations of $\rho(r)$ and $U(n)$ are related to quantities of the physical system. One of such combinations is Eq. (1.46) for the bulk modulus. From this equation, it is seen that the choice of ρ'_d is quite important, because fitting the bulk modulus then forces a particular value for $U''(n_0)$, $\phi''(d)$ being fixed by the transverse phonons. This value for $U''(n_0)$ may result to be incompatible with the general behaviour of $U(n)$, which is governed by other considerations such as the surface energy fitting (as discussed in 2.2.3). Actually, the inverse route has been followed: first, a reasonable value for $U''(n_0)$ is selected, then ρ'_d is determined by fitting the bulk modulus. This requires a sort of self-consistency in the fitting

process, since $U(n)$, as explained in the next Subsection, must be constructed after $\rho(r)$, and only at this last stage it is apparent whether the original choice for $U''(n_0)$ was really good or not. A valid, if qualitative, quality test is the smoothness of $U'(n)$ and $U''(n)$, i.e., they should be free from spurious oscillations.

The value for ρ'_d resulting from this procedure gives a rather flat curve around $r = d$. The shape of $\rho(r)$ seen in Fig. 2.3 is the result of the competition between this small slope around $r = 3$ Å and the short-range requirement. The "cutoff region" between $r_b = 3.5$ Å and $r_m = 3.9$ Å has been located in correspondence with the minimum between the first- and the second-neighbour shell in the pair correlation function (as determined by high temperature simulations). In this way, the effect of this region on the properties of the system has been reduced to a minimum.

The control provided by the two parameters ρ''_d and ρ'''_d permits to adjust the shape of $\rho(r)$ in the very important region around $r = d$, which determines how the atoms gain and lose coordination when their mutual distances are varied. Since the energies associated with coordination changes are large, slight modifications on $\rho(r)$ around the first-neighbour distance can easily induce dramatic changes in the thermal behaviour and in the surface properties. For example, the presence of surface reconstructions can be switched on or off by acting on $\rho(r)$ for $r < d$.

2.2.3 Construction of the glue function $U(n)$

The "glue" function $U(n)$, defined by Eq. (2.3) with the parameters given in Table 2.1, is shown on Fig. 2.4.

The 14 coefficients appearing in Eq. (2.3) have been determined by the following conditions:

- $U(0) = 0$ (by definition, Eq. (1.6))
- $U(n_0) = U_0$ (cohesive energy, Eq. (1.44))
- $U'(n_0) = 0$ (Eq. (1.15))

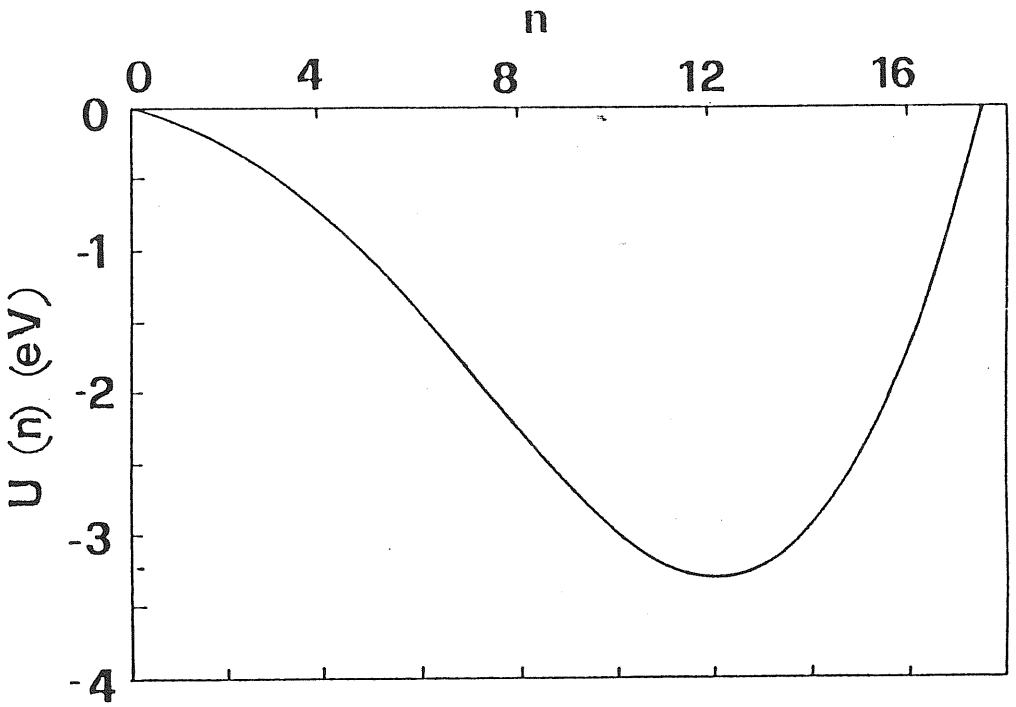

Figure 2.4:
The "glue" function $U(n)$.

- $U''(n_0) = U_0''$ (bulk modulus, Eq. (1.46))
- $U(n^*) = 0$ (supplied)
- $U(n_s) = U_s$ (surface energy, Eq. (2.4))
- $U'(n_s) = U_s'$ (supplied)
- $U(n)$ continuous in $n = n_0$
- $U'(n)$ continuous in $n = n_0$
- $U''(n)$ continuous in $n = n_0$
- $U(n)$ continuous in $n = n_s$
- $U'(n)$ continuous in $n = n_s$
- $U''(n)$ continuous in $n = n_s$
- $U'''(n)$ continuous in $n = n_s$

Here, $n_0 = 12$ (bulk coordination), and n_s is the first layer coordination on a relaxed (111) surface (defined below). Only two parameters are supplied externally: n^* and U_s'. n^* is greater than n_0 and controls the shape of $U(n)$ for large coordinations. For gold, the value chosen ($n^* = 17.48$) is such that the glue function rises rather rapidly above $n = n_0$. This rise corresponds to a sort of core-core repulsion, but obtained through the glue term instead of the two-body term. This peculiar behaviour solves the following problem. In order to obtain a system with the correct melting temperature, the core region of the two-body potential should be soft enough to allow large vibrational amplitudes of the atoms. Such a "soft" system, however, would not be enough anharmonic to yield a realistic thermal expansion. A potential with a hard core region, on the other hand, gives a system which expands well but is too stiff and melts at a temperature which is too high. In the gold realization described here, the potential is soft and the anharmonicity is supplied by the glue: at high temperatures, in fact, the shape of the glue around $n = n_0$ favours fluctuations which tend to decrease, rather

than increase, the local coordination. The system reacts by increasing slightly the lattice parameter.

The surface energy fit also deserves some comments. Once $\phi(r)$ has been assigned, $U(n_0)$ is known by fitting the cohesive energy (Eq. (1.44)) and at this point $U(9)$ can be calculated using the expression (1.48) for the surface energy of a (111) face. However, this expression refers to an unrelaxed surface; relaxations raise the first layer coordination above 9, thus reducing the effective surface energy. To avoid this problem, a more sophisticated fitting procedure must be adopted. Assuming that only the distance between the first and the second layer is varied from the unrelaxed value $s_0 = \sqrt{2/3}d$ to a certain value s, the expression for the surface energy per atom can be generalized as follows:

$$\epsilon_s(s) = -\frac{9}{2}\phi(d) + \frac{6}{2}\phi(d') + \frac{6}{2}\phi(a') + U(n_s) + U(n_2) - 2U(n_0) \quad (2.4)$$

where d is the bulk first-neighbour distance, $d' = \sqrt{s^2 + d^2/3}$ the distance between an atom in the first layer and a first neighbour in the second layer, $a' = \sqrt{s^2 + 4d^2/3}$ the distance between an atom in the first layer and a second neighbour in the second layer, $n_s = 6\rho(d) + 3\rho(d') + 3\rho(a')$ the first layer coordination, and $n_2 = 9\rho(d) + 3\rho(d') + 3\rho(a')$ the second layer coordination. Some second-neighbour terms are present because, due to a possible contraction, it is not guaranteed that a' is larger than the range of $\phi(r)$ or $\rho(r)$. (2.4) is more complicated than (1.48), but can be straightforwardly calculated for a given value of s.

Our fitting procedure self-consistently solves the two equations

$$\begin{aligned} \epsilon_s(s) &= \sigma A \\ \epsilon_s'(s) &= 0 \end{aligned} \quad (2.5)$$

where σ is the experimental surface energy per unit area and $A = d^2\sqrt{3}/2$ is the area occupied by an atom. Equations (2.5) ensure that the correct surface energy is obtained in correspondence with the equilibrium relaxation. They are solved by using the following iterative method:

1. Build the region of $U(n)$ with $n > n_0$; this can be done from the initial conditions, and will never be changed.

2. Assume an initial value for s.

3. Given s, calculate d', a', n_s and n_2.

4. Solve Eq. (2.4) for $U(n_s)$. Note that $U(n_2)$ is known, since $n_2 > n_0$. This gives the condition $U(n_s) = U_s$.

5. Now all the coefficients of $U(n)$ can be determined, so that $U(n)$ becomes known for all values of n.

6. Solve $\epsilon_s'(s) = 0$. This yields a solution $s' \neq s$.

7. If $|s - s'| < \varepsilon_s$ and $|\epsilon_s(s) - \epsilon_s(s')| < \varepsilon_\epsilon$ (where ε_s and ε_ϵ are very small tolerances) then terminate, otherwise rename s' as s and go back to step 3.

Note that the final shape for $U(n)$ is controlled by the parameter U_s' which is supplied externally. If a reasonable value is given to this parameter, the procedure converges within ten iterations. Relaxation effects between the second and the third layer and between deeper layers, neglected by this method, lead to a very small (-0.2%) correction, as a molecular dynamics calculation established later. This correction is surely negligible in comparison with the error associated with the experimental estimate of the surface energy [48].

2.3 Comparison with experiment

Many physical quantities of gold as predicted by the fit are compared with experiment in Table 2.2. The calculations of the thermal expansion coefficient, the bulk melting properties, and the vacancy parameters, are presented respectively in Sections 3.1, 3.2 and 3.4.

From the table, it can be seen that modelling of gold is fairly accurate on the whole. In particular, all the quantities difficult to fit with two-body forces, which we have discussed in Sec. 1.1, are now well reproduced.

Quantity	*Glue model*	*Experimental*	*Ref.*
$T = 0$ Lattice parameter a_0 (Å)	4.07*	4.07	[50]
Cohesive energy ϵ_c (eV/atom)	3.78*	3.78	[9]
Surface energy σ (meV/Å^2)	96.6*	96.8	[48]
Vacancy formation energy ϵ_v^F (eV)	1.26	0.94	[51]
Vacancy migration energy ϵ_v^M (eV)	0.98	0.85	[51]
Bulk modulus B (10^{12} dyne/cm^2)	1.803*	1.803	[52]
C_{11} (10^{12} dyne/cm^2)	2.203	2.016	[52]
C_{12} (10^{12} dyne/cm^2)	1.603	1.697	[52]
C_{44} (10^{12} dyne/cm^2)	0.600	0.454	[52]
$\nu_L(X)$ (THz)	3.89	4.61	[49]
$\nu_T(X)$ (THz)	2.75*	2.75	[49]
$\nu_\Pi(W)$ (THz)	3.37	3.63	[49]
$\nu_\Lambda(W)$ (THz)	2.75	2.63	[49]
$\nu_L(L)$ (THz)	3.89	4.70	[49]
$\nu_T(L)$ (THz)	1.94	1.86	[49]
Th. exp. coeff. α at 773 K (10^{-6} K^{-1})	13.8*	15.2	[53]
Heat capacity C_p at 1200 K (10^{-4} eV/K/atom)	3.1	3.09	[53]
Melting temperature T_m (K)	1357*	1336	[53]
Entropy of melting S_m (k_B/atom)	1.0	1.13	[10]
Latent heat of melting ΔH_m (eV/atom)	0.12	0.13	[10]
Volume change on melting $\Delta V/V_s$ (%)	0.6	5.2	[10]
* fitted			

Table 2.2:

Comparison between some experimental quantities of gold and the same quantities as predicted by the glue model. The fit is not always exact, owing to the procedure used (see text). σ (referring to a non-reconstructed (111) surface), ϵ_v^F and ϵ_v^M are calculated at $T = 0$ and include relaxation effects. α, T_m, S_m and ΔH_m are determined by zero-pressure molecular dynamics simulations.

Chapter 3

Molecular dynamics studies of bulk properties

3.1 f.c.c. stability and bulk thermal expansion

As mentioned in Sec. 2.2, several properties of the bulk at finite temperature were monitored during the construction of the three functions characterizing the glue Hamiltonian.

To this end, the Parrinello-Rahman molecular dynamics technique [54] has been extensively used (for a general survey on molecular dynamics, see Ref. [55]). In this method, the box containing the particles (and extended to infinity through periodic boundary conditions) can vary in volume and shape, under the action of the internal stress and, if present, an externally applied pressure or anisotropic stress. It has been shown [54] that changes in the shape of the box allow the (previously impossible) observation by molecular dynamics of solid-solid transformations, such as that of an f.c.c. crystal into a b.c.c. and vice versa. These phase transformations can be induced by applying external forces, but they may also occur spontaneously if at a certain temperature the two phases have the same free energy [56].

The stability of the f.c.c. structure of gold (as described by our glue

Hamiltonian) against the b.c.c. structure [1] has been therefore verified up to the melting temperature through Parrinello-Rahman simulations in the absence of pressure or stress.

The same calculation also gives directly the lattice parameter a as a function of temperature. Within the accuracy allowed by our trial-and-error procedure, we have tried to reproduce the experimental data as closely as possible by making changes on the shapes of the functions. The result for the final choice is shown in Fig. 3.1. The agreement between the model and experiment is fairly good.

3.2 Melting point

The melting temperature has been determined by computer simulation. A bulk simulation is not well suited for this purpose because, lacking any defects, it undergoes overheating and supercooling, i.e., it exhibits a large hysteresis effect which makes it difficult to locate even approximately the melting point [29,57]. A system with a free surface overcomes this problem, because the melt can easily nucleate at or near the surface and then propagate into the bulk [28,29,136].

In order to determine the melting temperature, the following procedure has been adopted. A system with a free surface is heated until a spontaneous nucleation of the liquid phase occurs at or near the surface. The system is then kept hot, to allow for the motion of the liquid-solid interface into the bulk. In this way we produce a sample with a liquid phase and a solid phase simultaneously present, although not in perfect equilibrium. Starting from this sample, the melting temperature, at which by definition the liquid-solid interface remains stationary, is searched by trial-and-error.

The melting temperature is a function of the pressure or, more generally, of the stress applied on the system. We have kept the stress

[1] The f.c.c.-h.c.p. stability is more delicate, because it involves atom displacements relative to the box, as well as variations in the box shape [54]. No conclusion can be drawn about this point. Note that at $T = 0$, with the glue Hamiltonian, the f.c.c. is favoured over the b.c.c., while f.c.c. and h.c.p. have the same energy.

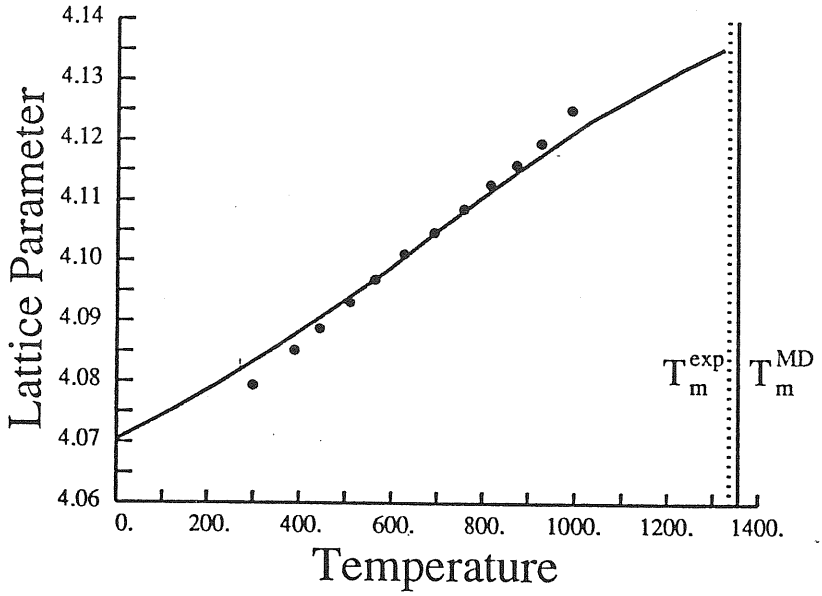

Figure 3.1:
Lattice parameter a of Au as a function of temperature. Molecular dynamics simulation data (solid line) are compared with experiment (dots) [50]. The vertical lines represent the calculated (solid line) (see Chapter 5) and experimental (dotted line) melting temperature.

equal to zero by adjusting the lattice parameter of the crystalline phase to match the value obtained by the thermal expansion curve at each temperature. This is done by scaling of the molecular dynamics cell. The liquid is not under pressure due to the presence of the free surface.

The melting temperature, as discussed in Sec. 2.2, is one of the quantities our glue Hamiltonian has been fitted to. However, a precise determination of the bulk melting point is computationally quite expensive. In fact, when T is near T_m the solid-liquid interface moves very slowly, so that long simulation times become necessary to detect the motion. For this reason, T_m was monitored rather roughly (with an accuracy around 5%) when constructing the Hamiltonian.

A much more accurate determination has been done later, in the context of a study aimed at detecting the possible existence of surface melting on the Au(111) surface. This study is fully detailed in Chapter 5, and we report in this Section only the results related to bulk melting. The resulting value for the melting temperature is

$$T_m = 1357 \pm 5\,\mathrm{K}$$

At $T = 1350\,\mathrm{K}$, the liquid-solid interface moves in the direction of the solid, eventually leading to a complete recrystallization of the sample, while at $T = 1360\,\mathrm{K}$, the melt is seen to proceed into the bulk. The estimate of the melting temperature is based on the different interface velocities observed at these two temperatures. To achieve an accuracy of $\pm 5\,\mathrm{K}$, the simulation time scale must be of the order of ~ 50000 time steps, or $\sim 0.5\,\mathrm{ns}$. The value obtained for T_m is in good agreement with the experimental value, $T_m(\mathrm{exp}) = 1336\,\mathrm{K}$.

The latent heat of fusion has been also estimated by comparing the average energy per particle in the liquid and in the solid phase. The result is

$$\Delta H = 0.12 \pm 0.01\,\mathrm{eV/atom}$$

The entropy change on fusion is therefore

$$S_m = \Delta H / T_m = 1.0 \pm 0.1\,\mathrm{k_B/atom}$$

These values are only slightly lower ($\sim$ 10%) than the experimental values (see Table 1.1 on page 7), which is very gratifying.

The volume change on melting has also been estimated. In this case, the value obtained (0.6%) is one order of magnitude smaller than the experimental value (5.2%, from Table 1.1). We can attribute this discrepancy tentatively to the extreme softness of the core of our two-body potential.

3.3 Liquid structure

With the exception of the melting temperature, properties of the liquid phase have not been taken into account when building the parametrization of the glue Hamiltonian for gold. Nonetheless, it is interesting to study how our Hamiltonian reproduces structural and thermodynamic properties of bulk liquid Au. This study constitutes an additional test of the model, and may also indicate if the present approach is well suited for computer simulations of liquid metals.

The results described in this Section have been obtained by molecular dynamics. For liquid simulations, the Parrinello-Rahman technique mentioned in Sec. 3.1 does not offer particular advantages compared with traditional methods where the box has a fixed shape. In fact, in a solid, small deformations cause restoring elastic forces to arise, so that the box shape oscillates around an equilibrium shape. In a liquid, on the other hand, no force reacts to deformations, and the box shape in a Parrinello-Rahman simulation "wanders" randomly. For this reason, the simpler constant-pressure Andersen method [58] has been used. In this method, the box may still vary in volume, but shape variations are not allowed.

In all computations, the box, extended to infinity in all the directions by periodic boundary conditions, contains 500 particles and the external pressure is set to zero.

3.3.1 Diffusion

A series of MD runs has been performed to investigate thermodynamics properties of liquid Au at zero pressure. In each run, the system is first equilibrated for 2500 steps at constant enthalpy E, then several data are collected in the subsequent 2500 steps. Table 3.1 reports the temperature T, self-diffusion coefficient D, atomic volume Ω and coordination n (as defined by Eq. (1.7)), for each run at a given enthalpy E. T is proportional to the kinetic energy, averaged (as Ω and n) both on particles and time. The self-diffusion coefficient D has been extracted by using the relation [59]

$$\left\langle |\vec{r}(t) - \vec{r}(0)|^2 \right\rangle = 6Dt, \tag{3.1}$$

averaged on the 500 atoms in the sample.

The table goes beyond the experimental evaporation temperature of gold, $T_e(\text{exp}) = 3081\,\text{K}$. No attempt to determine T_e in the glue model has been made. Therefore, some high-temperature points reported in Table 3.1 might refer to an overheated liquid. On the other hand, points with $T < T_m = 1357\,\text{K}$ surely refer to an undercooled liquid.

It is very well known that in solids the temperature dependence of the diffusion coefficient is well reproduced by an Arrhenius-type law

$$D = A\mathrm{e}^{-Q/k_B T}, \tag{3.2}$$

with (possibly) small deviations near the melting temperature (see Sec. 3.4). In liquids, on the other hand, deviations from this law are quite common [60]. The Arrhenius plot of our calculation, shown in Fig. 3.2, exhibits a linear behaviour up to a temperature $T^* \simeq 1850\,\text{K}$, with

$$A = 207 \times 10^{-6}\,\text{cm}^2/\text{s}, \quad Q = 0.315\,\text{eV}$$

Progressively higher deviations occur at higher temperatures.

Unfortunately, no experimental values have been found in literature for liquid gold. Data reported for other noble metals [61], collected in a temperature range just above T_m, show comparable values for Q:

$$\begin{aligned} &\text{Cu(exp)}: \quad A = 1460 \times 10^{-6}\,\text{cm}^2/\text{s}, \quad Q = 0.421\,\text{eV} \\ &\text{Ag(exp)}: \quad A = 580 \times 10^{-6}\,\text{cm}^2/\text{s}, \quad Q = 0.332\,\text{eV} \end{aligned}$$

E (eV/atom)	T (K)	D (10^{-6} cm^2/s)	Ω (Å^3)	n
−3.600	315	0.11	17.466	11.9
−3.550	496	0.16	17.549	11.8
−3.500	660	0.45	17.624	11.8
−3.450	820	2.4	17.672	11.8
−3.400	961	4.7	17.712	11.7
−3.350	1110	8.2	17.732	11.7
−3.300	1268	11.6	17.763	11.7
−3.250	1430	16.2	17.803	11.6
−3.200	1587	21.7	17.836	11.6
−3.150	1756	26.3	17.881	11.6
−3.100	1923	32.3	17.918	11.5
−3.050	2091	44.0	17.966	11.5
−3.000	2266	52.7	18.025	11.5
−2.950	2440	61.8	18.078	11.5
−2.900	2618	76.0	18.125	11.4
−2.850	2801	74.1	18.208	11.4
−2.800	2983	87.4	18.266	11.4
−2.750	3165	111.	18.337	11.4
−2.700	3346	112.	18.415	11.3
−2.650	3543	115.	18.490	11.3
−2.600	3736	132.	18.573	11.3
−2.550	3921	150.	18.654	11.2
−2.500	4113	156.	18.742	11.2

Table 3.1:

Total enthalpy per atom E, temperature T, self-diffusion coefficient D, atomic volume Ω and coordination n (defined by Eq. (1.7)) as averaged in zero-pressure molecular dynamics runs.

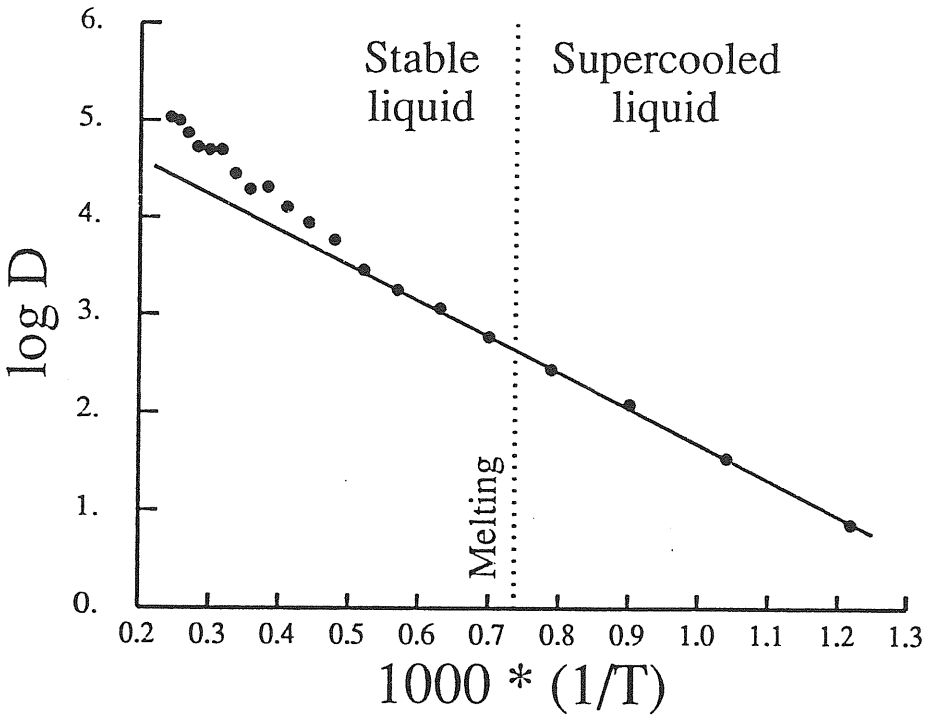

Figure 3.2:

Arrhenius plot ($\log D$ vs. $1/T$) of the diffusion coefficient of liquid Au in the glue model as a function of temperature. The points are the simulation data, the solid (straight) line is a fit at low temperatures.

The specific heat at constant (zero) pressure $C_p = (\partial E/\partial T)_p$, extracted from Table 3.1 in a wide region near T_m, is $C_p = 3.1 \times 10^{-4}$ eV/K/atom. This result is in almost perfect agreement with experiment, $C_p(\mathrm{exp}) = 3.04 \times 10^{-4}$ eV/K/atom [62].

The glue model, on the other hand, fails in predicting the thermal expansion coefficient of liquid Au. The value extracted from Table 3.1, $(1/\Omega)(\partial\Omega/\partial T) \simeq 17 \times 10^{-6}\,\mathrm{K}^{-1}$, is lower than the experimental value, $(1/\Omega)(\partial\Omega/\partial T)(\mathrm{exp}) \simeq 86 \times 10^{-6}\,\mathrm{K}^{-1}$ [62], by about a factor 5. This problem, together with the low volume change on melting mentioned in Sec. 3.2, indicates that the repulsive (core) part of the potential at short distances is probably too soft.

3.3.2 Pair correlation function

The pair correlation function $g(r)$ of the liquid predicted by the glue Hamiltonian has been also calculated using molecular dynamics. The conditions assumed are zero pressure and a temperature of 1600 K.

Starting from a crystalline state, the system is brought at $T = 2000$ K in order to melt quickly. After 3000 steps of equilibration, the temperature is decreased to 1600 K, and the system is equilibrated again for 3000 steps. The pair correlation function has been measured in the subsequent 1000 steps, and the result is shown on Fig. 3.3, compared with the experimental $g(r)$ at $T = 1573$ K [63]. There is a substantial agreement on the position, height and width of the first peak. The calculated $g(r)$ has, however, the first minimum too deep, and the second shell slightly too close when compared with the experimental $g(r)$.

As a final observation, it may be noted from $g(r)$ that the distance between a pair of particles, in practice, is always larger than 2 Å; in this simulation it is also seen that the distribution of the coordinations n (in the glue Hamiltonian sense) of the atoms is confined in the interval 9–14 (with an average value of 11.6). At surfaces, the lower bound of the coordination distribution decreases to about 7. As discussed at the end of Sec. 2.1, these values indicate the limits of validity for the functions in the glue Hamiltonian: we do not expect that modifications made to

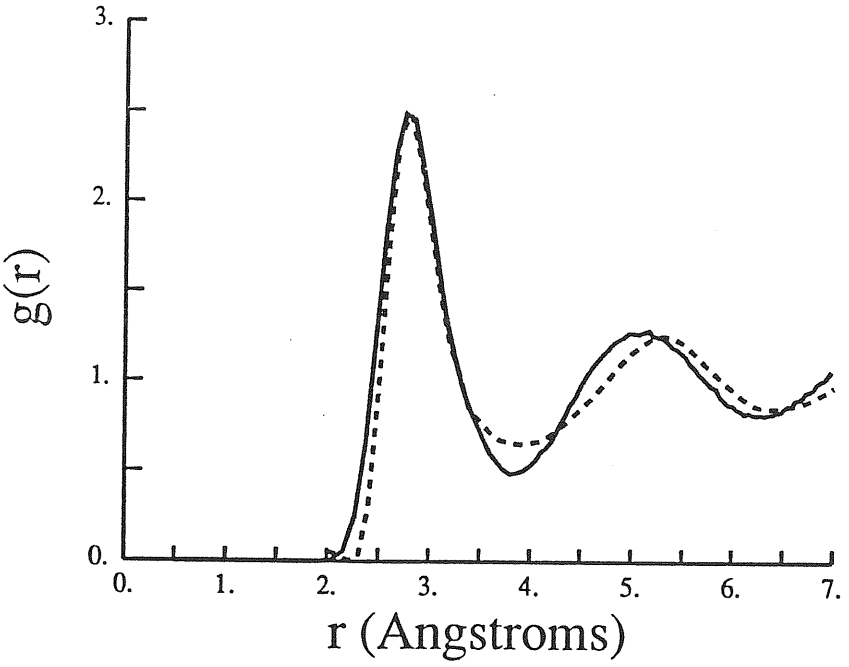

Figure 3.3:
Calculated (solid line, 1600 K) and experimental (dashed line, 1573 K) [63] pair correlation function $g(r)$ of liquid gold.

these functions out of the ranges sampled in simulations would yield visible effects on the properties of the system. The validity range can be thus summarized: $r > 2$ Å, $7 < n < 14$.

3.4 Vacancy properties at $T = 0$

Gold is one of the most studied metals from the point of view of point defect properties [51,64,65]. However, several aspects of its vacancy properties are still controversial and justify further theoretical studies.

Two-body force models are certainly inadequate to study vacancies in metals, for the reasons discussed in Section 1.1. The present glue model, on the other hand, reproduces fairly well defect energies and the temperature behaviour, and offers a suitable framework for this kind of studies. A full, detailed investigation of vacancy properties, aiming at characterizing temperature-dependent properties, is currently in progress [66]. In this Section, we report some preliminary results on $T = 0$ properties of a monovacancy in gold.

3.4.1 Vacancy formation

As already stated in Sec. 1.1, the vacancy formation energy is given by

$$\epsilon_v^F = E_N^v - E_N$$

where E_N is the energy of a system with N particles in N perfect crystal sites, while E_N^v is the energy of a system with N particles in $N+1$ crystal sites, that is, when a vacancy is present. In the same terms we can define the vacancy formation volume:

$$\Omega_v^F = \Omega_N^v - \Omega_N$$

Neglecting relaxations, the formation energy predicted by the glue Hamiltonian can be calculated using Eq. (1.47). This gives $\epsilon_{v,0}^F = 1.458$ eV which is about 50% higher than the experimental value, $\epsilon_v^F(\mathrm{exp}) = 0.94$ eV [51]. Atom relaxations around the vacancy, however, reduce the formation energy.

Relaxations effects have been included by using molecular dynamics. The procedure consists in performing a simulated quenching, where the atoms are moved accordingly to the instantaneous forces but their velocities are rescaled by a factor $\alpha < 1$ at every time step of the simulation. In this way, kinetic energy is continuously removed until the system eventually reaches a stationary state, where all the atoms are at rest in their relaxed equilibrium positions and the energy is minimized.

A problem lies in the fact that a point defect in a crystal generates an elastic strain which at large distances falls as $1/r^3$ [67], but in molecular dynamics calculations the range of the distortion is limited by the size of the computational box (subjected to the usual periodic boundary conditions), so that long-range contributions are lost. However, these contributions can be estimated by noting that the density of elastic energy $w(r)$ at a distance r from the defect decays like $1/r^6$ (the square of the strain). Therefore, the total elastic energy $W(R)$ associated to deformations at distances $r > R$ falls, for large R, as

$$W(R) \simeq \int_R^\infty 4\pi r^2 w(r)\, dr \sim \frac{1}{R^3} \tag{3.3}$$

For this reason, we expect that vacancy formation energy calculations performed on a cubic box of size La (where a is the lattice parameter) should exhibit a dependence on L of the kind

$$\epsilon_v^F(L) \simeq \bar{\epsilon}_v^F + \frac{A}{L^3} \tag{3.4}$$

By fitting this relation to the values of $\epsilon_v^F(L)$ extracted from the simulations, the asymptotic term $\bar{\epsilon}_v^F$ can be reasonably estimated.

Two sets of calculations have been performed, one (CL) at constant lattice spacing and one (ZP) at zero pressure, with $L = 3, 4, 5, 6$, and $N = 4L^3 - 1 = 107, 255, 499, 863$.

CL In this set (constant lattice spacing), the volume of the box is kept fixed accordingly to the $T = 0$ lattice spacing of the perfect crystal. This corresponds to imposing a vacancy formation volume equal to the atomic volume Ω_0. The resulting energies are given in the second column of Table 3.2, while in the third column these

L	$\epsilon_v^F(L)$	Eq. (3.4)
3	1.3013	1.3012
4	1.2787	1.2788
5	1.2705	1.2708
6	1.2676	1.2673

Table 3.2:

Vacancy formation energies ϵ_v^F (in eV) from constant lattice spacing (CL) calculations, and best fit from Eq. (3.4).

L	$\epsilon_v^F(L)$	Eq. (3.4)	$\Delta a/a_0$	Ω_v^F/Ω_0
3	1.2383	1.2383	−0.27	0.1408
4	1.2518	1.2520	−0.11	0.1459
5	1.2567	1.2569	−0.06	0.1476
6	1.2592	1.2590	−0.03	0.1484

Table 3.3:

Vacancy formation energies ϵ_v^F (in eV) from zero pressure (ZP) calculations, best fit from Eq. (3.4), corresponding lattice parameter variation $\Delta a/a_0$ (in %) and vacancy formation volume in atomic volume units.

energies have been fitted by Eq. (3.4), with $\bar{\epsilon}_v^F = 1.2624\,\text{eV}$ and $A = +1.0482\,\text{eV}$.

ZP In this set, the volume of the box is allowed to vary in order to compensate the internal pressure induced by the vacancy, so that the system is at zero pressure. In this case, the vacancy formation volume becomes less than Ω_0 and can be measured. The results are given in Table 3.3. The fit parameters in Eq. (3.4) are $\bar{\epsilon}_v^F = 1.2620\,\text{eV}$ and $A = -0.6404\,\text{eV}$.

As seen from the above Tables, CL calculations overestimate the formation energy, while ZP calculations underestimate it. The explanation

lies probably in the fact that in ZP, the attractive interaction between the vacancy and the other image vacancies in the nearby computational boxes is stronger than in CL, where it is almost cancelled by the constant volume constraint. The two sets are in remarkable agreement as for the value of $\bar{\epsilon}_v^F$. Dropping the last digit, we can thus assume

$$\epsilon_v^F = 1.262\,\mathrm{eV}$$

as the vacancy formation energy predicted by the glue Hamiltonian. This value is larger than the experimental value (0.94 eV), but the agreement can still be regarded as reasonably good, particularly if we recall (from Sec. 1.1) that two-body forces would predict $\epsilon_v^F \sim \epsilon_c = 3.78$ eV !

From ZP data we obtain also

$$\Omega_v^F = 0.15\Omega_0$$

as the vacancy formation volume, which is only weakly dependent on the box size. This value appears to be small when compared with the experimental value, $\Omega_v^F(\mathrm{exp}) \simeq 0.5\Omega_0$ [64]. This signifies an excess of relaxation in our model.

Finally, the relaxations of the first four atomic shells around the vacancy in the case $L = 5$ are given in Table 3.4, together with the atomic coordinations n (in the glue Hamiltonian sense). It can be seen that all the four shells move towards the vacancy. It is interesting to note [68] that in two-body systems with interactions not limited to the first neighbours, the first shell relaxes towards the vacancy but the other shells move away from it.

3.4.2 Vacancy migration

The vacancy migration energy ϵ_v^M is defined as

$$\epsilon_v^M = E_N^s - E_N^v \tag{3.5}$$

where E_N^v is the energy of the crystal with the vacancy in the equilibrium position, and E_N^s the energy at the saddle point of the potential

Shell	R	ΔR	n
CL			
1	2.8324	-0.0458	11.205
2	4.0205	-0.0499	12.109
3	4.9447	-0.0405	12.041
4	5.7255	-0.0309	12.009
ZP			
1	2.8298	-0.0484	11.219
2	4.0184	-0.0520	12.123
3	4.9416	-0.0436	12.055
4	5.7220	-0.0344	12.022

Table 3.4:

Distance R from the vacancy (in Å), relaxation ΔR respect to the unrelaxed distance (in Å) and coordination n for the first four atomic shells around the vacancy. *CL* indicates the constant lattice spacing calculation, *ZP* the zero pressure calculation.

energy surface in configuration space. This saddle point separates the two regions corresponding to the vacancy being located in one of two neighbouring lattice sites. In other words, ϵ_v^M is the energy barrier associated with the jump of an atom into a vacant site.

The vacancy migration volume Ω_v^M is defined by the similar relation

$$\Omega_v^M = \Omega_N^s - \Omega_N^v. \tag{3.6}$$

ϵ_v^M and Ω_v^M have been determined by a relaxation procedure similar to that described in the previous Subsection. The saddle point configuration is produced by constructing a crystal with a vacancy equally split between two neighbouring sites. This means that an atom near the vacancy has been moved to a position halfway between the vacancy and its original lattice site. This configuration is then relaxed by the quench procedure. The "jumping" atom remains on the saddle surface without additional constraints, as a consequence of the high symmetry of the initial condition [2].

The results, for the case $L = 4$ (255 atoms), *not* corrected for size effects, are

$$\epsilon_v^M = 0.98\,\mathrm{eV}$$

and

$$\Omega_v^M = -0.28\Omega_0.$$

While ϵ_v^M is in good agreement with the experimental estimate, $\epsilon_v^M(\mathrm{exp}) = 0.85$ eV [51], the negative value found for Ω_v^M is rather unusual, and disagrees with the experimental estimate $\Omega_v^M(\mathrm{exp}) \simeq 0.15\Omega_0$ [64]. Once again, this seems an effect due to excessive relaxation.

3.4.3 Isotope effect

If we assume that the main mechanism of self-diffusion in metals is through jumps of monovacancies, the diffusion coefficients D_α and D_β

[2] Numerical roundoff errors in the computation destroy the symmetry, so that the atom may "fall" into one of the two wells in a long simulation run. The quench procedure must be quick enough to prevent this.

of two isotopes α and β are related by [69,70]

$$\frac{D_\alpha}{D_\beta} - 1 = f\left(\frac{\Gamma_\alpha}{\Gamma_\beta} - 1\right) \tag{3.7}$$

where Γ_α, Γ_β are the vacancy jump frequencies, and f is the correlation factor for monovacancy self-diffusion, which in f.c.c. crystals has the constant value 0.781 [71].

Accordingly to classical harmonic rate theory [72], the jump frequency is given by

$$\Gamma_\alpha = \frac{1}{2\pi}\frac{\prod_{i=1}^{3N}\omega_i}{\prod_{i=1}^{3N-1}\omega_i'}\exp(-\epsilon_v^M/k_BT) \tag{3.8}$$

where ω_i are the eigenfrequencies of the system at the equilibrium position, and ω_i' are the eigenfrequencies at the saddle point. The imaginary frequency relative to the reaction coordinate, ω_{3N}', is not included in the product at the denominator.

From this relation, since the ω's scale as $M_\alpha^{-1/2}$ (where M_α is the mass of isotope α) and ϵ_v^M does not depend on mass, we may write

$$\frac{\Gamma_\alpha}{\Gamma_\beta} = \left(\frac{M_\beta}{M_\alpha}\right)^{1/2} \tag{3.9}$$

and conclude that

$$\frac{D_\alpha}{D_\beta} - 1 = f\left[\left(\frac{M_\beta}{M_\alpha}\right)^{1/2} - 1\right] \tag{3.10}$$

However, we are implicitly assuming here that the movement of the jumping atom is completely decoupled from the other atoms in the lattice.

Coupling to other atoms reduces the sensitivity of diffusion rates to the isotope mass. Other atoms also move during the jump, and it is no longer true that the ω's scale as $M_\alpha^{-1/2}$, which refer only to the jumping atom. A more realistic relation is

$$\frac{D_\alpha}{D_\beta} - 1 = f\Delta K\left[\left(\frac{M_\beta}{M_\alpha}\right)^{1/2} - 1\right] \tag{3.11}$$

where ΔK is a factor < 1, which can be shown [73,74] to be the fraction of the kinetic energy associated with motion in the jump direction, which belongs to the jumping atom.

A lattice dynamics evaluation of the *isotope effect factor* ΔK can be simply carried out as [75]

$$\Delta K = \frac{(\vec{n} \cdot \vec{u}_1)^2}{\sum_{i=1}^{N} (\vec{n} \cdot \vec{u}_i)^2} \tag{3.12}$$

where $\vec{n}$ is the unit vector in the jump direction, $\vec{u}_i$ is proportional to the velocity of atom i (obtained from diagonalization of the dynamical matrix at the saddle point), and $i = 1$ is assumed to be the jumping atom.

For gold in the glue model at $T = 0$, this analysis yields

$$\Delta K = 0.897.$$

This is in excellent agreement with the experimental estimate obtained by Herzig *et al.* from measurements on ^{195}Au and ^{199}Au, $\Delta K(\text{exp}) = 0.90$ [76]. This value has been obtained by assuming that all diffusion is due to single vacancies, i.e. without consideration of any divacancy contributions.

Chapter 4

Structural studies of Au surfaces

4.1 Noble metal surface reconstructions

Since the advent of the earliest experimental tools in surface physics, the noble metal surfaces have constituted a kind of standard testing ground. Their rather peculiar structural properties have therefore been discussed—if not properly understood—since a long time [77]. For iridium, platinum and gold, in particular, the most notable feature is surface reconstruction, namely a surface rearrangement which produces new strange surface periodicities. For example, the (110) surfaces all exhibit a so-called (1×2) reconstruction, meaning that the surface periodicity is twice as long as expected along the surface direction $\langle 001 \rangle$, while it remains regular along the orthogonal $\langle \bar{1}10 \rangle$ direction. Also the (100) surfaces of Ir, Pt and Au reconstruct, although not exactly with the same periodicities. For Au, the reconstruction is often designated as (20×5). Finally, Au seems to stand out as a kind of "reconstruction champion" in that also the (111) surface reconstructs (the so-called $(23 \times \sqrt{3})$ reconstruction).

The situation prior to 1981 is reviewed very nicely by Van Hove *et al.* [77], who summarize various possible explanations for some of these reconstructions. More recently, with newer surface techniques—such as

STM, ion scattering, He-scattering, etc.—more information has become available, particularly for Au.

A common factor of all these reconstructions seems to be the formation of close-packed (111)-type facets or overlayers, as was guessed pretty early in some cases [78,79,80]. The electronic motivation for this tendency is a subject of current theoretical research, and still open to discussion [81,82]. At the *ab initio* microscopic level, with present-day possibilities, the task is certainly a difficult one, due to the great complexity of the electronic problem. First-principle approaches (of the LDA type) are beginning to appear [83], but it will be presumably some time before a consensus based on them will form. In particular, it cannot be hoped that complicated geometries, such as those of the (100) or (111) surfaces, could be handled without another breakthrough of the level of the recent Car-Parrinello method [2].

Phenomenological schemes, however, could also constitute useful tools to study the nature of metal surface reconstructions. As discussed in the previous Chapters, empirical schemes where the total energy is assumed to depend only on the atomic coordinates, should incorporate many-body forces in order to reproduce correctly many bulk properties of noble metals. It has been shown, in particular, that using a many-body Hamiltonian of the "glue" type (certainly a very restricted class of many-body forces) with a carefully constructed parametrization, a satisfactory modelling of bulk gold properties can be achieved.

Inward surface relaxations (which occur in most metals) and surface reconstructions are clearly many-body phenomena too. In fact, two-body systems always display bulk-like crystalline atomic arrangements at their surfaces, usually with outward vertical relaxations [22,23].

These phenomena can be accounted for by the glue Hamiltonian. The rise of $U(n)$ for decreasing coordinations, such as one finds at a surface, provides a natural driving force for surface relaxation. By contracting the first layer onto the second, the value of n for surface atoms can rise, and the total energy is lowered. This mechanism works, however, only when $U(n)$ is a mild function of n. When $U'(n)$ is too large, surface relaxation may become inadequate to lower surface energy, and

can be replaced by reconstruction: since the coordination of a surface atom is poor, it pays to reconstruct into a denser layer, with better coordination. As shown in this Chapter, this simple mechanism is capable to explain at a considerable detail level the $T = 0$ structural properties of the Au(100), Au(110) and Au(111) reconstructed surfaces [84].

Section 4.2 is devoted to a discussion of the technicalities of the slab molecular dynamics method used for searching the optimal structures. Sections 4.3, 4.4 and 4.5 contain a description of our main findings for Au(100), Au(110) and Au(111) respectively.

4.2 Searching for the optimal structure

Searching for minimum energy configurations in systems with a large number of degrees of freedom and non-trivial forces may be a difficult task. This is particularly true when the "best" geometries are largely unknown and have low symmetries—perhaps due to the presence of surfaces or defects—so that it is not possible to restrict the search by freezing-in some degrees of freedom. In these cases, the system should be able to find its own way towards the energy minimum, without any "suggestion" or built-in constraint. This is the case when statistical mechanics simulation methods, based on molecular dynamics or Monte Carlo algorithms, are used—except for limitations due to the cell size and to the statistical ensemble.

The minimum energy configuration can be obtained from simulation either by a direct quenching procedure, or by a thermal annealing followed by a slow cooling down to $T = 0$. The former method is faster, but since the danger of trapping in a local energy minimum is high, it must be used with caution. The latter method ("simulated annealing") requires more computer time, but energy barriers can be overcome and the system may be able to "land" in the global energy minimum, provided that is deep enough, even if the initial conditions were very far away from there. This method of course does not guarantee attainment of the absolute minimum. However, it is always possible to improve

one's confidence in a given configuration by trying different annealing schedules, and by starting from different initial conditions.

We have used either of these methods, in a molecular dynamics (MD) framework, to find the optimized structures. The atoms are arranged in a slab geometry, with periodic boundary conditions parallel to the surface, free boundary conditions along the surface normal, and a number of layers in the range 10–20. The area of the slab is kept rigid, however its value is changed at different temperatures to match the bulk thermal expansion, accordingly to the zero-pressure bulk calculation described in 3.1. This ensures that internal layers of the slab are as close to bulk layers as possible.

We use standard molecular dynamics, where the number of particles N is fixed. This poses a problem for the study of reconstructed surfaces, since reconstruction often implies surface density changes. In real systems showing surface phase transitions, extra atoms can be added or removed because reservoirs are present in the form of steps, kinks or other defects [77]. Such defects are not present in our small cell, and the only escape is to perform simulations on the same cell using different values for N. The preferred final structure at $T = 0$ will be that with the lowest surface energy σ, which we define as

$$\sigma = \frac{E - N\epsilon_c}{2A} \tag{4.1}$$

where E is the total energy of the slab, ϵ_c the bulk cohesive energy per atom, A the slab area and the factor 2 accounts for two surfaces.

Another problem arises from the small size of the MD cell. Clearly, the MD cell must be a multiple of the reconstruction cell. As a consequence, the search for the optimal reconstruction cell must proceed through attempts with different MD cells, comparison of surface energies always being the ultimate criterion to establish the optimal geometry.

4.3 Au(100) surface reconstruction

4.3.1 Experiments

The (100) surface of gold has been known to reconstruct since a long time. The first, low-resolution LEED measurements [78,79] indicated a (1×5) surface periodicity. Shortly after, the discovery of extra spots in the LEED pattern led to assume (20×5) as the best estimate for the reconstruction cell [78,80].

This large cell was explained as due to the formation of a closely packed triangular overlayer, on top of a square (100) substrate. In this geometry, the five-fold periodicity is due to the fact that six close-packed rows of the triangular layer are stacked above five $\langle 011 \rangle$ close-packed rows of the substrate. This arrangement requires a small (3.8%) shrinkage of the overlayer—when compared with a normal (111) plane in the bulk—to bring the natural row separation $d\sqrt{3}/2$, where d is the bulk first neighbours distance, into the commensurate $5d/6$. If the registry were preserved in the direction $\langle 011 \rangle$ parallel to the rows, the unit cell would be (1×5). The observed (20×5) cell of Au(100) was explained by assuming a small contraction of the overlayer also in this direction, so as to accommodate one extra row over 20 $\langle 01\bar{1} \rangle$ substrate rows.

Later experiments [77,85,86,87,88] refined this substantially correct picture. In particular, LEED [77] and He-scattering [87] studies suggested a much larger unit cell such as $c(26 \times 68)$, as the result of an additional contraction along the five-fold direction $\langle 01\bar{1} \rangle$ (and 26 replacing 20). In their scanning-tunneling-microscope (STM) real-space investigation [88] Binnig, Rohrer, Gerber and Stoll (henceforth BRGS) propose a $\begin{pmatrix} 26 & 0 \\ Z & 48 \end{pmatrix}$ unit cell where $-5 \leq Z \leq 0$, implying an additional $\langle 01\bar{1} \rangle$ contraction but also the possibility of a small rotation (about 0.1°) of the whole overlayer over the substrate. It should be noted that these experiments do not rule out the possibility that the two lattices are actually incommensurate.

From the physical point of view, the most important feature of the Au(100) reconstruction is the close packing achieved by the topmost

layer. This indicates the surface density increase as the driving force behind reconstruction. The energy of the system is lowered by this density increase, overcoming the strain energy cost caused by the misfit between the square substrate and the triangular overlayer.

The scope of the present Section is to explore all details concerning both shape and energetics of the Au(100) surface atomic arrangement as predicted by the glue Hamiltonian at $T = 0$ [33,89].

4.3.2 (1×5) reconstruction

An investigation of the Au(100) surface structure predicted by the glue Hamiltonian has been carried out using molecular dynamics, following the procedure outlined in Sec. 4.2. MD is used as a tool to generate the minimal energy configuration, through simulated annealing, of slabs with in-plane periodic boundary conditions and initially $5 \times 5 = 25$ atoms per (100) plane. It is found that a number of layers $L = 14$ is sufficient to decouple the two surfaces. A typical annealing cycle consists of warming the slab up to about $T_m/2$ and, after equilibration, gradually cooling back to $T = 0$. The total length of the cycle is of the order of 10000 MD steps (1 step $\simeq 7 \times 10^{-15}$ s).

This procedure has been first applied to the clean, unreconstructed (100) faces. Figure 4.1a shows the appearance of the first atomic layer after annealing. One can note that the surface atoms have shrunken together, leading to formation of close-packed stripes (five atomic rows each) separated by a gap [1]. This gap in turn can be seen as leading to the formation of two monatomic steps, here still very near to one another. The second layer has remained a basically perfect (100) plane. This is a clear indication that our (100) surface wants to reconstruct into a denser layer, even within the constraint of the small 5×5 cell.

To pursue further this idea, we have made a series of runs where a

[1] By a careful quench of a perfect crystal, *not* preceded by heating and thermal equilibration, an unstable relaxed but perfect (100) surface has been indeed produced. Its surface energy is higher than that of the configuration with the gaps (128.5 vs. 109.6 meV/Å^2).

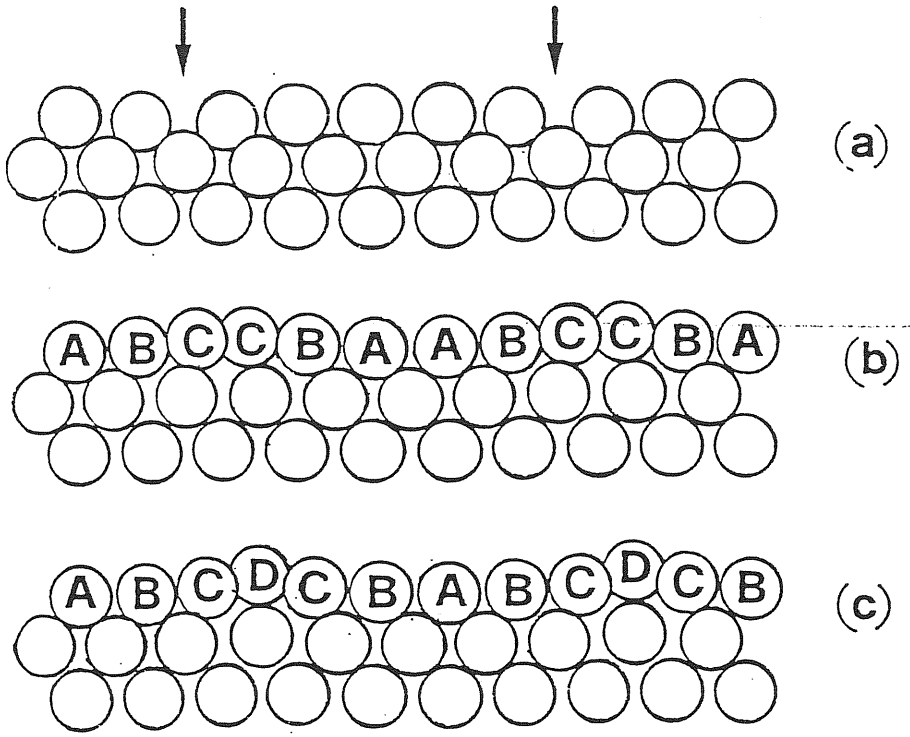

Figure 4.1:
Side views of minimum energy configurations of (100) slabs after thermal equilibration and subsequent annealing. Two molecular dynamics cells are shown for clarity.

(a) The starting configuration was a perfect (100) slab. The atoms have shrunken in 5-rows wide stripes, leaving a gap (indicated by the arrow) in between. The surface energy is 109.6 meV/Å^2.

(b) 5 additional adatoms present in the starting configuration. They are absorbed, giving rise to a 20% denser quasi-triangular reconstructed first layer with a $ABCCBA$ stacking. The surface energy is 102.3 meV/Å^2.

(c) Same as (b), but the registry is different and the stacking is $ABCDCB$. The surface energy is 102.6 meV/Å^2.

All atomic positions shown to scale (not schematic), but atom radii are arbitrary. Vertical (z) direction $\langle 100 \rangle$, horizontal (y) direction $\langle 01\bar{1} \rangle$.

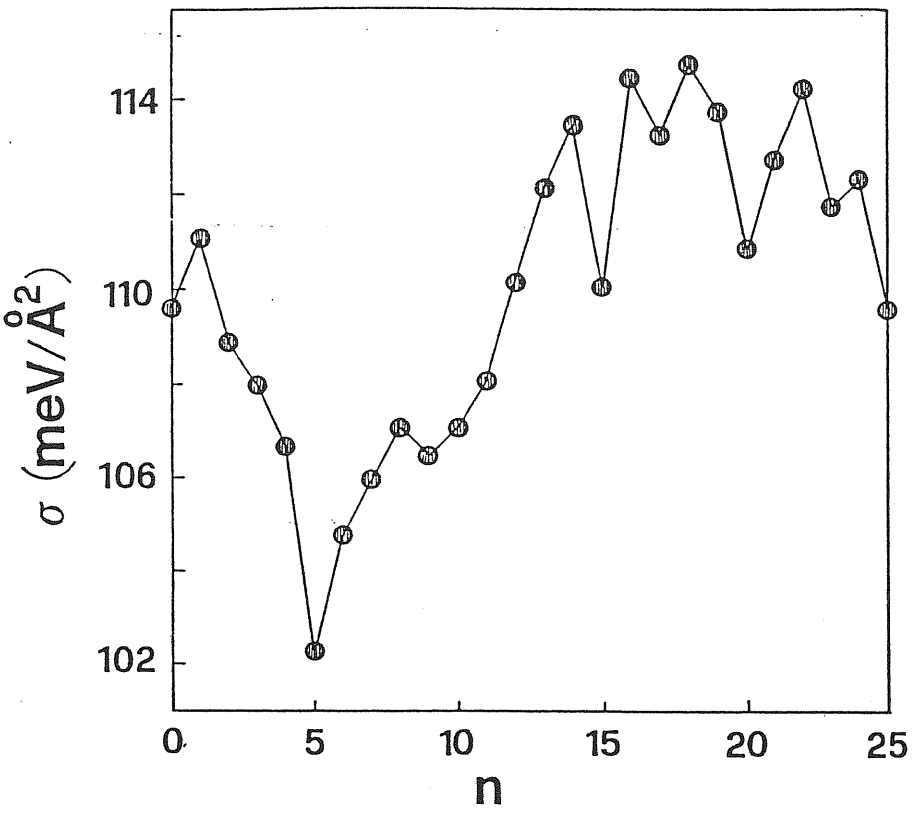

Figure 4.2:
Surface energy of the final configurations as a function of the number of adatoms present at the start in a 5 × 5 (100) slab. The minimum at $n = 5$ corresponds to the configuration in Fig. 4.1b.

number n of extra adatoms is added on top of the first layer. n is varied throughout the range from $n = 1$ to $n = 25$. For n small, the extra atoms are absorbed into the first layer giving rise, after annealing, to a denser packing. At the same time, we find a decrease of the surface energy σ (defined by Eq. (4.1)). A minimum of σ as a function of n is obtained for $n = 5$, as shown by Fig. 4.2.

The corresponding first-layer arrangement of Fig. 4.1b is a good candidate for explaining the Au(100) reconstruction. The second and deeper layers retain a strained (100) character, in agreement with the

experimental findings [85]. The amplitudes of the corrugation predicted for the first four layers are $\xi_1 = 0.47\,\text{Å}$, $\xi_2 = 0.21\,\text{Å}$, $\xi_3 = 0.13\,\text{Å}$, and $\xi_4 = 0.08\,\text{Å}$. The relaxations of the distances between average layer positions are $\Delta d_{12} = +3.6\%$, $\Delta d_{23} = +2.2\%$, and $\Delta d_{34} = -0.2\%$. The increase of d_{12} and d_{23} is due to excessive coordination in the second layer, caused by the first-layer reconstruction. The stacking of the rows is $ABCCBA$, as on Fig. 4.1b.

We have also found a local energy minimum at another stacking $ABCDCB$, shown in Fig. 4.1c. In this arrangement the surface energy is slightly higher and the corrugation is larger. The main physical difference between the two stackings is that in the latter the strain is concentrated on the atoms of row D, which is severely raised over the A row ($\xi_1 = 0.74\,\text{Å}$), whereas in the former $ABCCBA$ stacking the strain is shared by the two C rows, resulting in a smaller outwards corrugation over the A rows. In both cases the strain is not uniformly distributed; the surface density is higher in a hilltop row, and lower in a valley row, where the atoms are not far from their ideal hollow-site positions over the square substrate.

Of course the role played by the cell size in these calculations is not a minor one. The $n = 5$ "best" configuration has a (1×5) reconstructed structure which fits very well in our 5×5 cell. On the other hand, the use of different cells may reveal the existence of reconstructed surfaces with a still lower surface energy. Following this idea, calculations of the same kind have been performed, with cells suited to the following reconstruction patterns: (1×7), (1×12), (1×8), (1×3), respectively of the kind 8-onto-7, 7-onto-6, 5-onto-4, 4-onto-3 (in increasing order of surface density). Some have periodicities which are twice the number of substrate rows because the unit cells must contain an even number of rows in the triangular overlayer. All these surfaces reconstruct into a denser overlayer, and the surface energies are reported in Table 4.1. Since they are all higher than the (1×5) surface energy, (1×5) is the preferred pattern.

Structure	σ (meV/Å^2)
non-reconstructed, ideal	143.1
non-reconstructed, relaxed	128.5
(1×7) relaxed	103.7
(1×12) relaxed	103.2
(1×5) relaxed	102.3
(1×8) relaxed	103.3
(1×3) relaxed	108.6

Table 4.1:
Surface energies for several (100) geometries. (1×7), (1×5) and (1×3) have 8 rows over 7, 6 over 5, 4 over 3 respectively. (1×12) and (1×8) have 7 rows over 6 and 5 rows over 4. (1×5) has the lowest surface energy.

4.3.3 $(M \times 5)$ reconstruction

So far we have considered only the reconstruction along the five-fold $\langle 01\bar{1} \rangle$ direction, which gives rise to the basic (1×5) pattern. In this geometry, the quasi-triangular overlayer is contracted on the average by 3.8% along $\langle 01\bar{1} \rangle$ (henceforth direction y), while it is in registry with the underlying lattice in the $\langle 011 \rangle$ direction (henceforth direction x). On the other hand, as discussed in Subsec. 4.3.1, the unit cell has been regarded as a (20×5) for a long time, indicating a 4.8% average contraction along x, and larger cells are suggested by later experiments [77,88].

The 5×5 cell size used in the calculation described in the previous Subsection obviously prevents the possibility to study reconstructions of long periodicities. We have therefore lifted this restriction by going to larger $M \times 5$ unit cells. Assuming as a starting point the presence of a 6-onto-5 reconstruction in the y direction, we searched for the optimal contraction in the x direction by studying the surface energies of reconstructed $(M \times 5)$ 12-layers slabs.

In the starting configuration, the topmost layer is a perfect triangular lattice contracted by 3.8% in the y direction to accommodate 6 rows

onto 5 in the substrate and by a factor $1/(M+1)$ in the x direction to accommodate $M+1$ $\langle 01\bar{1}\rangle$ (staggered) rows onto M. All the initial interlayer distances are set equal to $a_0/2$. This configuration is already reconstructed and very close to the (1×5) geometry, found to be optimal among all small size cells investigated in the previous Subsection. Therefore, only small relaxations (and not extensive atom rearrangements) are expected to be required to minimize the energy. For this reason, a relatively fast (~ 3000 steps) molecular dynamics quench procedure has been employed to search the minimum energy state, where kinetic energy is gradually extracted from the system until a local energy minimum is attained.

Although computationally heavier (due to the large N and to the number of slabs to study) and, as it turns out, quite instructive, the present study is in a way simply a refinement of the basic quasi-triangular geometry already established. In particular, we know from the previous Section that there are two kinds of stable (1×5) arrangements ($ABCCBA$ and $ABCDCB$), differing mainly in the registry with the substrate along the y direction. In the present study of $(M \times 5)$ cells we explore either possibility, by choosing the appropriate registry in the starting configuration. We then calculate and compare the surface energies σ of the final, fully relaxed slabs. We have verified, in each case described here, that the two surfaces of the slabs behave identically, structurally and energetically, to an accuracy of better than six significant figures.

4.3.4 Energetic and structural analysis

The surface energy of relaxed $(M \times 5)$-reconstructed slabs as a function of M is shown in Fig. 4.3. Surface energies are expressed as differences $\Delta\sigma$ from the $ABCCBA$ (1×5)-reconstructed surface, $\sigma_0 = 102.3\,\mathrm{meV/\AA^2}$. Four curves are represented, two corresponding to the $ABCCBA$ registry and two to the $ABCDCB$ registry. For each registry, the even and odd M cases are distinguished. The latter choice in fact gives systematically a slightly higher surface energy. The two curves related to the

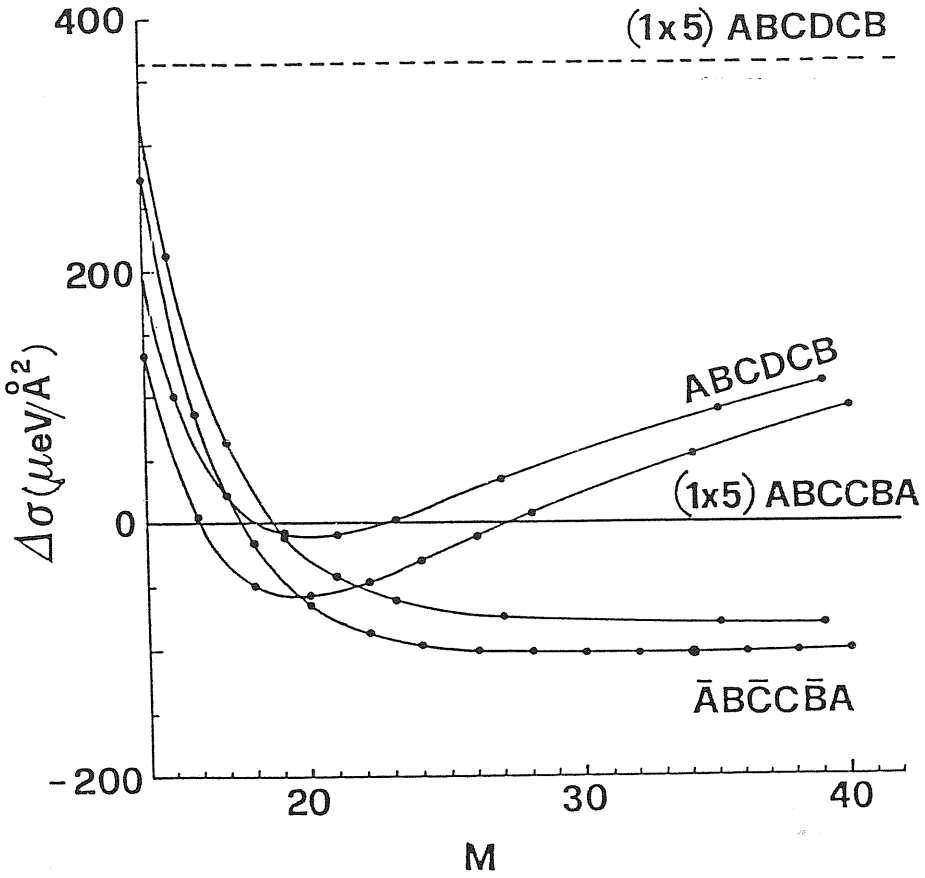

Figure 4.3:

Differences of surface energies of $(M \times 5)$-reconstructed slabs, with respect to a (1×5)-reconstructed $ABCCBA$ slab, as a function of M. The two basic y registries ($ABCCBA$ and $ABCDCB$) show different behaviours. For each registry, the odd M case is slightly disfavoured due to the presence of excited solitons S^* (see Subsec. 4.3.6). The optimal surface is $ABCCBA$, $M = 34$.

$ABCCBA$ registry should converge to 0 in the limit $M \to \infty$, where the (1×5) registry is recovered. The $ABCDCB$ registry is favoured for $M < 19$, while the $ABCCBA$ has a lower surface energy for $M \geq 19$. In the $ABCCBA$ case, all $M \geq 18$ improve over the (1×5) surface energy. The curve becomes very flat for $M > 26$, with differences of the order of $1\,\mu\text{eV/Å}^2$ between adjacent points [2]. The absolute minimum value occurs at $M = 34$, then the curve gently begins to rise towards the asymptotic zero value. The surface energy corresponding to this minimum is about 0.1% less than the $ABCCBA$ (1×5) surface energy. In the $ABCDCB$ registry there is a marked minimum at $M = 20$, then the curve rises towards the $ABCDCB$ (1×5) surface energy which corresponds to $366\,\mu\text{eV/Å}^2$. Furthermore, we note that after annealing some of the small distortions that take place break the exact mirror plane symmetry of $ABCCBA$. The relaxed surfaces have instead a lower symmetry of the type $\bar{A}B\bar{C}C\bar{B}A$, where A and $\bar{A}$, B and $\bar{B}$, C and $\bar{C}$ are different as discussed below.

The above analysis leads to the following interesting points:

1. the $\bar{A}B\bar{C}C\bar{B}A$ arrangement provides the overall surface energy minimum, and leads to larger unit cells than $ABCDCB$.

2. the best length M of the $(M \times 5)$ unit cell is $M = 34$, but the minimum of the surface energy is so flat as to make this precise value almost meaningless. Any value of M between 28 and 38 is about equally good.

3. the odd M cells cost more energy to realize than the even M cells. This has to do with the presence of a defect, as will be discussed in detail in 4.3.6. The defect-free situation is that of even M, which therefore must be taken as representative of the perfect surface.

[2] Of course, the *absolute* level of confidence we have on the energetic accuracy of our glue scheme is far from the level of the μeV, or even the meV, per atom. The accuracy of *relative* energy differences, however, can be very different, and should basically be as good as the physical description behind our Hamiltonian. In this sense, it is meaningful to seek the optimal configuration, even among possibilities which are energetically very close.

We can now proceed to examine the structural details of our optimal (100) surface arrangement, i.e. $\bar{A}B\bar{C}C\bar{B}A$, (34×5), as resulting from our molecular dynamics minimization. In Fig. 4.4 we show three views of this surface. It is apparent that the strain in the x direction is concentrated in highly corrugated regions which have a one-dimensional "soliton" appearance [90]. These solitons form a two-dimensional lattice, six of them per each rectangular unit cell, of size 34×5. Except for a small distortion, this arrangement corresponds to a centered rectangular lattice with two solitons per cell, of size $34 \times \frac{5}{3}$. Note the alternate stacking of solitons, due to the geometrical interplay of superposed triangular and square lattices (see Fig. 4.4b), more than to an effect of repulsion between solitons. Yet, this repulsion exists. In the dilute limit, i.e. M very large, the soliton-related surface energy change $\Delta\sigma$ can be expanded in powers of their density, $\frac{6}{5}M^{-1}$:

$$(a_0^2/2)\Delta\sigma = \mu(6/5)M^{-1} + \frac{1}{2}\nu(6/5)^2M^{-2} + \ldots \qquad (4.2)$$

We have found that Eq. (4.2) provides a good fit for $M = 18, 20, \ldots, 40$ and ∞, as shown in Fig. 4.5. The fit yields $\mu = -48\,\text{meV}$ (the soliton "chemical potential") and $\nu = 1370\,\text{meV}$ (the effective soliton "pairwise repulsion").

Next, we discuss the corrugation pattern of our (34×5) surface, shown on Fig. 4.6. We note first of all that, far from the soliton regions, the B, $\bar{B}$ rows are basically at the ideal first-second layer distance (2.035 Å), while the A, $\bar{A}$ rows are $\sim 1\%$ contracted and the C, $\bar{C}$ rows are $\sim 4\%$ expanded. The solitons show up rather sharply at $x = +0.7$ Å (with our choice of origin, $x = 0.7$ Å corresponds to a bulk $\langle 01\bar{1}\rangle$ row), as can be seen from the sharp cusps for rows $\bar{A}$, $\bar{B}$ and $\bar{C}$. The soliton width can be estimated to be about 10 Å. The remaining rows A, B and C run "between" these solitons and show a much weaker corrugation. In fact the other three solitons in our cell appear symmetrically on these rows A, B and C, and their centers fall at $x = -48.2$ Å, very near to the cell boundary ($x = \pm 48.9$ Å). A wide smooth area extends between the two triplets of solitons. Right in the middle of it, at $x = -23.7$ Å and $x = +25.2$ Å, there is a coincidence of A with $\bar{A}$, B with $\bar{B}$, and C

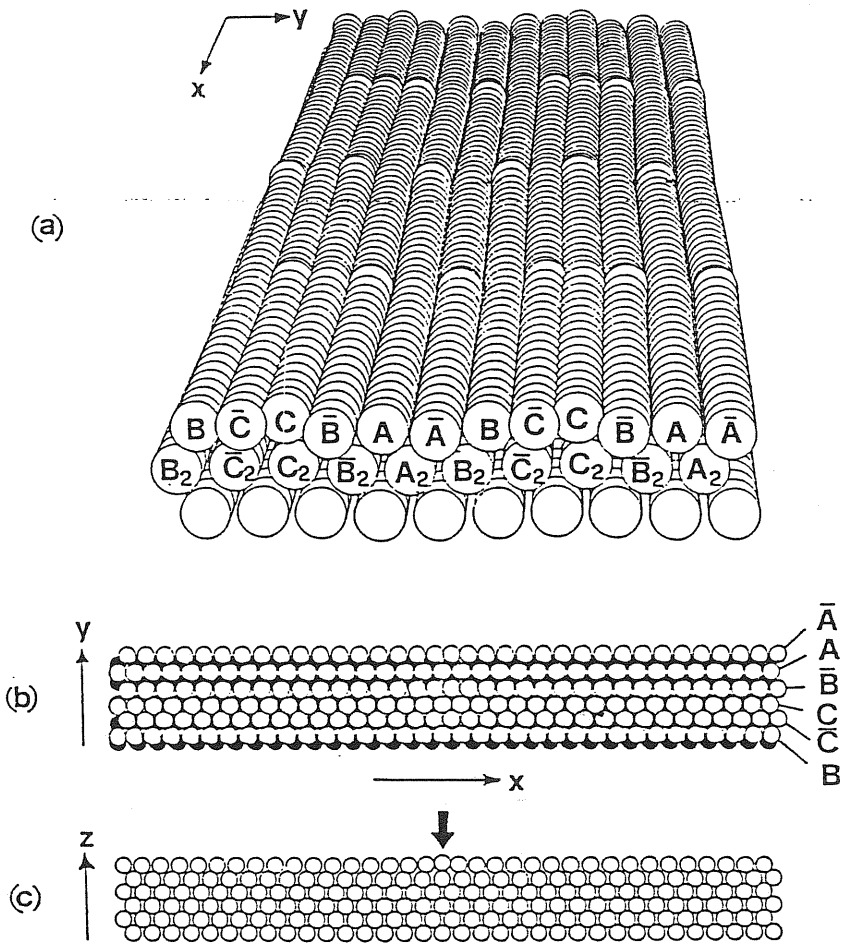

Figure 4.4:

The optimal $ABCCBA$ (34 × 5) surface.

(a) Perspective view showing the soliton lattice. A 2 × 2 array of cells is shown.

(b) Top view of the first (white atoms) and the second layer (black atoms).

(c) Side view of the first six layers. The first layer (a $\bar{B}$ row is shown) has a soliton in the middle.

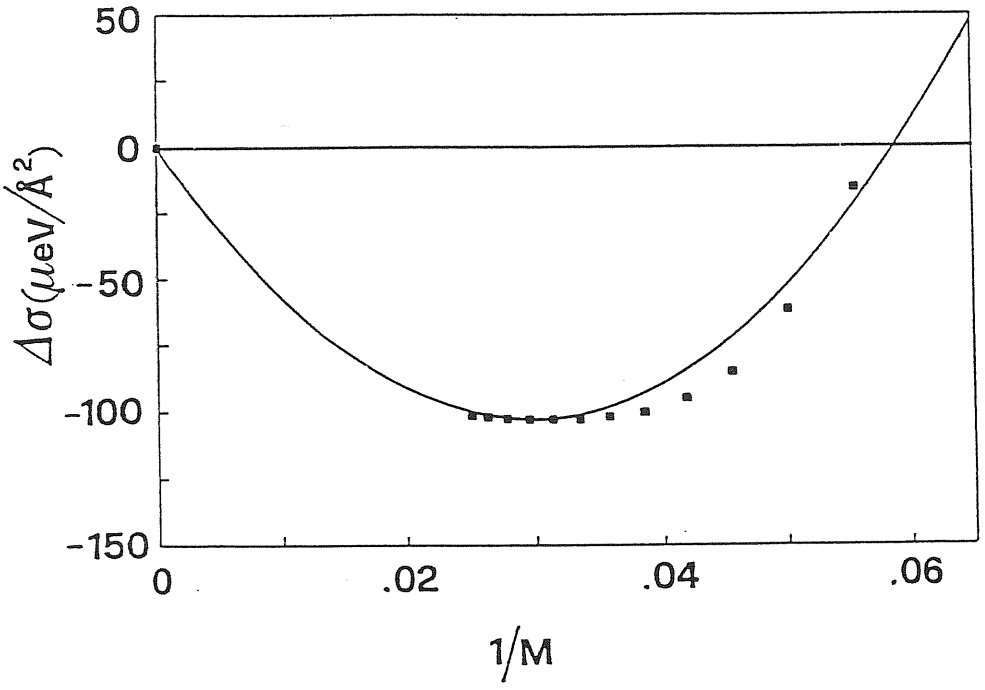

Figure 4.5:
Second-order expansion of the surface energy difference $\Delta\sigma$ with respect to $ABCCBA$ (1×5) in powers of $1/M$. The dots are the values obtained from the molecular dynamics minimization.

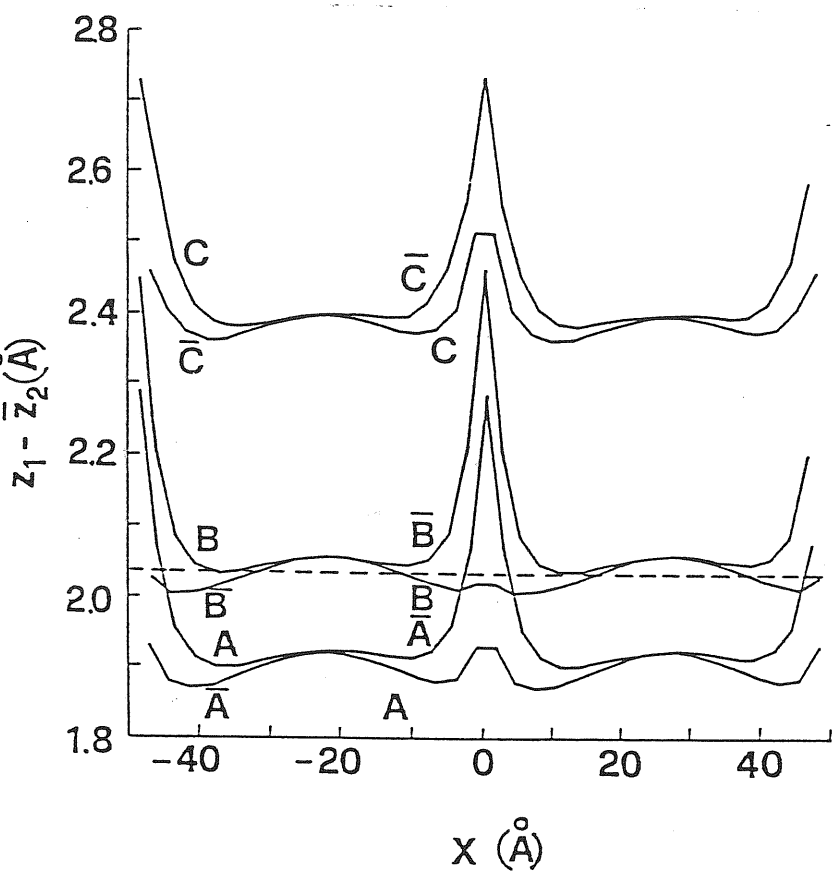

Figure 4.6:
Distance of first layer atoms from the second-layer average plane as a function of x for each row. The dashed line at $a_0/2 = 2.035$ Å corresponds to the bulk interplanar spacing.

with $\bar{C}$, so that locally the surface is exactly a (1×5) $ABCCBA$. The relatively large extension of this area may account for the intense (1×5) features of diffraction patterns: the surface only differs from a (1×5) due to the solitons, which are rather localized.

We can argue from Fig. 4.6 also about the y-corrugation (along $\langle 01\bar{1} \rangle$). The corrugation pattern in the smooth area (i.e. for $x \approx \pm 25$ Å) is single-maximum–single-minimum, with a total excursion of 0.48 Å in the middle of the area. On top of the solitons, on the other hand, the $ABCCBA$ pattern is double-maximum–double-minimum, with a total swing of 0.80 Å. This pattern occurs only on 6 rows out of 35, i.e. when the $\bar{A}$ (A) atoms are higher than the B ($\bar{B}$) atoms. It is noteworthy that the two maxima have different heights (2.29 Å in $\bar{A}$, 2.74 Å in $\bar{C}$).

Along with these morphological features, we can identify corresponding oscillations of the local atomic coordination n_i (defined by Eq. (1.7)), and of the associated excess energy per atom relative to the bulk, $\epsilon_i - \epsilon_c$ (defined by Eq. (1.12)), both of which are shown on Fig. 4.7. The coordination along a row increases when approaching a soliton, but falls into a deep minimum in correspondence with the top atom at the center of the soliton. At the same time the energy has a sharp maximum. This situation is completely changed when the soliton is in the two adjacent rows (for $\bar{A}$, $\bar{B}$, $\bar{C}$ in Fig. 4.7 this happens at $x = -48.2$ Å). In this case, the atoms have a true maximum in the coordination and a minimum in the energy when going through the "valley" between the solitons. Therefore, the alternate soliton stacking plays a crucial role in keeping down the soliton formation energy.

Also evident from Fig. 4.7b is the high average energy of the $\bar{C}$ row. This is due to a concentration of the strain in the y direction over the C and $\bar{C}$ hill rows. In fact, it can be visually seen in Fig. 4.4a and 4.4b that the A and $\bar{A}$ rows have a slightly wider spacing than the C and $\bar{C}$ rows. On the C and $\bar{C}$ rows we observed large bond length contractions (up to 16% for some atom pairs, with $\sim 5\%$ as a typical average value) and the associated two-body repulsion raises the energy of the row.

Finally, in Fig. 4.8 we show the behaviour of the phase φ_k of the

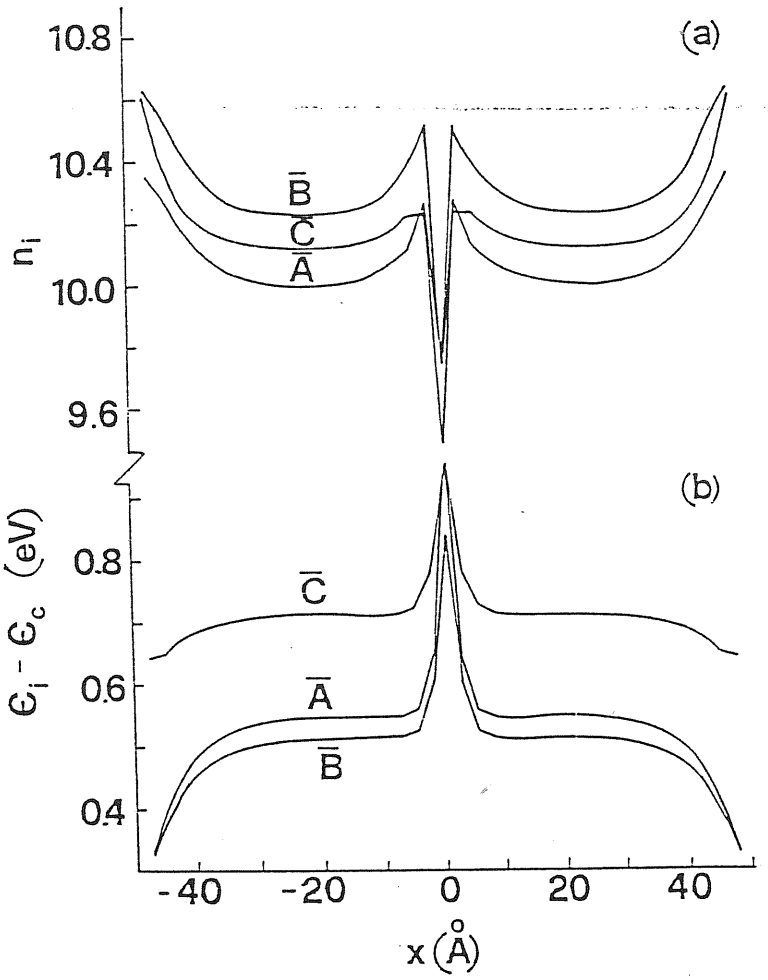

Figure 4.7:

(a) Coordination n_i as a function of x for atoms of the $\bar{A}$, $\bar{B}$, $\bar{C}$ rows.

(b) Excess energy per atom (relative to the bulk) $\epsilon_i - \epsilon_c$ as a function of x for the $\bar{A}$, $\bar{B}$, $\bar{C}$ rows.

The soliton centers are at $x = +0.7$ Å for $\bar{A}$, $\bar{B}$, $\bar{C}$, and at $x = -48.2$ Å for the adjacent rows A, B, C.

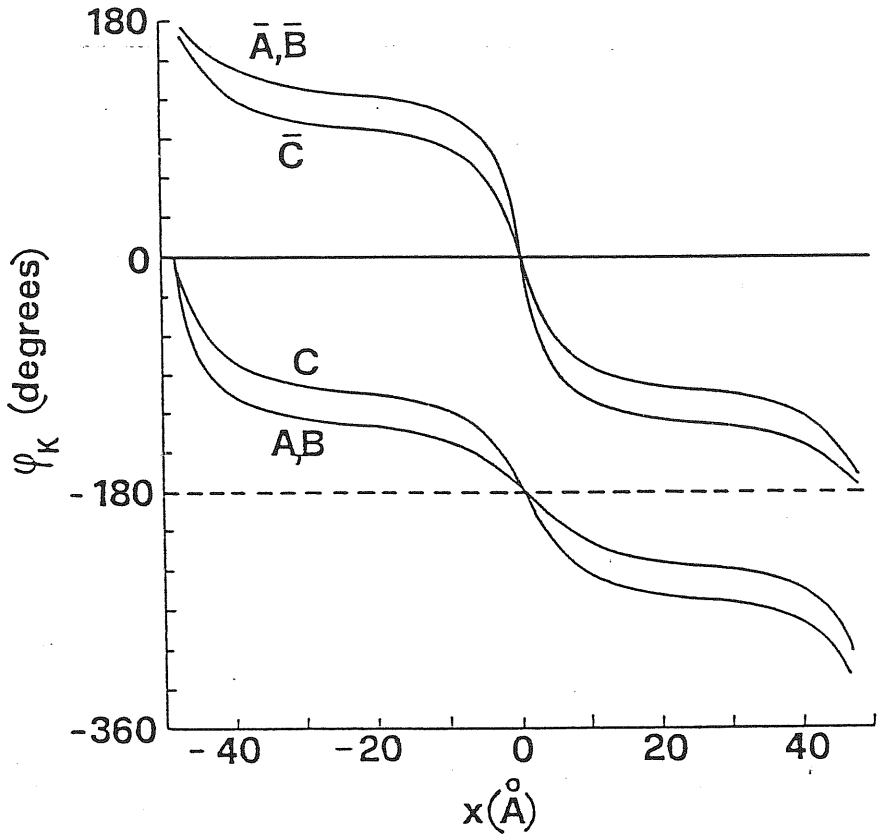

Figure 4.8:
Soliton phase (defined by Eq. (4.3)) as a function of x for each row. The total 360° phase shift in a cell is achieved in two steps. The large step corresponds to a soliton in the given row and the small step to solitons in the adjacent rows.

solitons, defined for a given row as

$$\varphi_k = \frac{2\pi}{d}(x_k - kd + b), \tag{4.3}$$

where k is an index running from 1 to 35 (number of atoms in a top row for a bulk cell of 34), x_k is the x coordinate of atom k, d is $a_0/\sqrt{2}$ and b is a constant (equal for all the rows). We have referred the phase angle to an ideal perfect square lattice rather than to the actual substrate layer, which is slightly distorted as discussed in 4.3.5. It is apparent that the 360° total phase shift within a cell is achieved by a row through two distinct steps: a larger phase shift across the soliton region ($\sim 250°$ for A, $\bar{A}$, B, $\bar{B}$, $\sim 200°$ for C, $\bar{C}$), and a smaller phase shifts when the row runs "between" two solitons ($\sim 110°$ for A, $\bar{A}$, B, $\bar{B}$, $\sim 160°$ for C, $\bar{C}$). As a result, the phase difference between any pair of rows changes its sign across the soliton region, so that the (1×5)-like phase on the left of the soliton becomes mirrored in a specular phase on the right.

4.3.5 Multilayer relaxations

The previous Subsection describes the first layer alone rather exhaustively. This should not be taken to imply that the second and deeper layers, which have not reconstructed, have retained their perfect square lattice atomic positions. On the contrary, the second layer is severely strained and warped. Moreover, some "multilayer" relaxation propagates down to the third and fourth layers.

The second layer undergoes a considerable amount of in-plane shear distortion. The maximum shear occurs in correspondence with the middle of the smooth area, and amounts to 0.37 Å between the two adjacent $\langle 011 \rangle$ rows labeled C_2, $\bar{C}_2$ in Fig. 4.4a. The vertical corrugation is also very noticeable, "following" generally the first-layer corrugation. The detailed pattern is that of Fig. 4.9. Cusps are still sharp at the soliton positions, although their height is lower. The y-corrugation ranges from 0.21 Å in the center of the smooth area, to 0.29 Å in correspondence with the solitons.

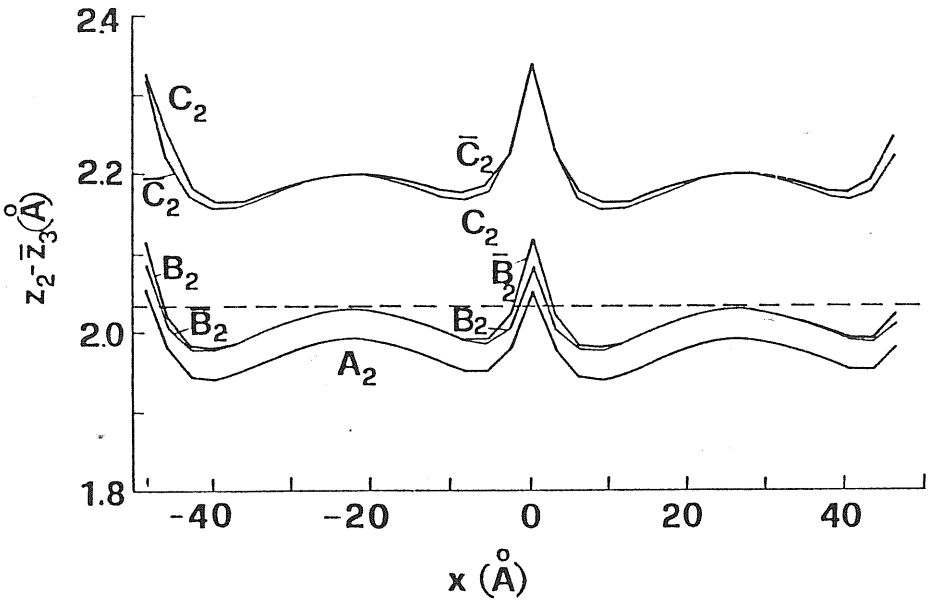

Figure 4.9:

Same as Fig. 4.6, for the second layer. Distances are from the third-layer average plane. The dashed line corresponds to the bulk interplanar spacing. The labeling of second-layer rows is shown in Fig. 4.4a.

Proceeding down to the third and deeper layers we observe that, while the in-plane shear decays quite fast (0.07 Å in the third layer, 0.02 Å in the fourth, and negligible afterwards), the same is not true for the vertical corrugation. In the third layer, the y-corrugation is 0.13 Å near the middle of the smooth area, and 0.19 Å at the soliton positions. The corresponding values for the fourth layer are 0.08 Å and 0.10 Å.

Finally, the average interplanar distance is also modified appreciably. By averaging over all atoms of each layer, we obtain $\Delta d_{12} = (d_{12} - d_{12}^0)/d_{12}^0 = +5.0\%$, $\Delta d_{23} = +2.1\%$, $\Delta d_{34} = -0.3\%$. Δd_{45} and successive are negligible. These average relaxations are close to those obtained with the smaller (1×5) cell. The outwards relaxation of the first layer may appear unusual for a metal. However, it is an unescapable consequence of our Hamiltonian, where coordination plays a key role. The first-layer reconstruction, while not succeeding in raising the first layer coordination to 12, has the effect of increasing that of the second layer *above* 12. Outwards relaxation of the first layer relative to the second, and to some extent also of the second relative to the third, is then called for as the only means to keep the second-layer coordination from getting too high. No experimental data have been reported for such relaxations on Au(100). It is interesting, however, to note that data do exist for the closely related (1×5) Ir(100) surface. The model proposed by Moritz [91] based on dynamical LEED is quite similar to our (1×5) cell, and is reported to have a large first layer outwards relaxation $\Delta d_{12} \approx +15\%$ (average value), which encouragingly goes precisely in that direction.

4.3.6 Odd versus even M: excitations in the soliton system

Here we digress briefly on the implications of the even-odd M oscillations shown by our results of Fig. 4.3. It is quite simple to explain how these oscillations arise in our calculation. We start by recalling that we have $M + 1$ atoms per row to be placed above M substrate atoms along x. As it turns out, for even M one of the $M + 1$ atoms of each row wants

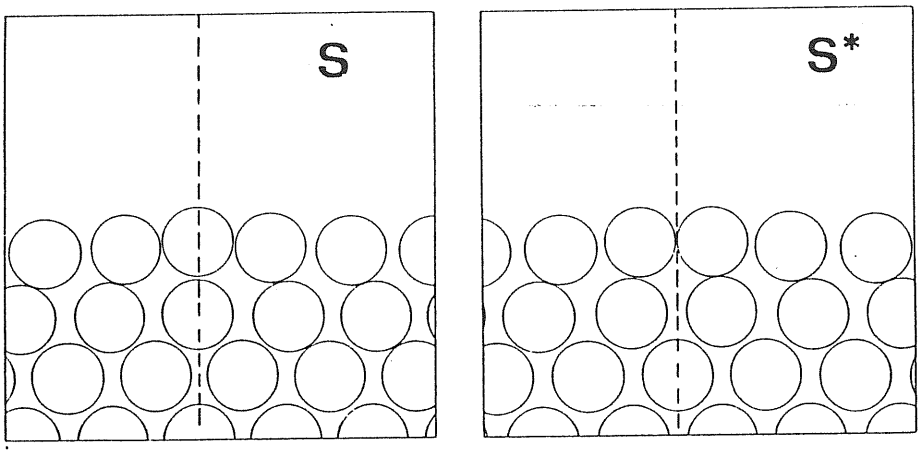

Figure 4.10:
The sharp soliton S and the broader "excited" soliton S^* for the $\bar{B}$ rows. The "excitation energy" from S to S^* is about 11 meV.

to sit exactly at the same x, i.e., approximately on top, of one of the M substrate atoms. That is the center of the sharp soliton (denoted by S) for that row. When M is odd, it is not possible to realize a sharp soliton on all rows. The optimal solution is realized by retaining a sharp soliton S for every other row (e.g. A, B, C) and replacing the sharp soliton on the remaining rows ($\bar{A}$, $\bar{B}$, $\bar{C}$) with a broader "excited" soliton S^* energetically less favourable than S [3]. As shown by Fig. 4.10, in S^* the soliton center falls *between* two atoms rather than on top of an atom as in S. In the odd M case the stacking is thus $\bar{A}^*B\bar{C}^*C\bar{B}^*A$ (where $\bar{A}^*$ means an $\bar{A}$ row with an S^* soliton, etc.). The mirror plane reflection transforming $\bar{A}B\bar{C}C\bar{B}A$ into $A\bar{B}C\bar{C}B\bar{A}$ for even M, has disappeared

[3] Actually, for the odd M case, other less symmetric configurations can also be generated with comparable or even slightly lower energy than that just described. In such configurations, the number of S^* solitons per cell is decreased, at the cost of some extra strain on the S solitons. We will not go into further detail about that here, since the concept of excited soliton S^* is already well introduced by the symmetric arrangement.

for odd M, where S and S^* are different.

The energetic cost ε required for "exciting" a soliton S into S^* is straightforwardly extracted from the even-odd oscillation $\delta\sigma$ visible in Fig. 4.3, by using $\delta\sigma = 3\varepsilon/A$. Here $3/A$ is the surface density of S^* excited solitons in a cell of area A. Our best estimate for ε is 11 meV. Such a low energetic cost is interesting, and suggests that already at room temperature the probability to find each given soliton in the (broader) excited state is far from negligible.

4.3.7 Comparison with STM results

The surface energy minimization described in the previous sections has provided a very detailed model for the Au(100) reconstructed surface. The optimized periodicity is (34×5), to be compared with the suggested experimental value of (26×48) [88], which (in spite of numbers looking different) is very close to (26×5). This can be regarded as a pretty good agreement, particularly since: (a) the minimum in σ versus M is extremely flat, as already mentioned in Subsec. 4.3.4; (b) no provision is made for an additional contraction in the y direction or a small overall rotation (both leading to much larger unit cells) and for finite temperature effects.

The detailed discussion provided by BRGS of the Au(100) surface morphology obtained by STM allows some further comparison with our calculated structure. Their STM micrograph, shown in Fig. 4.11, exhibits an alternation of "smooth ribbons" with "rough ribbons". We can identify the rough ribbons as the stripes joining solitons along $\langle 01\bar{1} \rangle$, and the smooth ribbons as the wide flat regions in between. The rough ribbons seem narrower in our calculation than in the STM picture. However, it is possible that this could be due to temperature smearing, rather than a genuine disagreement. We note that a non-sharp soliton can only really be expected of a hard-sphere model, where relaxation is totally absent. Soliton sharpening is an inevitable effect of relaxation which is generally expected, quite independently of the present specific force

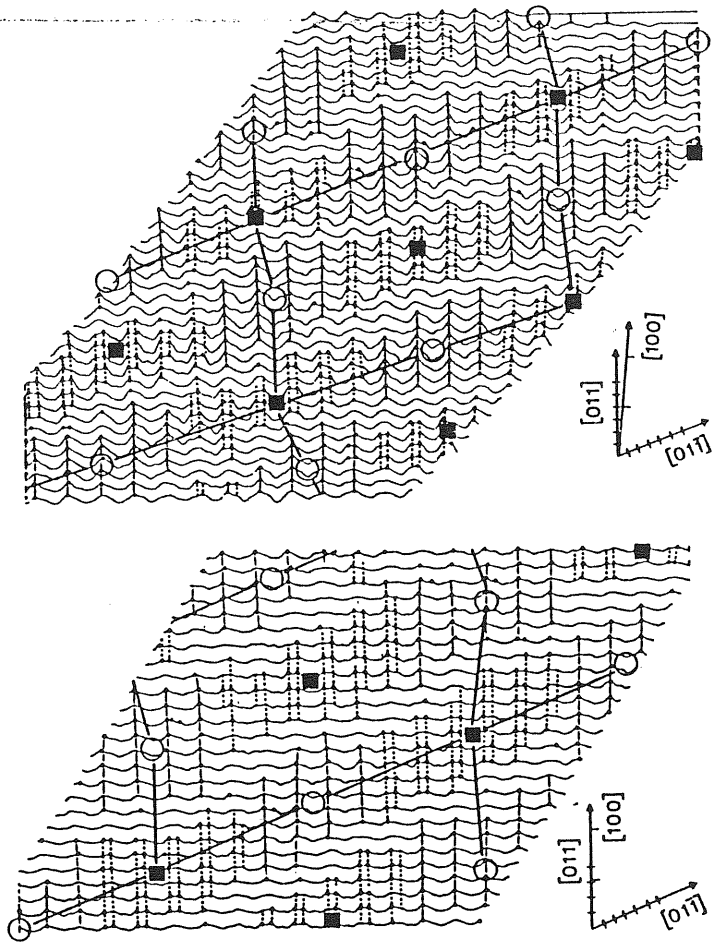

Figure 4.11:

STM micrographs of Au(100), taken from ref. [88]. They show the alternating sequences of "rough ribbons", with a double-maximum–double minimum corrugation pattern, and "smooth ribbons", with a single-maximum–single-minimum pattern. These ribbons are oriented along $\langle 01\bar{1} \rangle$. Divisions on the axes correspond to 5 Å. The solid lines show the unit cell, $\approx (26 \times 48)$. $\langle 011 \rangle$ is direction x and $\langle 01\bar{1} \rangle$ direction y in Fig. 4.4.

model [4].

Another feature which is present in a hard-sphere model but is wiped out by relaxation in our model is the "triple-maximum" corrugation along y [88]. In our (34×5) surface the y corrugation can be described as follows. In the x region between the solitons (the smooth ribbon of BRGS) we find a "single-maximum–single-minimum" corrugation of magnitude ~ 0.5 Å (see Fig. 4.6). This corrugation coincides numerically with the value suggested by the He-scattering analysis of Rieder *et al.* [87]. On the other hand, on top of the solitons the y corrugation is of the "double-maximum–double-minimum" type (due to the alternating stacking of solitons) with total magnitude ~ 0.8 Å. Once again, it seems to us that such a theoretical corrugation pattern is compatible with the STM results. They indeed present an alternation of "single-maximum–single-minimum" with "double-maximum–double-minimum" stripes, with little direct evidence for a triple maximum.

In conclusion, it has been shown how an extremely detailed picture of the reconstructed Au(100) surface can be obtained by starting from the same glue Hamiltonian which reproduces the bulk properties. The resulting energetics and surface atomic arrangement appear realistic, and compare favourably with existing experimental evidence.

4.4 Au(110) surface reconstruction

4.4.1 Experiments

The (110) surfaces of Ir, Pt and Au exhibit a (1×2) reconstruction, meaning that the surface unit cell length is the same as in a truncated bulk along the $\langle \bar{1}10 \rangle$ direction, while it is twice as long along $\langle 001 \rangle$. Among gold surfaces, Au(110) is probably the most studied. Experimental data for Au(110) have been obtained with a number of different

[4]However, the amount of sharpening does depend on details. For example, if the final first-second layer expansion of Au(100) were found to be as large as suggested for Ir(100) [91], i.e. $\sim$ 15% rather than 5%, then also the soliton width would probably be larger.

techniques, namely LEED [78,92,93,95,96,105], He-diffraction [94,98], low [97,106], medium [107] and high [99,103,104] energy ion scattering, STM [100], X-ray diffraction [101] and transmission electron microscopy [102].

While various models have been proposed in the past to explain the (1×2) pattern (see, e.g., Ref. [98]), general consensus has now gathered around the "missing row" model. In this model, every other close-packed $\langle \bar{1}10 \rangle$ row is absent in the topmost layer. The resulting surface structure displays a zigzag profile, with tiny (3-rows wide) (111) facets. A point debated in literature concerns the relaxation of the top row. By now, most authors believe that the top (ridge) row is contracted towards the second layer [92,97,98,105,106,107], although expansion had been argued by some [101,102].

Other periodicities such as (1×3) and (1×4) are also occasionally observed in experiments [92,100]. In their STM study [100], Binnig *et al.* interpret these periodicities as due again to structures of the "missing row" type, but with larger channels. In particular, a $(1 \times L)$ missing row model consists of $L-1$ rows missing in the topmost (110) layer, $L-2$ in the second layer, and so on. This gives rise to (111) facets (each of them $L+1$ $\langle \bar{1}10 \rangle$ rows wide), which form—neglecting relaxation effects—an ideal angle of about 35° with the flat (110) surface plane. From these experimental observations, Binnig *et al.* argue that at the origin of the Au(110) reconstruction there is a strong tendency to (111) faceting. This tendency should be driven in turn by a large surface energy anisotropy, where the cost a perfect (110) face is very high compared with (111) [108].

It has been shown in Sec. 4.3 that the Au(100) surface reconstruction is explained in considerable detail as arising by the necessity of surface atoms to switch from a poorly packed (100) layer to a (111)-like densely packed configuration. It is therefore natural to expect that a Au(110) missing row reconstruction should be favoured in the glue model.

4.4.2 Unrelaxed missing row surface energies

Owing to the simple geometry, it is easy to calculate analytically, *neglecting relaxations*, the $T = 0$ surface energies in the glue model for the various $(1 \times L)$ missing row reconstructions and for the perfect (110) surface.

If we assume first-neighbour interactions for both $\phi(r)$ and $\rho(r)$, as in our realization for gold, then in a $(1 \times L)$ missing row surface:

- the top (ridge) row atoms have coordination $n = 7$;
- the bottom (groove) row atoms have coordination $n = 11$;
- all the other atoms in the (111) facets have coordination $n = 9$;
- the remaining atoms, buried below the "surface" atoms above, have the bulk coordination $n = 12$.

To bring the coordination of an atom from 12 to n, it is necessary to break $12 - n$ bonds, so that the associated energetic cost is

$$\epsilon(n) = -\frac{12 - n}{2}\phi + U(n) - U(12) \tag{4.4}$$

where ϕ (which is negative) is the two-body potential at the first-neighbour distance d.

Therefore, the surface energy $\sigma^{(L)}$ for a $(1 \times L)$ missing row surface is given by

$$\sigma^{(L)} = \frac{1}{LA}[\epsilon(7) + \epsilon(11) + 2(L-1)\epsilon(9)] \tag{4.5}$$

where $A = d^2\sqrt{2}$ is the area occupied by an atom in a perfect (110) plane. This equation recovers for $L = 1$ the surface energy of a perfect (110) face

$$\sigma^{(1)} = \frac{1}{A}[\epsilon(7) + \epsilon(11)] \tag{4.6}$$

while in the limit $L \to \infty$ it gives

$$\sigma^{(\infty)} = \frac{2}{A}\epsilon(9) \tag{4.7}$$

Such a "$(1 \times \infty)$" reconstructed surface is simply a slanted (111) surface, and its surface energy is of course that of a (111) multiplied by the inverse of the cosine of the tilting angle (about 35°):

$$\sigma^{(\infty)} = \sqrt{\frac{3}{2}}\sigma^{111} \simeq 1.225\sigma^{111} \tag{4.8}$$

From the above results, we can write

$$\sigma^{(L)} = \frac{1}{L}\sigma^{(1)} + \left(1 - \frac{1}{L}\right)\sigma^{(\infty)} \tag{4.9}$$

In this simple model, therefore, $\sigma^{(L)}$ changes linearly from $\sigma^{(1)}$ to $\sigma^{(\infty)}$ as $1/L$ is decreased from 1 to 0. It may also be noted that

$$\sigma^{(2)} = \frac{\sigma^{(1)} + \sigma^{(\infty)}}{2} \tag{4.10}$$

In order to determine the lowest surface energy state of the surface, we evaluate, using Eq. (4.4), the difference

$$\Delta\sigma \equiv \sigma^{(1)} - \sigma^{(\infty)} = \sigma^{(1)} - \sqrt{\frac{3}{2}}\sigma^{111} = \frac{U(7) - 2U(9) + U(12)}{A} \sim \frac{4U''(9)}{A} \tag{4.11}$$

The conclusions that can be drawn from this analysis, based on neglecting relaxations, are the following:

- If only a first-neighbour pair potential is used, there is no difference in surface energy between all the $(1 \times L)$ missing row surfaces, including $L = 1$ (unreconstructed surface).

- In presence of a glue term, the reconstruction is favoured ($\Delta\sigma > 0$) if $U(n)$ has a positive curvature in a wide region around $n = 9$, disfavoured ($\Delta\sigma < 0$) in the opposite case. Note, however, that the former condition is usually satisfied when $U(n)$ is fitted to other physical properties. In particular, U'' *must* be positive around $n = 12$ to give a positive Cauchy pressure (see Eq. (1.57)).

- As a peculiar consequence, it is impossible to model f.c.c. metals whose (110) surface do not reconstruct (e.g., Cu) with a *first-neighbour* glue as done for Au. At the very least, second neighbours must play a role in that case.

- If reconstruction is favoured, the "best" state is that with $L = \infty$, which corresponds to a tilted (111) plane. (1×2) is *not* particularly good in a picture where relaxations are absent [109].

The results of the above analysis somewhat contradict the experiments. Of course, a $(1 \times \infty)$ would take in practice an infinite time to form when starting from a perfect (110) plane, for kinetic reasons. However, experimental results indicate the (1×2) as the *most stable* state for the surface, and (1×3), ... as *metastable*, and no tendency to increase indefinitely the size of the facets is observed.

While this may seem a failure of the model, or a limitation due to the short range of the interactions, it is really a consequence of neglecting atom relaxations. As it will be shown below, relaxations are very strong on this surface, and the energy gained from them is larger than the energy gained from reconstruction.

In the following Subsections, we report about the energetics (4.4.3), the structure (4.4.4) and the low-temperature behaviour (4.4.5) of the Au(110) surface in the glue model, studied using molecular dynamics [110].

4.4.3 Energetics

We use molecular dynamics (MD) as a tool for searching the energetically optimal configuration, following the procedure outlined in Sec. 4.2. The systems chosen for our study are (110) slabs of sufficient thickness (twelve to twentyfour layers) and variable lateral (x, y) size. A relatively fast quenching procedure (about 2000 MD steps) turned out to be sufficient to optimize the energy reliably for all the geometries we have studied. We have applied this procedure first of all to a flat Au(110), and then to the $(1 \times L)$ missing row reconstruction models. Displacive reconstruction models [98], like the "sawtooth" model [111], are automatically included in the search, and need not be pursued separately.

For each starting point, we have searched and reached the lowest energy E_0, and the corresponding optimal structural configuration. Table 4.2 presents the surface energy, defined by Eq. (4.1), and the percent

Structure	$\sigma\,(\mathrm{meV/\AA^2})$	$\Delta d_{12}\,(\%)$	$\Delta d_{23}\,(\%)$	$\Delta d_{34}\,(\%)$
(1×1) ideal	150.4	0	0	0
(1×2) ideal	139.5	0	0	0
$(1 \times \infty)$ ideal	128.7	0	0	0
(1×1) relaxed	122.5	-33.9	$+6.9$	$+1.3$
(1×2) relaxed	107.4	-27.5	-4.7	-2.2
(1×3) relaxed	109.8	-30.8	-4.8	-10.2
(1×4) relaxed	109.5	-31.9	-5.2	-8.3
(1×5) relaxed	109.4	-36.0	-6.9	-10.0
(1×6) relaxed	110.0	-33.1	-14.1	-8.3
$(1 \times \infty)$, rel. (111)	118.3			
$(1 \times \infty)$, rec. (111)	108.0			

Table 4.2:

Optimal surface energies and multilayer relaxations for various models of Au(110). All the structures except (1×1) are of the missing row type. The values relative to $(1 \times \infty)$ are based on (111) surface energies $\sigma^{111}_{ideal} = 105.1\,\mathrm{meV/\AA^2}$, $\sigma^{111}_{rel} = 96.6\,\mathrm{meV/\AA^2}$, $\sigma^{111}_{rec} = 88.1\,\mathrm{meV/\AA^2}$, calculated in Sec. 4.5.

variations of the average (110) interlayer distances $\Delta d_{i,i+1}$, relative to our bulk value $d_0 = 1.439$ Å.

We note, in the first place, that simple relaxation is by itself able to reduce drastically the surface energy. However, a small but definite extra energy gain is obtained by reconstructing (displacive reconstruction models are not listed, as they are found to *raise* the surface energy). The best configuration is found to be the (1×2) missing row, in agreement with experimental evidence presented in Subsec. 4.4.1 and with other recent *ab initio* [83] and empirical or semiempirical [112,113] theoretical studies.

Contrary to the approximate treatment presented in 4.4.2, we find the surface energies of the (1×3), (1×4), ..., missing row reconstructions to be higher than (1×2). The difference, however, is extremely small. This may explain the above mentioned observations of (1×3) or (1×4) local configurations in STM data [100], and of (1×3) by LEED [92] and He-scattering [114]. It probably also has a bear on the detailed mechanism of disappearance of (1×2) ordering at high temperatures [115,116,117] or through silver deposition [118].

As a last comment on energetics, we note that, knowing the Au(111) surface energies calculated in Sec. 4.5, we automatically have the "$(1 \times \infty)$" missing row energies. If the (111) facets are taken to be themselves unreconstructed, then the "$(1 \times \infty)$" energy is higher than any of the $(1 \times L)$ missing row models. However, at some value of L, reconstruction should set in on the (111) facets [129], leading to further energy lowering. Although we have not tried to verify this for any finite L, we can still confirm that this is the case for $(1 \times \infty)$. The $(1 \times \infty)$ slanted *and* reconstructed (111) has in the glue model a surface energy only slightly higher than the optimal (1×2) missing row surface.

4.4.4 Structure

Now, we turn to a discussion of the Au(110) surface structure. Table 4.2 already indicates that all situations display a very substantial contraction of the first-second layer distance. This is a typical effect of the

	$T = 0\,\mathrm{K}$			$T = 300\,\mathrm{K}$		
Atom	x	y	z	x	y	z
A	0.266	0.000	8.185	0.000	0.000	8.204
B	1.496	−1.752	7.141	1.444	−1.770	7.150
C	1.496	1.752	7.141	1.444	1.770	7.150
D	−0.027	0.000	5.586	0.000	0.000	5.599
E	0.022	4.070	5.955	0.000	4.084	5.994
F	1.436	−2.153	4.363	1.444	−2.169	4.393
G	1.436	2.153	4.363	1.444	2.169	4.393
H	0.001	0.000	2.839	0.000	0.000	2.837
K	−0.001	4.070	2.902	0.000	4.084	2.913
M	1.439	−2.040	1.452	1.444	−2.048	1.459
N	1.439	2.040	1.452	1.444	2.048	1.459
O	0.000	0.000	0.000	0.000	0.000	0.000
P	0.000	4.070	0.011	0.000	4.084	0.013

Table 4.3:
Coordinates, in Å, of the atoms in the (1×2) reconstructed surface unit cell. Direction x is $\langle \bar{1}10 \rangle$, y is $\langle 001 \rangle$, z is $\langle 110 \rangle$ (surface normal). $T = 0\,\mathrm{K}$ denotes the optimized geometry, while average coordinates are given at $T = 300\,\mathrm{K}$. The atom labels are as in Fig. 4.12. The origin has been arbitrarily placed on the atom O. The bulk lattice parameter of the crystal, calculated in Sec. 3.1, is $a = 4.070\,\text{Å}$ at $T = 0$ and $a = 4.084\,\text{Å}$ at $T = 300\,\mathrm{K}$.

glue. Contraction takes place against two-body forces, but it improves coordination, which is very poor for a surface atom. Deep multilayer relaxations are also created as a byproduct.

A lateral picture of our optimized (1×2) surface structure is presented on Fig. 4.12. Atom coordinates at $T = 0$ and $T = 300\,\mathrm{K}$ are reported in Table 4.3. The finite temperature positions have been extracted from a 10000-steps MD run for a 20-layers slab with a 8×6 in-plane size. The coordinates reported are the result of averages both on time and on the 48 (1×2) surface unit cells available (24 on each

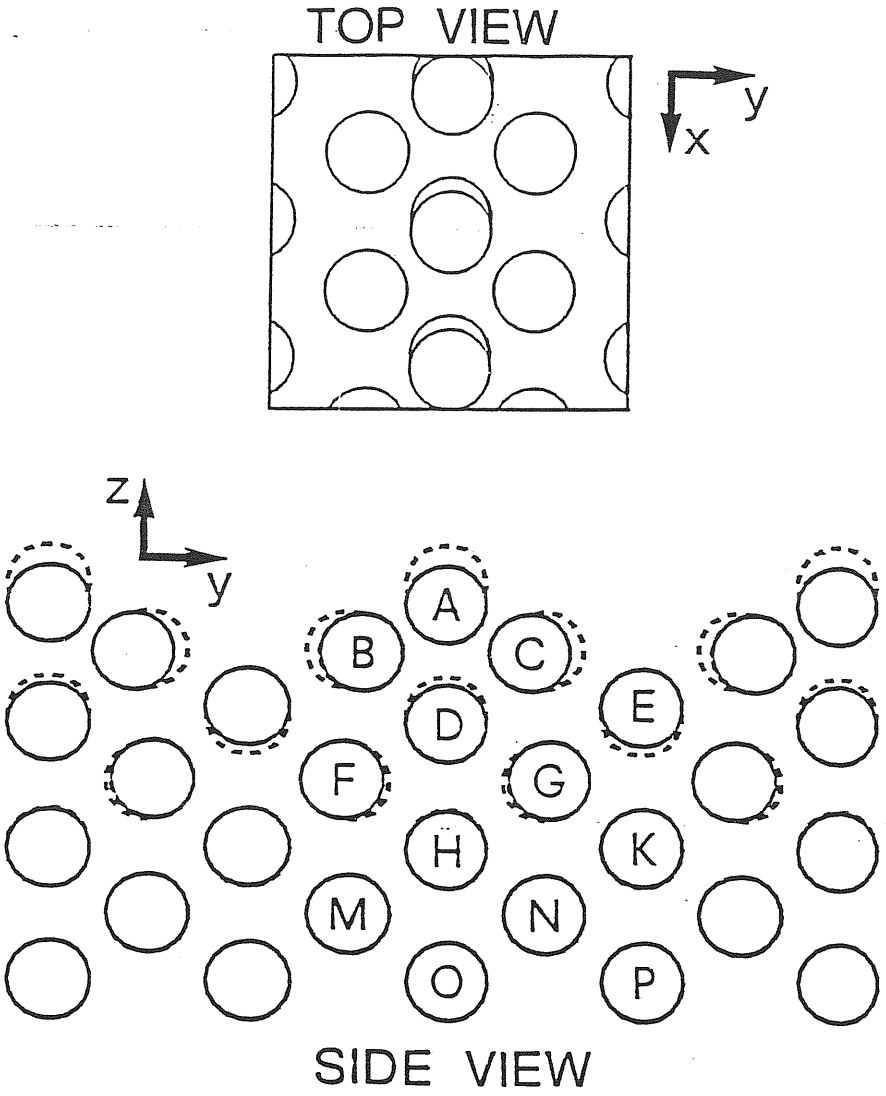

Figure 4.12:
Side and top views of the optimized $T = 0$ (1×2) missing row surface. All atomic positions shown to scale (*not* schematic). Atom radii are arbitrarily chosen to be 0.85 Å. In the side view, the solid circles correspond to the actual atomic positions, the dashed circles to the ideal, unrelaxed missing row structure. In the top view (first three layers shown), the sliding distortion of the top row along its own direction partly uncovers third layer atoms.

side of the slab).

The topmost row is deeply sunken, with a 27% contraction onto the second layer. This value exceeds only slightly the estimates extracted from recent data, indicating a contraction in the range 18%–20% [105,106,107]. It disagrees totally with earlier reports of outwards expansion [101,102].

The lateral motion of second layer atoms is smaller ($y_B - y_M = 0.29$ Å), but appears to be opposite in sign to that indicated experimentally [105]. A similar "inward" motion of second layer atoms was also obtained by Daw for Pt(110) using an "embedded-atom" scheme [119], and seems to be typical of this class of Hamiltonians.

The third layer is buckled: the atoms directly underneath the missing row are slightly pushed up, while the others are strongly pushed down by the first-layer atoms, their first (bulk) neighbours. Our total third-layer buckling is $z_E - z_D = 0.37$ Å. The corresponding experimental values are reported in the range 0.20–0.24 Å [105,107]. Again, this confirms a qualitative agreement with experiments, while in the detail our numbers seem somewhat too large. The relaxation pattern continues, while attenuating progressively, into a multilayer relaxation which falls below 0.1% only around the 8th layer.

4.4.5 A "sliding distortion" of the top row

Our optimized (1×2) missing row structure has also an unexpected frozen-in secondary lattice distortion, clearly visible in the top view in Fig. 4.12. All the topmost $\langle \bar{1}10 \rangle$ rows have undergone a uniform "sliding" translation $x_A - x_O = 0.27$ Å along their own direction, and the second-layer atoms follow with $x_B - x_M = 0.06$ Å. The corresponding surface energy decrease is small, about 0.67 meV/Å^2, or 180 K per surface atom, with respect to the (unstable) arrangement where the sliding distortion is removed.

The energetic cost of a single (left-right) defect in a row is large ($J_{||} \simeq 1100$ K) while the coupling between neighbouring rows (8.14 Å apart) is tiny ($J_{\perp} \simeq 1.7$ K). Thus, it is expected that this symmetry-lowering dis-

tortion should disappear with an extremely anisotropic Ising-like transition. If we, quite roughly, use the formula of Ref. [120]

$$k_B T_c \sim 2J_{||}/\ln(J_{||}/J_{\perp})$$

to get an estimate for T_c, we anticipate a transition somewhat above room temperature.

We obtain a much more accurate determination of T_c by molecular dynamics. We have carried out a (microcanonical) study of the low-temperature properties of our (1×2) missing-row surface. The main structural features described above remain essentially unchanged up to room temperature. However, the sliding distortion disappears above roughly $T_c \simeq 230\,\mathrm{K}$. Table 4.3 clearly shows that at room temperature the distortion is absent. It should be pointed out that such a distortion might explain a symmetry breaking reported by spin-polarized LEED [95]. Further low-temperature studies of Au(110) would be helpful to clarify this point.

At and above room temperature, we can observe an increasingly frequent sliding motion of entire top rows. This massive sliding would of course become impossible for larger cell sizes, but it could easily occur in presence of defects. It is interesting to note that the defects observed by Binnig *et al.* by STM [100] seem precisely connected with the sliding of a top row, which we find in our glue model. Moreover, sliding rows might provide a clue to the understanding of the highly anisotropic diffusion rates observed on the similar Pt(110) surface [121].

4.5 Au(111) surface reconstruction

4.5.1 Experiments

Gold is the only known f.c.c. metal which exhibits reconstruction on the already well-packed (111) surface [77]. Experimentally, Au(111) has long been known to reconstruct with a periodicity which is probably incommensurate, numerically close to $(23 \times \sqrt{3})$, as established by electron diffraction [122,123,124], transmission electron microscopy

[125,126,127,128] He-diffraction [129] and STM [130]. To explain this, it has been supposed that the uppermost (111) layer is somewhat contracted along the $\langle 1\bar{1}0 \rangle$ direction, while contraction is absent in the orthogonal $\langle 11\bar{2} \rangle$ direction.

Due to the contraction, epitaxy of the first layer onto the second is imperfect. Refinements of this model [127] suggest that f.c.c. epitaxy might remain essentially exact over a whole region. Then, a phase slippage (soliton) occurs, leading to a second region of good epitaxy, now of h.c.p. type. Again, a second phase slippage would then lead to a new f.c.c. region, and so on. Harten *et al.* [129] have shown that this domain model is able to give an interpretation to He-diffraction data, although the soliton regions do not seem as narrow as originally proposed, but rather have an extension of about 12 Å.

Theoretically this situation is quite analogous to that occurring, e.g., in a rare gas adsorbed film, and has been widely discussed, in general phenomenological terms [90]. Nevertheless, it is quite interesting to ask whether a model based on explicit interatomic forces, such as the glue model, might account for this rather unusual behaviour of Au(111).

It has been shown in Section 4.3 that the tendency to form a closely packed, (111)-like surface layer, induced by the glue Hamiltonian, explains the Au(100) surface reconstruction. In fact, the many-body energy decrease obtained by improving surface coordination is larger than the two-body energy increase due to the bond lengths reduction, and the total energy decreases by reconstruction. On a (111) surface, however, the packing is already good. Although surface contraction always acts to reduce the glue energy, the final result of the energetic balance between two-body and many-body forces is not easy to predict.

In this Section, we describe the results of a molecular dynamics investigation of the $T = 0$ surface structure of Au(111) in the glue model [131]. More details on this work can be found in Ref. [132].

4.5.2 Energetics and structure

A molecular dynamics simulated annealing procedure has been used as a tool for searching the optimal surface structure, as described in Sec. 4.2. In particular, for the (111) surface we use 10-layer slabs, with free boundary conditions in the $\langle 111 \rangle$ direction, and periodic boundary conditions in the in-plane directions $\langle 1\bar{1}0 \rangle$ and $\langle 11\bar{2} \rangle$. The length of the box along $\langle 1\bar{1}0 \rangle$ is Md (where $d = 2.88$ Å is the first-neighbours distance and M an appropriately chosen integer), while the length along $\langle 11\bar{2} \rangle$ is $2\sqrt{3}d$. The number of atoms in a general layer is $4M$, while that in the outermost surface layer is permitted to increase to $4(M+1)$. If the surface wants to reconstruct by in-plane contraction, as suggested by earlier discussions, then such an increase should lead to a lowering of surface energy, provided M is conveniently chosen.

We have found that this is indeed the case. Table 4.4 summarizes the values obtained for the surface energy as a function of the cell length M. For the relaxed but not reconstructed surface, corresponding to the limit $M \to \infty$, the surface energy (defined as in Eq. 4.1) is $\sigma_{nr} = 96.6\,\mathrm{meV/Å^2}$. For all $M > 5$, $\sigma(M) < \sigma_{nr}$, and the optimal value is $\sigma(11) = 88.1\,\mathrm{meV/Å^2}$. Hence the optimal (111) surface geometry of our glue model is indeed reconstructed as expected, but with a shorter periodicity, roughly $(11 \times \sqrt{3})$. A picture of our optimized surface structure is shown in Fig. 4.13.

We can make the following comments and qualifications:

1. The surface energy minimum at $M = 11$ is very asymmetric and shallow only if M is increased above 11. For example is still as low as $90.2\,\mathrm{meV/Å^2}$ when M is as high as 23. This means that grand-canonical fluctuations (allowed in presence of source terms which could be present in the form of steps, etc.) might tend to increase the average M value at finite temperatures. In turn this would bring the theoretical result closer to the experimental value $M = 23$. The behaviour of $\sigma(M)$ is reproduced reasonably well

Structure	σ (meV/Å^2)	$\Delta s_{12}(\%)$	$\Delta s_{23}(\%)$	$\Delta s_{34}(\%)$
$(4 \times \sqrt{3})$ relaxed	114.4	+1.4	+2.4	−0.3
$(5 \times \sqrt{3})$ relaxed	99.4	−0.5	+2.5	−0.3
$(6 \times \sqrt{3})$ relaxed	93.2	−1.8	+2.6	−0.3
$(7 \times \sqrt{3})$ relaxed	90.4	−2.6	+2.6	−0.3
$(8 \times \sqrt{3})$ relaxed	89.1	−3.2	+2.6	−0.3
$(9 \times \sqrt{3})$ relaxed	88.5	−3.7	+2.6	−0.3
$(10 \times \sqrt{3})$ relaxed	88.3	−4.1	+2.6	−0.3
$(11 \times \sqrt{3})$ relaxed	88.1	−4.4	+2.6	−0.3
$(12 \times \sqrt{3})$ relaxed	88.3	−4.6	+2.6	−0.3
$(13 \times \sqrt{3})$ relaxed	88.4	−4.8	+2.6	−0.3
$(15 \times \sqrt{3})$ relaxed	88.8	−5.1	+2.6	−0.3
$(18 \times \sqrt{3})$ relaxed	89.3	−5.4	+2.5	−0.3
$(23 \times \sqrt{3})$ relaxed	90.2	−5.8	+2.5	−0.3
$(33 \times \sqrt{3})$ relaxed	91.4	−6.1	+2.4	−0.3
$(50 \times \sqrt{3})$ relaxed	92.5	−6.4	+2.4	−0.3
non-rec., relaxed	96.6	−7.9	+1.2	−0.1
non-rec., ideal	105.1	0	0	0

Table 4.4:

Surface energies and variations of the average interplanar distances $\Delta s_{i,i+1} = (s_{i,i+1} - s_0)/s_0$, where $s_0 = 2.35$ Å is the bulk (111) spacing, for several (111) reconstruction geometries.

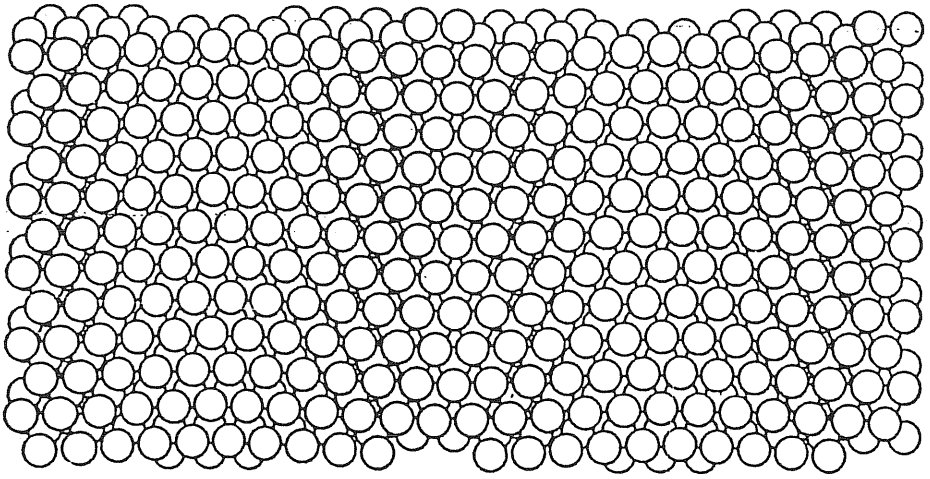

Figure 4.13:
Top view of the optimized Au(111) $(11 \times \sqrt{3})$ surface. Twelve unit cells, arranged in a 2×6 array, are shown.

by a second order expansion in powers of $1/M$:

$$\sigma(M) - \sigma_{nr} \simeq -\mu/M + \frac{1}{2}\nu/M^2 \qquad (4.12)$$

with $\mu \simeq 200\,\mathrm{meV/\AA^2}$ and $\nu \simeq 2400\,\mathrm{meV/\AA^2}$. μ can be regarded as the "chemical potential" of the reconstruction stripes.

2. There are many similar (but not identical) $T = 0$ configurations, all of which have the same M and very close surface energies (typically within $\pm 0.05\,\mathrm{meV/\AA^2}$ at $M = 11$). The difference between any two such structures consists mainly in a very small lateral $\langle 1\bar{1}0 \rangle$ shift of position of the topmost layer relative to the second layer. Therefore in our model the average structure, even at very low temperatures, is not identical to that belonging to any of the $T = 0$ optimal structures. The relevance of this point may be somewhat academic, since for example already at 100 K the thermal fluctuations overwhelm those due to this sort of "spin-glass" problem.

3. Morphologically, the optimal $T = 0$ structures are all characterized

by an "undulating" behaviour of each single top layer $\langle 1\bar{1}0\rangle$ atomic row, with the peak positions corresponding to f.c.c. or h.c.p. crystal sites. The in-plane $\langle 11\bar{2}\rangle$ undulation, amounting to about 1.0 Å, is clearly visible in Fig. 4.13. A corresponding small vertical $\langle 111\rangle$ undulation is also present, with periodicity half of the in-plane undulation, and a peak-to-peak amplitude of 0.12 Å.

4. All the cells display oscillatory multilayer relaxations. s_{12} increases when M is decreased to compensate for the increment of in-plane packing. For the optimal $(11 \times \sqrt{3})$ structure, the average first-second layer spacing is contracted by 4.4% (0.10 Å) with respect to the bulk value, while the second-third layer spacing is increased by 2.6% (0.06 Å).

5. Considering one $T = 0$ "optimal" structure, we have studied the $\langle 1\bar{1}0\rangle$ phase of the first layer lattice (relative to an ideal (111) bulk layer lattice) in an attempt at identifying f.c.c. and h.c.p. epitaxial regions, as well as soliton regions. Our result indicates, somewhat surprisingly, a nearly uniform $\langle 1\bar{1}0\rangle$ in-plane shrinking, with rather narrow f.c.c. and h.c.p. regions separated by wide, smooth transition regions. This disagreement with the experimental model [127,129] seems genuine, and the reasons for it are not yet clear.

Within the present MD approach, it might seem that we are ideally equipped for the study of (111) phase transitions. In particular, a transition between a directional ("striped") reconstruction as assumed here and three simultaneous such reconstructions at 120°, yielding an overall isotropic surface, has been reported near 1000 K [126] and discussed in phenomenological terms by Okwamoto and Bennemann [133]. A direct study has so far proved unfeasible, for two reasons both connected with the MD box. The box size is far too small to allow roughening of the solitons and possible formation of vortices, as one expects in such a system [90]. Moreover, its chosen directionality pre-determines at the outset whether one will go for a uniaxial, or hexagonal, reconstruction. While at $T = 0$ surface energy can tell which one is best, we have no

free energy that can be practically used at $T \neq 0$. Surface melting, on the other hand, is a short-range phenomenon and its study does not suffer from this problem. An investigation of the behaviour of both the reconstructed and the unreconstructed Au(111) surface in the present glue model is reported in Chapter 5.

4.6 Summary

We have shown in this Chapter that the glue Hamiltonian provides a rather realistic energetic and structural description of the reconstructed surfaces of gold.

This gives us important indications on the nature of this phenomenon. Since the glue forces are defined exclusively in terms of atom coordinations, the driving force for surface reconstruction in noble metals has been shown to be the tendency of surface atom to increase their coordination, induced in turn by the glue forces which mimic electronic d-band effects. While in other metals this tendency is weak, so that first-layer contraction suffices, in several noble metals the need to increase coordination is so strong as to make favourable extensive first-layer rearrangements. Complicated geometries arising from these rearrangements are simply a consequence of the packing tendency, and angular forces (not included in the glue) play no important role.

Strong first-layer contractions also have important consequences on surface dynamics. A recent dynamical study of Au(110) (1×2) performed with our model predicts the existence of anomalous high-frequency phonon modes, which presumably arise because of a stiffening of the surface force constants caused by the large inward relaxation of the topmost row [134].

A study of the behaviour of Au(111) near the melting temperature is presented in the next Chapter.

Chapter 5

Surface melting behaviour of Au(111)

5.1 The surface melting hypothesis

The idea that crystal melting could be a surface-initiated process is very old [10], and some evidence has been provided long ago by macroscopic means [135]. Recently, interest in surface melting has been revived by qualitative ideas [136], new theories [137], as well as by newly available microscopic surface tools [138], and by the possibility to realistically simulate the warm crystal surface on the computer (for a general review on surface melting, see Ref. [139]).

The best simulation so far is that of Lennard-Jones (LJ) crystal surfaces, thoroughly characterized by several researchers [28,140,141,142,143]. They show clear evidence of surface-nucleated melting, down to temperatures as low as $\frac{3}{4}T_m$, in remarkable agreement with predictions based on simple qualitative models [136,144].

Experimentally, surface-initiated melting has been recently demonstrated on Pb(110) [138] as well as on Ar [145]. For Pb(110), a close correlation has been found [146] between anharmonic surface outwards relaxation and the onset of surface disorder, as predicted by Jayanthi *et al.* [144].

The general situation is however still far from clear. In the case of

Lennard-Jones crystals, the role of vacancy-related surface roughness could be important [142], and is as yet unclear[1]. Moreover, the thermodynamics of the warm surface is not well established, in that one does not know if surface melting is or is not a well-defined phase transition, and of what type. Finally, metals are most commonly used for microscopic experiments, but a Lennard-Jones crystal is certainly not a good description for them.

For these reasons, computer simulation studies of hot metal surfaces would be very helpful to improve our understanding of surface melting. Until very recently, however, the lack of adequate force models prevented the possibility to perform such calculations. In particular, the need to reproduce correctly both surface energetics and vibrational properties *at the same time*, makes pairwise models completely inadequate for this purpose [29], as discussed in Sec. 1.1.

The glue model, on the other hand, satisfies the requirements mentioned above, and seems to be a valid tool for investigating the melting behaviour of a metallic surface. Therefore, we have undertaken an extensive molecular dynamics study of a gold surface at high temperature [148].

As detailed in Chapter 4, all low-index surfaces of gold in the glue model are unstable in their normal, bulk-like surface arrangement, and reconstruct to achieve (locally) a higher packing density. For the purpose of the study described here, it seemed appropriate to choose the surface where atomic rearrangements are less dramatic, namely Au(111) (see Sec. 4.5). Moreover, the non-reconstructed Au(111), although energetically disfavoured, could also be studied by molecular dynamics. In fact, it can be easily preserved in a metastable state, because surface reconstruction cannot occur without the addition of a few extra atoms at the outset.

The results for the reconstructed and non-reconstructed Au(111) are reported respectively in Sec. 5.2 and 5.3. A discussion on the role of many-body forces on the melting behaviour of well-packed metal sur-

[1]However, one can prove that, once surface melting has begun, roughening will necessarily ensue below the triple point, see Ref. [147].

faces is presented in Sec. 5.4.

5.2 Non-melting of reconstructed Au(111)

We have undertaken a series of molecular dynamics (MD) calculations to characterize the melting behaviour of the Au(111) surface. We have used the "glue" potential and a slab geometry, with the two bottom layers assumed to be rigid in their bulk-like positions to mimic the contact with a semi-infinite bulk. Periodic boundary conditions are used along x, y, and free motion is allowed along z (zero pressure). In order to minimize spurious slab effects, the lateral box size was adjusted to match the mean lattice parameter at $T \sim 1350\,\mathrm{K}$, as extracted from the bulk simulation described in Sec. 3.1.

Atom evaporation is a very improbable event in this system, and we have observed none during our simulations. On the other hand, we have directly checked that a surface vacancy or adatom has an extremely short lifetime ($\sim 10^{-13}$ s and $\sim 10^{-12}$ s respectively) before being annealed out. Therefore, the reconstructed surface is free of vacancies and adatoms at almost any time. Hence, we argue that a solid-vacuum interface—such as that realized in our simulation—should behave very similarly to the equilibrium solid-vapour interface[2].

For most of the calculations we have used slabs of 40 layers with 56 particles on each layer. Our (x,y) cell is defined by $L\frac{a}{2}\langle 1\bar{1}0\rangle \times M\frac{a}{2}\langle 11\bar{2}\rangle$ with $L = 7$ and $M = 4$. In this approximately square cell, we can accommodate either an unreconstructed surface (56 top layer atoms), or a denser unreconstructed surface (64 top layer atoms). This corresponds to higher surface density $\delta\rho_s/\rho_s \sim 14\%$. This value is slightly higher than the value $\delta\rho_s/\rho_s \sim 9\%$. which is optimal for our potential (as discussed in Sec. 4.5) but has the advantage of requiring a smaller size cell. The total number of particles with reconstruction is therefore $N = 56 \times 39 + 64 = 2248$, of which 112 belonging to the rigid layers. This

[2]This reasoning neglects asymmetry between surface vacancies and adatoms, which if important might cause a gradual decrease of surface density with T. We do not expect this effect to be relevant in our case.

requires about 1 CPU second per MD step on an IBM 3090 with Vector Facility.

Annealing of this system at low temperatures leads to the ordered surface structure studied in detail in Sec. 4.5. This reconstructed surface is, as it should, much more stable and well packed than the corresponding unreconstructed surface.

To check for lateral size effects we have doubled, in some calculations, the lateral size in each direction (bringing in this way to 224 the number of particles of an unreconstructed layer), and decreased the number of layers to 12 (of which 2 rigid) to limit the increase in the total number of particles. In these runs we have found no difference in behaviour with the other runs, thus indicating that 56 particles per layer are sufficient for present purposes.

We have performed both microcanonical and canonical runs. Canonical runs have been realized by crudely rescaling the particles velocities at each time step to adjust the kinetic energy to conform to the desired temperature. Figure 5.1 summarizes the results of the canonical runs for the reconstructed Au(111) surface, and presents the number n of molten layers at each temperature.

There are several qualitative ways to define a molten layer:

(a) the intra-layer pair correlations have lost their crystalline shell structure;

(b) diffusion is linear with time and large;

(c) the average energy per atom is $\sim 0.12\,\mathrm{eV}$ larger than in a typical bulk layer;

(d) the in-plane orientational (hexatic) order parameter O_6 has dropped from close to 1 to close to 0.

We define

$$O_6 = \frac{|\sum_{ij} W_{ij} e^{6i\theta_{ij}}|}{\sum_{ij} W_{ij}} \tag{5.1}$$

where the sums run over first-neighbour pairs and θ_{ij} is the angle which the i-j bond, projected on the xy plane, forms with the x axis. The

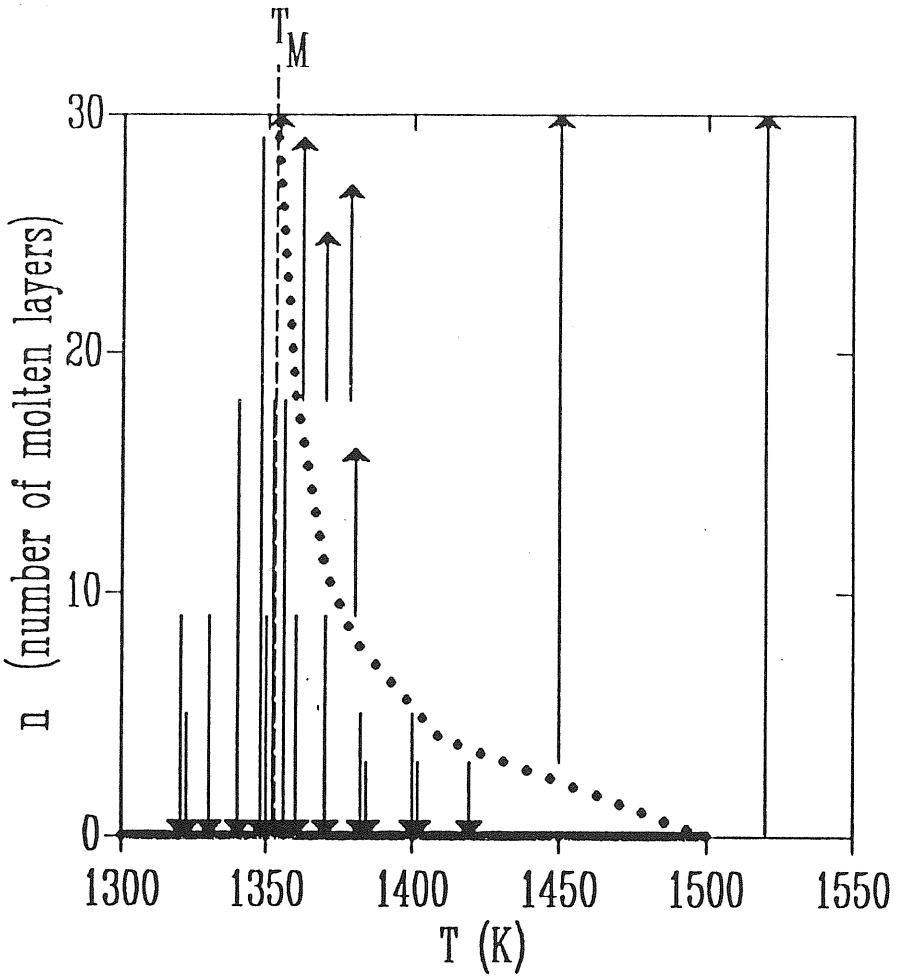

Figure 5.1:
Summary of the runs for the reconstructed Au(111) surface. The dotted line represents the curve of instability $\nu(T)$.

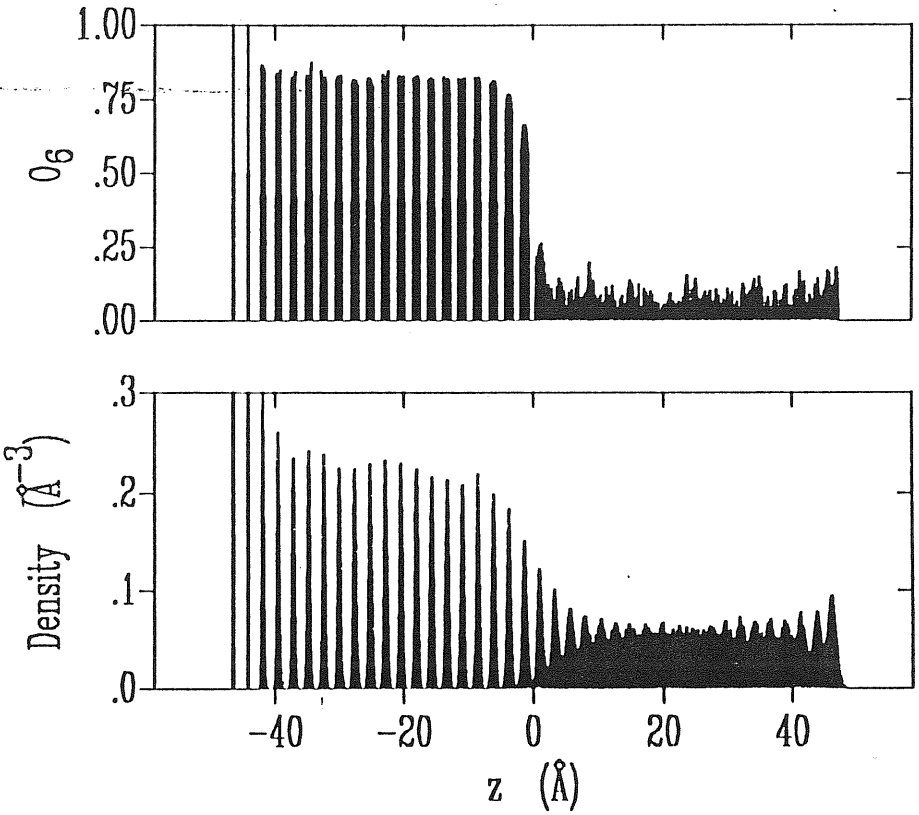

Figure 5.2:
Orientational order parameter O_6 and (x, y)-averaged density, for a micro-canonical sample with $\langle n \rangle = 18$ molten layers and $\langle T \rangle = 1350\,\mathrm{K}$. The two leftmost layers are rigid. These data have been averaged over 2000 MD steps.

weight function

$$W_{ij} = \exp\left(-\frac{(z_i - z_j)^2}{2\delta^2}\right), \tag{5.2}$$

with $\delta = 0.59\,\text{Å}$, has the purpose of filtering out all "non-coplanar" neighbours. Figure 5.2 exemplifies the behaviour of O_6 and of the (x, y)-averaged atomic density for a sample with $n = 18 \pm 2$ molten layers and $\langle T \rangle = 1350\,\mathrm{K}$. As a practical criterion, we call "solid" a layer with

$O_6 > \frac{3}{4}$. We have checked that this definition generally fits well with the other criteria (a), (b), and (c) above. In particular, diffusion sets in rather sharply for O_6 smaller than this value.

Returning to Fig. 5.1, each arrow nn' represents a simulation, beginning with n and ending with n' molten layers. Initial configurations with any number n of molten layers are easily generated by a high temperature run ($T > 1600\,\mathrm{K}$) where, starting from an initially solid slab, n grows with time. Each run has typically required $\sim 10^4$ to $\sim 3 \times 10^5$ time steps, the larger times being required for runs close to the melting temperature. Since a time step $\Delta t = 7.14 \times 10^{-15}\,\mathrm{s}$ has always been used, our equilibration times range from $\sim 10^{-10}\,\mathrm{s}$ to $\sim 10^{-9}\,\mathrm{s}$.

We generally find that the energy E of a sample is rather accurately related to temperature and to n by the simple relation

$$E = NC_pT + \Delta H n n_L \tag{5.3}$$

where $C_p = 3.1 \times 10^{-4}\,\mathrm{eV/(K\ atom)}$ is the solid bulk specific heat and $\Delta H = 0.12\,\mathrm{eV/atom}$ is the bulk heat of melting for our model potential. Here n_L is the number of particles in each layer.

Up to a temperature $T_0 = 1357 \pm 5\,\mathrm{K}$, the only equilibrium configuration is crystalline ($n = 0$). Above T_0, we find two possibilities. If the initial liquid thickness is small enough, $n < \nu(T)$, the sample crystallizes, $n' = 0$. For $n > \nu(T)$, the sample melts completely, $n' \to \infty$ (really, $n' \to 35$, due to our finite size and rigid layers). The "unstable line" $\nu(T)$ is oblique, and intersects zero at $T_1 \sim 1500\,\mathrm{K}$. Above T_1, any initial configuration, including $n = 0$, will melt.

We interpret the above as follows. The temperature T_0 is identified with the bulk melting (triple point) temperature $T_m = T_0 = 1357 \pm 5\,\mathrm{K}$. This value is in fairly good agreement with the experimental value $T_m^{exp} = 1336\,\mathrm{K}$, confirming the good accuracy of the glue potential also at high temperatures. The crystalline reconstructed surface is stable below T_m, and remains metastable between T_m and T_1. Thus, microscopic surface melting does not occur on this surface. In principle, this does not imply that macroscopic surface melting, i.e., sudden formation of a thick liquid film extremely close to T_m, might not occur. We simply

cannot address this question with our tools, due to size and time limitations. Within these limits, however, our surface is not only stable up to T_m, but can also sustain overheating by as much as $\sim 100\,\mathrm{K}$ *above* T_m.

5.3 Blocked-melting of unreconstructed Au(111)

It is tempting to relate the lack of microscopic melting of the reconstructed Au(111) to its denser first-layer packing. To test this idea, and also to explore the more general possibility of a totally different behaviour for a slightly different state of the surface, we have carried out a parallel study of the unreconstructed surface. Here, the topmost layer is taken to be simply identical to all other layers, i.e., no extra atoms have been added. This state of the surface might be experimentally accessible, in spite of its substantially higher surface energy σ (at $T = 0$, from Table 4.4, $\sigma_{rec} = 90.4\,\mathrm{meV/\AA^2}$, $\sigma_{unrec} = 96.6\,\mathrm{meV/\AA^2}$).

Figure 5.3 describes our results for the unreconstructed Au(111) surface. Here, the first two layers melt simultaneously at $T^* \sim 1250\,\mathrm{K}$, with an energy increase $\Delta h \sim 0.03\,\mathrm{eV/atom}$, a value much lower than the bulk heat of melting. This may be due to the poor degree of packing of the unreconstructed surface layer and by the concurrent high quality of packing found on the double melted layer. This two-layer melting shows hysteresis, which could indicate a first-order character.

Following this two-layer melting, one might have expected to observe the solid-liquid interface to propagate into the bulk, as T_m is approached further. However, this does not happen, and the double-melted layer state remains stable up to T_m (quite similarly to recent reports about Ge(111) [149]). Moreover, in analogy with the reconstructed surface, the two layer state can be overheated for about $\sim 100\,\mathrm{K}$ above T_m.

We conclude that indeed a situation of poorer surface packing can bring about some microscopic surface melting. Yet, this "nucleus" does not propagate into the bulk to give rise to a thick liquid layer as T_m is approached. In this sense, the lack of surface melting of Fig. 5.1 is confirmed.

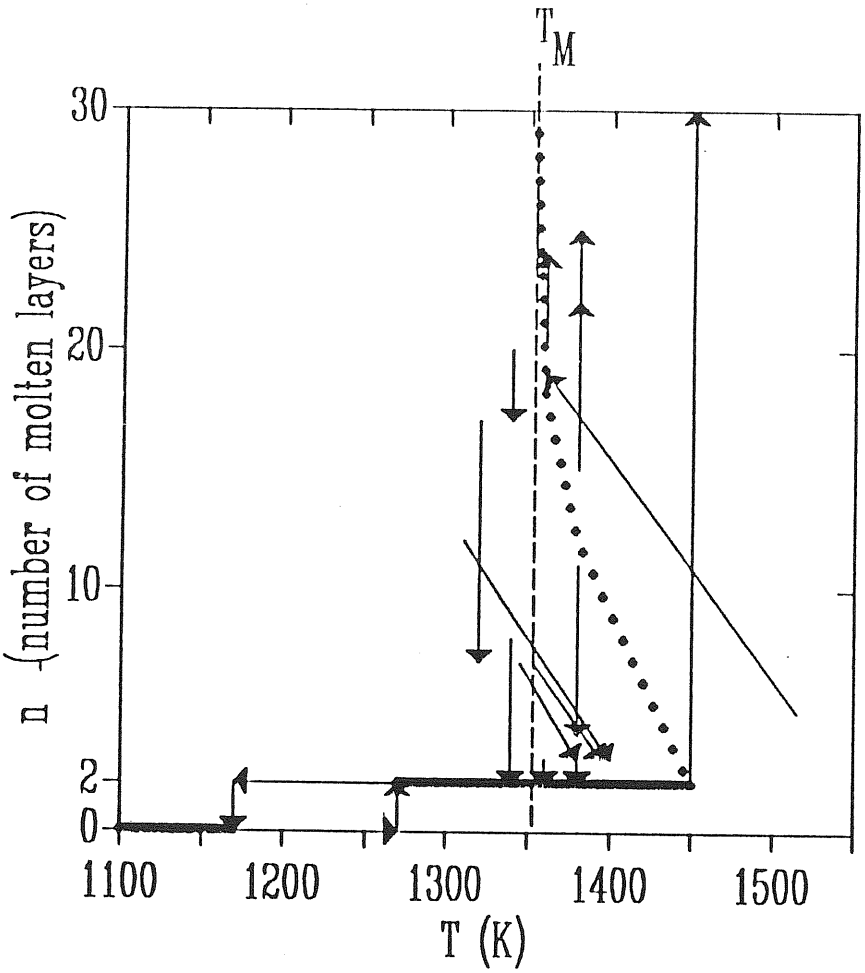

Figure 5.3:
Summary of the runs for the unreconstructed Au(111) surface. The dotted line represents the curve of instability $\nu(T)$.

5.4 Many-body forces and surface stability

We believe the non-melting behaviour of reconstructed Au(111) to be an effect of the many-body "glue" forces. Specifically, the energetics of surface atoms, very poor in a system with two-body forces (such as LJ), becomes very much better once the many-body forces are included. For example, the (relative) excess energy of a surface atom respect to a bulk atom at $T = 0$, $(E_s - E_b)/|E_b|$, decreases from 0.29 for LJ(111) [141] to 0.20 (ideal unrelaxed) to 0.17 (relaxed unreconstructed) to 0.13 (relaxed and reconstructed (111) surface). As a consequence, all entropy-related quantities, such as thermal vibration and expansion, defect concentration, etc., are expected to rise much higher near T_m in a two-body system than in a many-body system.

This particular point finds a direct confirmation by comparison of the LJ results with our Au(111) results. While the LJ surface is wobbly and full of defects already 5% below T_m, our reconstructed surface is still very much bulk-like even *at* T_m, as shown by Fig. 5.4. This point is also particularly evident from the mean-square vibration amplitudes of our reconstructed surface, shown in Fig. 5.5. Even as close to T_m as 5 K, the surface is clearly still vibrationally stable, in contrast with the LJ case [141]. The mean-square first layer vibration amplitude relative to the bulk for our reconstructed Au(111) surface is only 1.5 just below T_m ($T = 1350$ K). The corresponding value for LJ(111) is already as high as 2 at $T/T_m = 0.5$ [140].

Similar considerations also apply with respect to simple models. In the Pietronero-Tosatti model the surface instability is caused precisely by the abnormal entropy-driven growth of surface thermal vibration and expansion. As shown by Jayanthi *et al.* [144], even a small energetic strengthening—such as that caused by inwards relaxation—is very efficient in raising the vibrational surface instability and possibly killing surface melting. The conclusion to be drawn from these considerations is that the improved surface energetics of our metal as compared with,

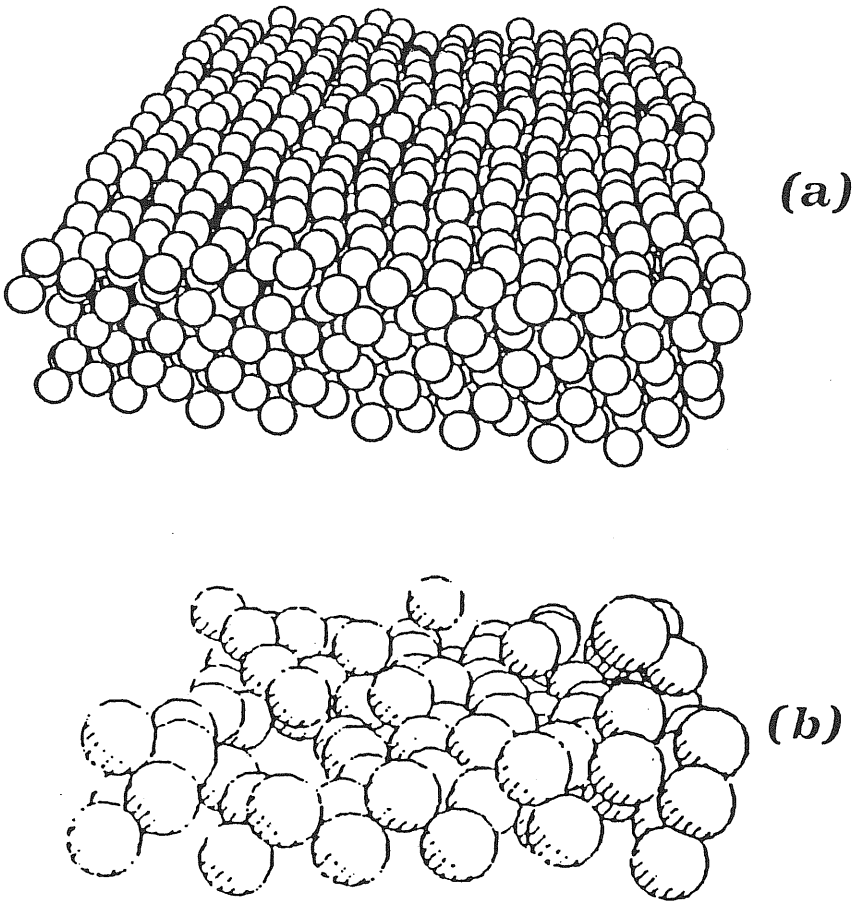

Figure 5.4:
Snapshots of the Au(111) reconstructed surface in the glue model at $T = T_m$ (a), and of the Lennard-Jones (110) surface at $T = 0.95T_m$ (b) (from Ref. [142]). The Au surface still exhibits crystalline order, while the LJ surface is very disordered and full of defects.

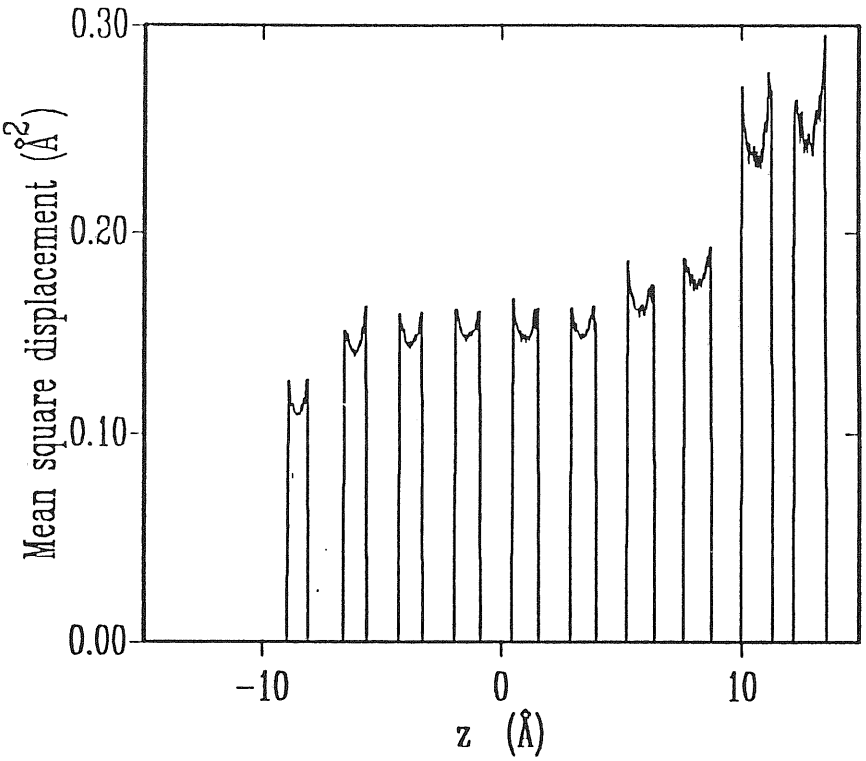

Figure 5.5:
Average mean square displacement $\langle u^2 \rangle$ (sum of the three components) as a function of z for a reconstructed sample at $T = 1350\,\mathrm{K}$, just below T_m. These data refer to a case with 12 layers, of which 2 rigid. The decrease in $\langle u^2 \rangle$ for the leftmost layers is due to the contact with the rigid layers. The average $\langle u^2 \rangle$ for the surface (rightmost) layer is only ~ 1.5 times larger than in the bulk.

say, a LJ crystal, implies a better surface stability against melting. The case of Au(111) is perhaps extreme, and surface stability is so strong as to completely prevent microscopic melting, allowing even the surface to be overheated.

Chapter 6

Structure of gold clusters

6.1 Introduction

The interest in the physics of small metal clusters [150,151,152] is especially related to catalysis and to crystal growth. In both cases, it is important to be able to prepare clusters with controlled size and purity, as well as to characterize their structure and stability. In this business, gold offers a number of advantages, due to its low reactivity and to the possibility of preparing it relatively easily with standard methods (evaporation, chemical deposition, etc.) on different substrates (alumina, SiO_2, graphite, etc.). Supported gold particles of a variety of sizes ($50 < N < 10000$) can thus be investigated with a number of structural tools. In fact gold particles are relatively well known: investigations have been conducted with extended X-ray absorption fine-structure (EXAFS) [153], X-ray diffraction [154], electron diffraction [155], electron microscopy [156,157,158,159,160,161], and more recently STM [162].

Several interesting structures have been reported particularly by high-resolution electron microscopy, among which one can find f.c.c.-cuboctahedra [157,158], icosahedral and decahedral particles [156,158,161], and also amorphous-looking clusters [159].

No information on the structure of free (unsupported) clusters is available. From the "magic numbers", i.e., the N's corresponding to

largest abundances in the mass spectra, special stability seems to correspond in the small size range ($N < 200$) to electron shell filling [163], which parallels very similar evidence in alkali metals.

As for the theoretical study of stability and structural properties of clusters, no relevant work has been done so far on supported aggregates. Several approaches have been pursued instead on free aggregates, which differ strongly in the size range of applicability.

At the most phenomenological extreme, various arguments have been presented (briefly reviewed in Sec. 6.2), based on Wulff constructions, arising from anisotropic surface tensions and theory of elasticity [164,165]. It is reasonable to apply this type of approaches to rather large clusters, where departure from "bulk + flat surface" conditions is minimal [166]. The situation of smaller clusters with, say, $N < 1000$, seems however too extreme for these models to retain a credible predictive power.

At the opposite microscopic extreme are the *ab initio* calculations based on either Hartree-Fock (HF) or configuration interaction (CI) schemes [167] or LDA, without [168,169,170,171] or with [172,173] the possibility for the atoms to move. These approaches are of course very satisfactory. However, they are computationally very heavy, and have not been practically implemented for N larger than a few tens of atoms. Even with the most advanced techniques [2] it is not foreseeable that $N > 100$ could be attacked at least in the next few years.

Model calculations of microclusters with a few hundred atoms have been attempted using a tight-binding description of the electron states [174,175,176]. These results provide an interesting starting point for discussion. However, the predictive power of this type of approach seems limited.

Summarizing, there is a size range, roughly $100 < N < 1000$, where no quantitative theory is readily available. This range is actually very interesting, since one generally expects a kind of transformation to occur between the "molecular" and "crystal" regimes. Moreover, for gold and other supported clusters, this is the range where most of the physics has been demonstrated.

In practice, studying atomic structure and dynamics of such relatively large aggregates would be easy if empirical interatomic potentials could be used. However, apart from the case of rare gases [177,178] and alkali-halides [179], only few attempts have been made to apply empirical potentials to covalent (silicon, germanium) [180] and metal [181] clusters. The reason is of course that a two-body potential is not expected to work in these cases, very much for the same reasons outlined in Chapter 1. Based on that reasoning, one is led to expect a large improvement by the use of a many-body force scheme, like the glue model.

In this Chapter we present a first qualitative study of structure and energetics of gold clusters in the size range $100 < N < 1000$ based on the glue Hamiltonian [182].

6.2 Cuboctahedra, icosahedra and decahedra

Particular geometrical shapes have been suggested as the equilibrium geometries for small atomic aggregates since a long time.

As thoroughly discussed by Ino [164] and later by Howie and Marks [165], shapes which are expected to be particularly favoured on energetic grounds are the cuboctahedron (i.e., octahedron with truncated corners), the icosahedron and the decahedron. These polyhedra are shown in Fig. 6.1.

Cuboctahedral particles. In cuboctahedral particles (Fig. 6.1a), all atoms occupy perfect f.c.c. sites. In most solids, $\sigma_{111} < \sigma_{100} < \sigma_{110} < \ldots$. If, in particular, $\sigma_{110} > \sqrt{3/2}\sigma_{111}$, the cuboctahedron minimizes the total surface energy $\int \sigma \, dS$, and is therefore the favoured shape accordingly to the Wulff theorem. Such a particle has only (111) and (100) faces. Of course, the relative amplitude of (100) and (111) areas is related to the $\sigma_{111}/\sigma_{100}$ ratio.

Icosahedral particles. Icosahedral particles (Fig. 6.1b) are constitu-

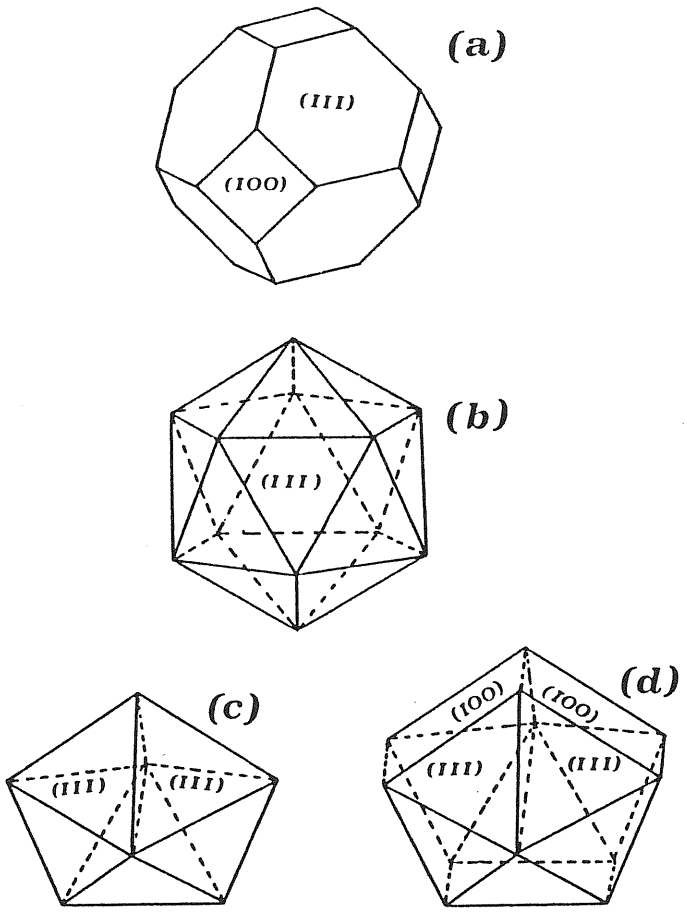

Figure 6.1:
Geometrical shapes particularly favoured by the Wulff theorem. (a) cuboctahedron; (b) icosahedron; (c) decahedron; (d) decahedron with five (100) extra faces.

ted by 20 tetrahedral twins (with (111) facets) arranged symmetrically. For this reason they are also called, together with the decahedral particles described below, *multiply-twinned particles* (MTPs). Only (111) faces are exposed, thus reducing the total surface energy. On the other hand, such a structure is not space filling, so that the interior must be strained. A certain amount of elastic energy will be associated to this strain.

Decahedral particles. Decahedral MTPs (Fig. 6.1c) are constituted by 5 tetrahedral twins (with (111) facets) arranged symmetrically. Although only (111) faces are exposed, the total surface energy is not as good as in the icosahedron, because the shape is quite far from the spherical shape, and therefore the total area is large. A better shape, if σ_{100} is not exceedingly large, is that shown in Fig. 6.1d, where a "ring" of five (100) faces is present. This is called by Ino a "D-Wulff-polyhedron" [164]. In the remainder, somewhat improperly, we shall refer to it as a "decahedron". Like the cuboctahedron, the size of the (100) faces with respect to the (111) faces depend on the $\sigma_{111}/\sigma_{100}$ ratio; and like the icosahedron, this structure must be strained to fill the space, with an elastic energy associated to the deformation.

It follows from these descriptions that a transition between MTPs and cuboctahedra should be expected to occur at a certain critical size N^*. For $N < N^*$, the energy is dominated by surface effects, and MTPs are favoured by their large (111) facets and small area. For $N > N^*$, however, the total elastic strain energy becomes so large as to make convenient the cuboctahedral arrangement, where the total surface energy is larger but there is no internal strain.

This approach is rather crude, being based only on macroscopic concepts (surface energy and elasticity theory). Its validity for small clusters is therefore questionable. However, its simple outcome is useful to interpret experimental results.

In the simple case of rare gas clusters, experiments and MD simulations suggest a transition between icosahedral and cuboctahedral struc-

tures around $N^* = 750$ [177].

For metal clusters, the situation is somewhat less clear. For example, the existence of very small ($N = 55$) cuboctahedral clusters is reported for Au [157] and Cu [183]. At the same time, multiply-twinned particles of gold are observed for sizes up to $N \sim 10000$ [156]. In the case of small particles, however, the influence of the substrate (or of the molecular matrix in which the cluster is embedded) on the structure is not known. Large particles, on the other hand, may be out of thermodynamic equilibrium.

In a recent electron microscopy experiment, Iijima and Ichihashi observe a gold particle, consisting of about 459 atoms, which continually changes its shape under electron-beam irradiation [158]. Among the various shapes, cuboctahedra and icosahedra are clearly distinguishable. Moreover, amorphous clusters are also occasionally observed [159]. Although the clusters are not in equilibrium owing to the intense electron beam, these experiments make the $100 < N < 1000$ range particularly attractive for a theoretical investigation.

Finally, it should be mentioned that a tight-binding based calculation of platinum clusters indicates a critical size $N^* \sim 200$ for the transition between icosahedral and cuboctahedral structure [174].

6.3 Method

A structural investigation of free gold clusters, with particular emphasis on the geometrical shapes described in the previous Section, has been carried out within the glue model framework. The method used for this study is based on a molecular dynamics (MD) annealing strategy very similar to that previously employed for our surface studies.

As in that case, we must live with two very basic handicaps. The first is that for a fixed atom number, well above 10 and below 10000, one can generally expect an extremely large number of configurations which are energetically nearly equivalent [184], many more so than for a surface situation, where periodicity along the xy plane helps to reduce their

number. The second handicap—present also for surfaces—is that MD works with a constant particle number which makes the search for the "best" cluster geometries very clumsy and essentially impossible to carry out systematically. Within the limits posed by these two handicaps, we have found that our scheme provides interesting new insight and understanding, as will be shown below.

Several different annealing methods have been used:

- *Simple relaxation (SR).* Starting from some initial configuration, a damped MD run is performed, where kinetic energy is continuously extracted from the system by a factor $\alpha < 1$ at each time step. This quickly brings the system in a local energy minimum. The number of time steps required depends on α, but a number in the range 2000–5000 is quite typical. This procedure is analogous to a steepest-descent minimization, though a limited choice between nearby local minima might be allowed. The *SR* procedure is often used by starting from highly symmetric initial conditions (i.e., a "perfect" polyhedron), and, frequently, this initial symmetry is preserved. *SR* consumes little computer resources, but, at least in our case, it rarely finds the true, absolute energy minimum.

- *Low-temperature annealing (LA).* In this procedure, the system is equilibrated at a temperature T of the order of 0.2–$0.3\,T_m$, where T_m is the melting temperature of *bulk* Au, then T is gradually decreased to 0. This procedure allows moderate atomic rearrangements to take place (especially at the surface), while extensive structural reorganizations cannot occur. The final energy is usually lower than that obtained by *SR*. The total length of the cycle, however, must be larger (of the order of 10000 time steps, or 10^{-8} s).

- *Medium-temperature annealing (MA).* As above, but the equilibration temperature is in the range 0.5–$0.7\,T_m$, and the total simulation time is also larger (20000–50000 steps). This method is of use in cases where large reorganization must occur.

- *High-temperature annealing (HA).* In this case, the system is brought at $T > T_m$ and melted. Then, the temperature is very slowly decreased back to zero. The cycle length may reach 100000 steps or more ($\sim 10^{-9}$ s). Except in the case of very small ($N < 60$) clusters, where the reliability of our potential is questionable, this procedure is not able to re-crystallize the melt. In fact, the time scale of the MD simulation is not sufficient for the purpose. Therefore, the final result is always a reasonably optimized amorphous structure. As will be shown below, these amorphous structures are often very competitive in energy with crystalline structures, and exhibit interesting features.

None of these methods can be classified as the "best". Rather, each of them constitutes a useful tool to apply when appropriate.

As will be detailed below, we have found that the atomic arrangement at the cluster surface is very important in determining the final total energy. Optimal or quasi-optimal arrangements are often quite far from the geometrical positions set at the beginning, so that, to improve the energy, surface atoms should be able to migrate for relatively long distances. Such migrations require relatively high temperatures ($\sim 0.8\,T_m$), which often lead also to disordering of the "bulk" part of the cluster. In this case, the cluster becomes amorphous, and its energy increases.

To overcome this problem, we have sometimes adopted a strategy in which only the atoms in the external shell are allowed to move, while the internal atoms are kept frozen in their crystalline arrangement. In detail, this strategy, that we shall call high-temperature surface annealing *(HSA)*, is performed as follows:

1. Starting from some initial (and often quite arbitrary, e.g. in the choice of the lattice parameter) configuration, a *SR* procedure is performed. This allows large relaxation effects to occur, like the contraction of the whole cluster, or surface relaxations. The symmetry, on the other hand, is not substantially altered.

2. At the end of *SR*, the internal atoms are frozen in their positions.

3. An *HA* cycle is performed. The external atomic shell is "melted", and then slowly cooled on the crystalline substrate provided by the frozen atoms.

4. When the temperature reaches zero, the frozen atoms are released, and allowed to move again.

5. Finally, a new *SR* procedure is performed with all the atoms allowed to move. This relieves the cluster of strains due to the new surface arrangement, and further reduces the total energy.

This procedure almost always leads to better results than all the other methods listed above. It also selects the type of cluster geometry (cuboctahedron, etc.) at the outset.

Finally, we make some considerations on the energetic comparison of two different clusters. Let us consider two clusters C_1 and C_2, with respectively N_1 and N_2 atoms, and average ($T = 0$) energies *per atom* ϵ_1 and ϵ_2. If $N_1 < N_2$, it is also likely $\epsilon_1 > \epsilon_2$. This is simply due to the proportionally larger number of surface atoms in the smaller cluster C_1. This surface energy contribution is, in a sense, trivial, and has to be removed for the effective comparison of different structures when N is not the same. It can be subtracted by writing the total energy of the cluster as

$$N\epsilon = N\epsilon^* + 4\pi R^2\sigma \tag{6.1}$$

where R is the average cluster radius and σ the average surface energy per unit area. What we have called ϵ^* is the "effective" energy per atom, and it is what we shall use for comparison purposes.

Of course, R could be directly estimated for each cluster. Somewhat roughly, we shall instead assume that the cluster has a spherical shape, whose volume is that occupied by the same number of atoms N in a bulk f.c.c. crystal:

$$\frac{4}{3}\pi R^3 = \frac{N a_0^3}{4} \tag{6.2}$$

Substitution in (6.1) then gives

$$\epsilon^* = \epsilon - \left(\frac{16\pi\sqrt{3}}{N}\right)^{1/3} \frac{\sqrt{3}a_0^2\sigma}{4} \tag{6.3}$$

By assuming a value for σ, we use this equation to compute the "effective" energy per atom ϵ^* [1]. We have taken $\sigma = 96.6\,\mathrm{meV/\AA^2}$, which is the surface energy of a non-reconstructed (111) surface (see Table 4.4, page 103).

6.4 Results

Due to the intrinsic limitations outlined in the previous Section, our MD study of clusters has been restricted to a very restricted set of situations, namely:

- Clusters without a crystalline germ. High-temperature annealing invariably leads to amorphous structures. Here a precise choice of N is not critical.
- Clusters growing from f.c.c., icosahedral or decahedral germs, leading to "crystalline" structures. Here, the choice of N is often critical (e.g., complete shells lead to more symmetrical arrangements).

In both cases, only a few values of N have been investigated, in the size region $100 < N < 1000$. The results for amorphous, cuboctahedral, icosahedral and decahedral clusters are discussed in the four following Subsections. A brief mention to the results for $N < 100$ is made in the last Subsection.

6.4.1 Amorphous clusters

As described in the previous Section, a high-temperature annealing procedure (*HA*), where the cluster is first melted, and then gradually cooled down to $T = 0$, always leads to an amorphous final structure. We discuss first these amorphous clusters, since they provide a good reference point against which the other structures can be compared. Moreover, their surfaces exhibit interesting (111)-faceting effects.

Table 6.1 reports the final energies per atom for amorphous clusters

[1] Of course, (6.3) could also be used in the opposite way: given a value for ϵ^* (for example, the cohesive energy), an effective surface energy σ can be computed.

N	ϵ	ϵ^*
116	−3.1072	−3.7370
201	−3.2142	−3.7386
314	−3.2857	−3.7376
459	−3.3434	−3.7416
640	−3.3775	−3.7339
861	−3.4101	−3.7330

Table 6.1:
Energies ϵ, and effective energies ϵ^* (in eV/atom), of amorphous clusters at $T = 0$, after high-temperature annealing (HA).

with $N = 116, 201, 314, 459, 640, 861$. This sequence is that of ideal cuboctahedra with 3×3 (100) facets, as described in the next Subsection. However, even if cuboctahedra were chosen, somewhat arbitrarily, as the starting point for the annealing procedure, the final amorphous configuration seems to retain no memory of this initial state.

It is interesting to note that ϵ^* is nearly constant across the sequence. This indicates that a spherical droplet model is quite adequate for these clusters, and also that the value we have chosen for σ (see Eq. (6.3)) is rather realistic. The average value for ϵ^*, $\epsilon^*_a = -3.737$ eV/atom, can be assumed as the average effective energy of an amorphous cluster, regardless of its size. This can be compared with the crystalline cohesive energy at $T = 0$, $\epsilon_c = -3.78$ eV/atom, and with the $T = 0$ extrapolation of the energy of the supercooled bulk liquid (from Table 3.1, page 52) $\epsilon_a = -3.70$ eV/atom.

Visual inspection also gives valuable informations. Figure 6.2 shows the clusters with $N = 201, 459$ and 861 at $T = 0$ after the HA procedure. Although the global shape is ball-like as expected, the surface layer is extremely well packed. Except for a few defects, it has locally a (111)-like, triangular lattice appearance.

Figure 6.3 shows the $N = 861$ cluster at $T = 0$, and a snapshot of the same cluster at $T = 1380$ K (above the bulk melting temperature). In

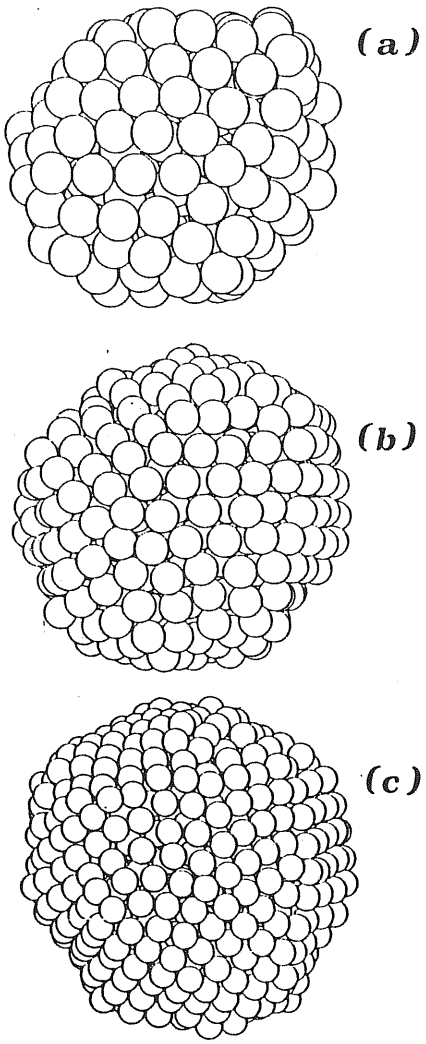

Figure 6.2:

Final $T = 0$ amorphous structures, after a high-temperature annealing, of clusters with $N = 201$ (a), 459 (b) and 861 (c). Surfaces are always well packed and tend to form (111)-like facets.

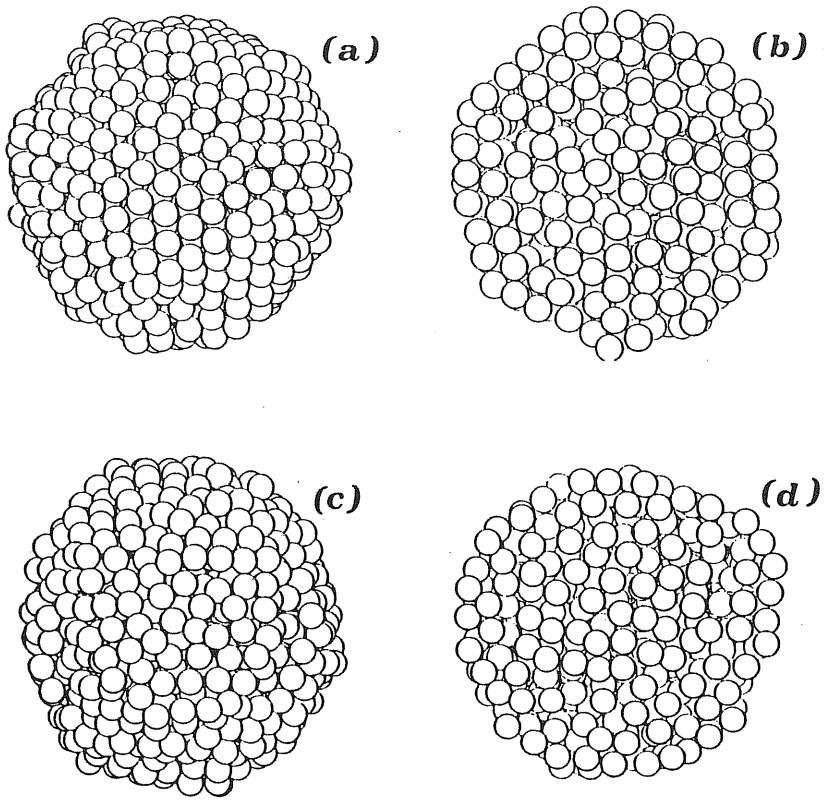

Figure 6.3:
Amorphous cluster with $N = 861$. (a) $T = 0$, overall view. (b) $T = 0$, internal view. The cluster has been cut along a plane passing through its center. (c) and (d) are the same as (a) and (b), but represent snapshots (instantaneous positions) at $T = 1380\,\mathrm{K}$, where the cluster is liquid.

the latter case, the diffusion coefficient and other thermodynamic data indicate that the cluster is indeed liquid. However, it can be seen that faceting and high surface packing are still present to some extent. This gives further support to the results on the non-melting behaviour of the Au(111) surface studied in Chapter 5. It can be also seen from Fig. 6.3 that the cluster is internally disordered, although the atomic layers near the surface are kept somewhat ordered by the highly-packed surfaces.

Amorphous gold clusters are sometimes observed in electron microscope experiments [159].

6.4.2 Cuboctahedral clusters

As discussed in Sec. 6.2, f.c.c.-cuboctahedra are octahedra with eight (111) faces, whose vertices are cut by six (100) faces. They are constructed by putting all atoms in f.c.c. crystal sites. The total (111) area, owing to the lower surface energy, is expected to be larger than the total (100) area. For this reason, only cuboctahedra with relatively small (100) faces have been investigated. In particular, the following families have been considered:

- *True octahedra.* (100) facets are absent. An octahedron with n shells is obtained from the octahedron with $n-1$ shells, by adding $(n+1)^2 + n^2$ atoms. This gives rise to the sequence $N = 6$, 19, 44, 85, 146, 231, 344, 489, 670, 891, ...

- *Cuboctahedra with* 2×2 *(100) facets.* Obtained from the octahedra by removing the six "tip" atoms. Their sequence is $N = \ldots$, 79, 140, 225, 338, 483, 664, 885, ...

- *Cuboctahedra with* 3×3 *(100) facets.* Obtained by further removal of six 2×2 atomic squares (24 atoms). Their sequence is $N = \ldots$, 55, 116, 201, 314, 459, 640, 861, ...

Odd N systems have an atom in the center, while even N systems have an interstitial site in the center.

	N	SR		LA	
		ϵ	ϵ^*	ϵ	ϵ^*
Octahedra	146	−3.1093	−3.6926	−3.1461	−3.7294
	231	−3.2055	−3.7061	−3.2284	−3.7290
	344	−3.2818	−3.7202	−3.2990	−3.7374
	489	−3.3395	−3.7294	−3.3526	−3.7425
	670	−3.3853	−3.7363	−3.3954	−3.7464
	891	−3.4224	−3.7416	−3.4302	−3.7494
2×2 *(100)*	140	−3.1003	−3.6918	−3.1383	−3.7298
	225	−3.2032	−3.7082	−3.2254	−3.7304
	338	−3.2782	−3.7192	−3.2978	−3.7388
	483	−3.3363	−3.7278	−3.3524	−3.7439
	664	−3.3820	−3.7341	−3.3954	−3.7475
	885	−3.4193	−3.7392	−3.4303	−3.7502
3×3 *(100)*	116	−3.0075	−3.6373	−3.1056	−3.7354
	201	−3.1746	−3.6990	−3.2135	−3.7379
	314	−3.2744	−3.7263	−3.2896	−3.7415
	459	−3.3405	−3.7387	−3.3440	−3.7422
	640	−3.3899	−3.7463	−3.3927	−3.7491
	861	−3.4279	−3.7508	−3.4301	−3.7530

Table 6.2:

Energies ϵ, and effective energies ϵ^* (in eV/atom), of cuboctahedral clusters at $T = 0$.

The results of simple relaxations and of low-temperature annealing runs are reported in Table 6.2. Several observations on these results can be made:

- The group of cuboctahedra with 3×3 (100) facets is slightly favoured over the others. For this reason, we shall refer mainly to this group in the following.

- *LA* invariably leads to a better energy than *SR*. This confirms that the optimization problem is not trivial in this case. The symmetry is often reduced by the finite-temperature annealing; the arrangement of surface atoms changes considerably.

- By using *SR*, all clusters with $N < 400$ have energies which lie *above* the energy of amorphous clusters, $\epsilon_a^* = -3.737$ eV/atom. This suggests that the starting point provided by the perfect, "crystalline" structures is indeed quite bad for such small sizes.

- *LA* apparently solves this problem. However, an examination of the systems with $N = 116$ and 201 (and also $N = 140, 146$) shows that their structure has become amorphous or quasi-amorphous. That is, for such small systems, the temperature reached in the annealing run (around 300 K) is sufficient to "melt" them. This is not of course a real melting, since the energy decreases in the transition. It simply indicates an unstable starting configuration, whose energy is higher than that of a well-annealed amorphous structure. Other crystalline structures with energies lower than the amorphous structures may, of course, exist.

- Clusters with N in the range 300–500 remain crystalline after *LA*, but their energetic improvement over the amorphous structures is extremely small (less than 5 meV/atom). Only for $N > 500$ cuboctahedra become clearly favoured.

- The competition between crystalline and amorphous structures seems basically due to the fact that amorphous clusters have a better surface energetics. For example, in the case $N = 459$,

the average energies of bulk and surface atoms, calculated using (1.12), are respectively $\epsilon_b \simeq -3.68\,\text{eV}$, $\epsilon_s \simeq -3.02\,\text{eV}$ in the crystalline cluster, and $\epsilon_b \simeq -3.61\,\text{eV}$, $\epsilon_s \simeq -3.09\,\text{eV}$ in the amorphous cluster. Here, bulk energies are better in the crystalline cluster, but surface energies are better in the amorphous. Since for this size the number of surface atoms nearly equals the number of bulk atoms, the total cluster energies are very close.

As usual, visual examination of the clusters provides some further insight. Figure 6.4 shows the cuboctahedra with $N = 201$ and 861 after the *SR* and *LA* procedures. In all cases, rounding of edges and a strong contraction of the (100) faces are clearly visible. For $N = 861$, the configurations after *SR* and *LA* are almost identical, and have very similar energies. For $N = 201$, on the other hand, *LA* gives a rather disordered cluster, while the original crystalline structure is retained by *SR*. This disordering might be attributed to the bad energetics of surface atoms in the initial configuration. This gives rise to forces which push the atoms towards more favourable positions. In small clusters, surface atoms are the majority and these forces are sufficient to destroy the crystalline order of the interior part.

In an attempt to overcome this problem, we have applied the high-temperature surface annealing procedure *HSA* described in Sec. 6.3, on cuboctahedra with $N = 201(79), 459(201), 861(459)$. Here, the presence of a rigid crystalline core prevents "catastrophic" rearrangements. The number in parenthesis indicates the size of the rigid core. The results are reported in Table 6.3. With the exception of $N = 201$, whose energy is nearly identical to that of the amorphous clusters obtained by *LA* (Table 6.2) or *HA* (Table 6.1), the energies display a clear improvement.

Figure 6.5 shows a global view and the atomic arrangement in one of the (100) planes passing through the center of the cluster for the case $N = 459$. Observation of this picture leads to the following points:

- Atom rearrangement occurred in a non-symmetric way.
- Surface relaxations are very strong, both in the radial and tangential direction.

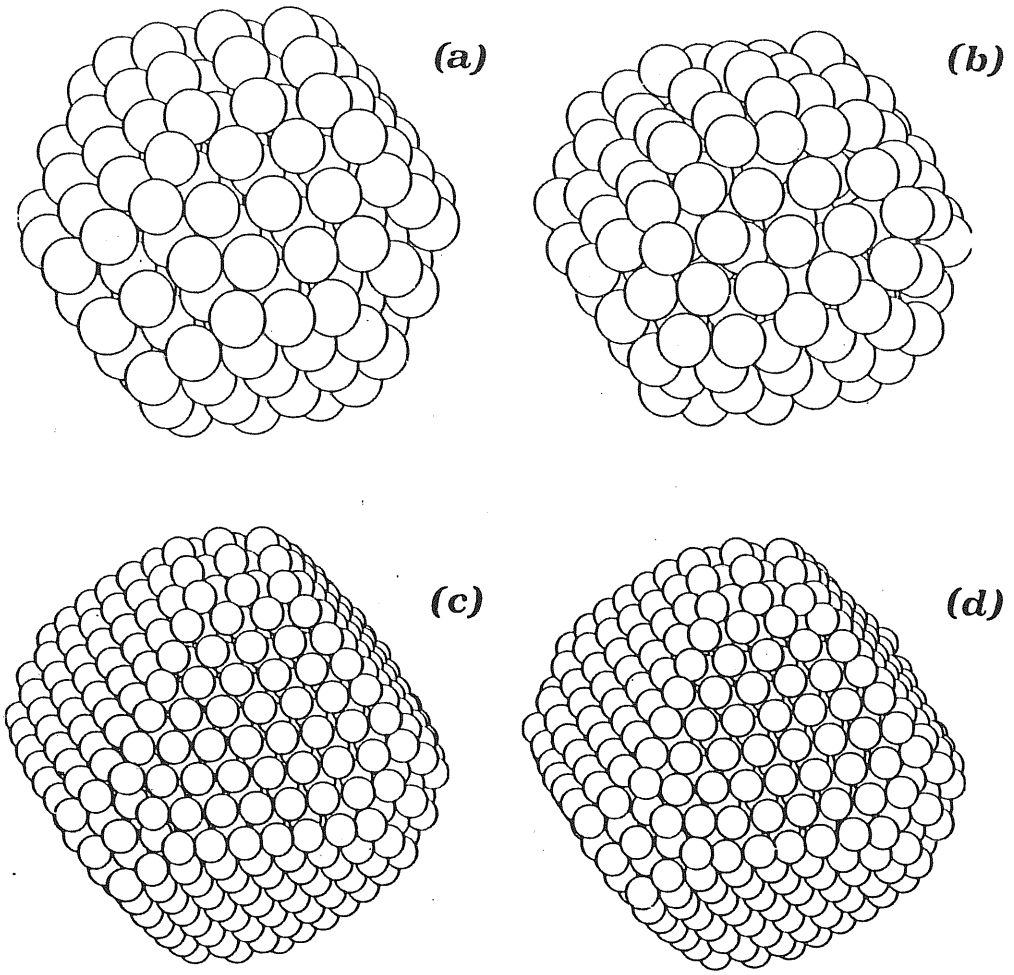

Figure 6.4:
$T = 0$ structures of cuboctahedral clusters: $N = 201$ after SR (a) and LA (b), $N = 861$ after SR (c) and LA (d).

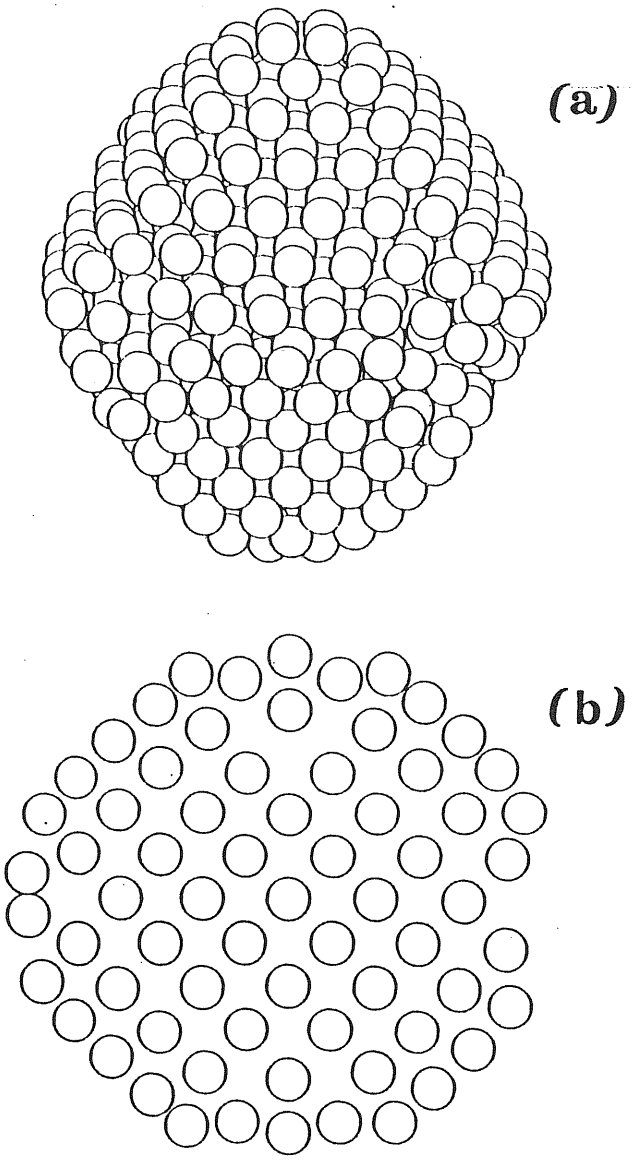

Figure 6.5:
$T = 0$ structure of a $N = 459$ cuboctahedral cluster after high-temperature surface annealing (*HSA*). Global view (a) and atomic structure of a plane passing through the center (b).

N	*SR*		*HSA*	
	ϵ	ϵ^*	ϵ	ϵ^*
201	−3.1746	−3.6990	−3.2138	−3.7382
459	−3.3405	−3.7387	−3.3528	−3.7510
861	−3.4279	−3.7508	−3.4364	−3.7593

Table 6.3:
Energies ϵ, and effective energies ϵ^* (in eV/atom), of cuboctahedral clusters with 3×3 (100) faces at $T = 0$. The two rightmost columns refer to a high-temperature surface annealing (*HSA*) procedure.

- (111) faces tend to shrink laterally, while (100) faces tend to open up laterally, probably being "pulled apart" by neighbouring (111) faces.

- A square of 2×2 atoms (instead of the initial 3×3) is often seen on top of the (100) faces. However, the central atom in the 3×3 "second layer" square is missing, so that the 2×2 square can heavily subside into the vacant hole. This also allows the (111) faces to shrink.

The last point suggest that a new family of cuboctahedra, i.e. with 2×2 (100) faces and the central atom missing in the 3×3 square below, could be a favourable geometry. We have tried three such systems, with $N = 219(79), 477(225), 879(483)$. The results are reported in Table 6.4. $N = 477$ and $N = 879$ are unique, in that *SR* and *HSA* yield the same result. As shown by Fig. 6.6, these clusters are symmetric and extremely stable. However, the somewhat defected $N = 459$ and $N = 861$ clusters reported in Table 6.3, have a (slightly) better energy.

6.4.3 Icosahedral clusters

The n-th atomic shell of an icosahedral particle has 12 vertices, each containing 1 atom; 30 edges, each containing $n - 1$ atoms; and 20 faces,

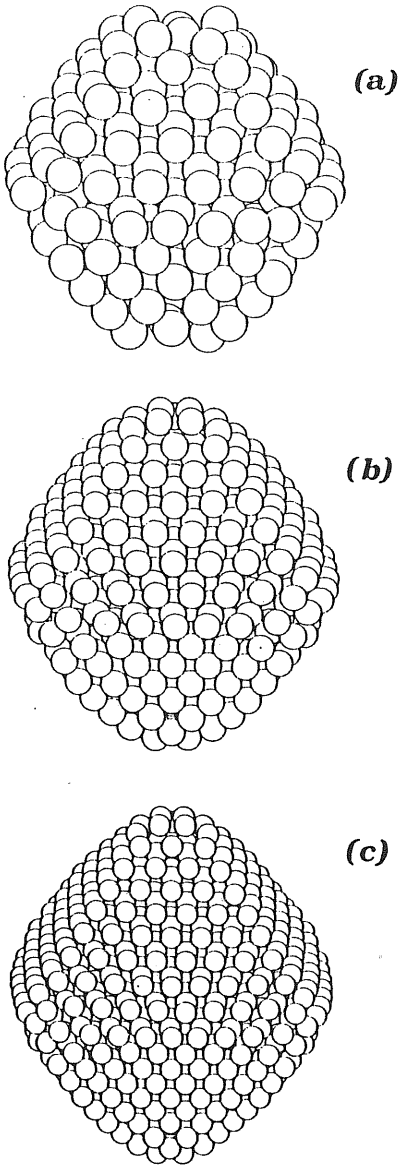

Figure 6.6:
$T = 0$ structures of $N = 219$ (a), $N = 477$ (b) and $N = 879$ (c) cuboctahedral clusters after high-temperature surface annealing (HSA).

N	SR		HSA	
	ϵ	ϵ^*	ϵ	ϵ^*
219	−3.2203	−3.7299	−3.2319	−3.7415
477	−3.3559	−3.7490	−3.3559	−3.7490
879	−3.4333	−3.7540	−3.4333	−3.7540

Table 6.4:

Energies ϵ, and effective energies ϵ^* (in eV/atom), of cuboctahedral clusters with 2×2 (100) faces, and the central atom missing in the 3×3 layers below, at $T = 0$. The two rightmost columns refer to a high-temperature surface annealing (HSA) procedure.

N	SR		LA		HSA	
	ϵ	ϵ^*	ϵ	ϵ^*	ϵ	ϵ^*
147	−3.0906	−3.6726	−3.1213	−3.7033	−3.1287	−3.7107
309	−3.2506	−3.7049	−3.2640	−3.7183	−3.2771	−3.7314
561	−3.3518	−3.7242	−3.3548	−3.7272	−3.3630	−3.7354

Table 6.5:

Energies ϵ and effective energies ϵ^* (in eV/atom) of icosahedral clusters at $T = 0$, using simple relaxation (SR), low-temperature annealing (LA) and high-temperature surface annealing (HSA) procedures.

each containing $(n-1)(n-2)/2$ atoms. The total number of atoms in the shell is therefore $S(n) = 12 + 30(n-1) + 10(n-1)(n-2)$, and therefore the total number of particles in icosahedra are given by $N(n) = 1 + \sum_{i=1}^{n} S(i) = 13, 55, 147, 309, 561, 923, \ldots$

Table 6.5 reports the results of SR, LA and HSA runs for $N =$ 147(55), 309(147) and 561(309). The numbers in parenthesis indicate the size of the rigid core. As in the case of cuboctahedra, the best results are obtained by HSA. All energies are higher than the cuboctahedra energies (Table 6.3), and also slightly higher than those of the amorphous

N	*HSA*	
	ϵ	ϵ^*
159	−3.1479	−3.7149
329	−3.2871	−3.7320
581	−3.3731	−3.7412

Table 6.6:
Energies ϵ and effective energies ϵ^* (in eV/atom) of icosahedral clusters at $T = 0$, using a *HSA* procedure. *SR* data are not reported, being not significant in this case (presence of adatoms).

clusters (Table 6.1). The energy differences, however, rarely exceed 20 meV/atom, with 10 meV/atom as a typical value.

The corresponding final configurations are shown in Fig. 6.7, where the atoms allowed to move have been put in evidence. It can be seen that surface atoms tend to shrink, forming "holes" on the cluster surface. This is basically the same phenomenon which occurs on the flat Au(111) surface, leading to surface reconstruction (see Sec. 4.5). In the case of cuboctahedral clusters, shrinking occurs at the expenses of (100) faces, which become broader. In icosahedra, all faces are initially equal, so that symmetry breaking and creation of defects are unavoidable consequences of shrinking.

Like in our surface studies, we attempted to improve the icosahedra energy by supplying more atoms on their surfaces (as adatoms) in the initial configurations. 12 atoms have been added to the smaller icosahedron, and 20 atoms (one per face) to the other two, producing clusters with N = 159, 329, 581. The results are reported in Table 6.6, and the final configurations are shown in Fig. 6.8. It can be seen that cluster surfaces are now well coated, but the energy improvement is rather small. Therefore, cuboctahedra remain favoured at all sizes over icosahedral particles. We see also from Table 6.6 that icosahedral clusters are better than amorphous for $N > 500$.

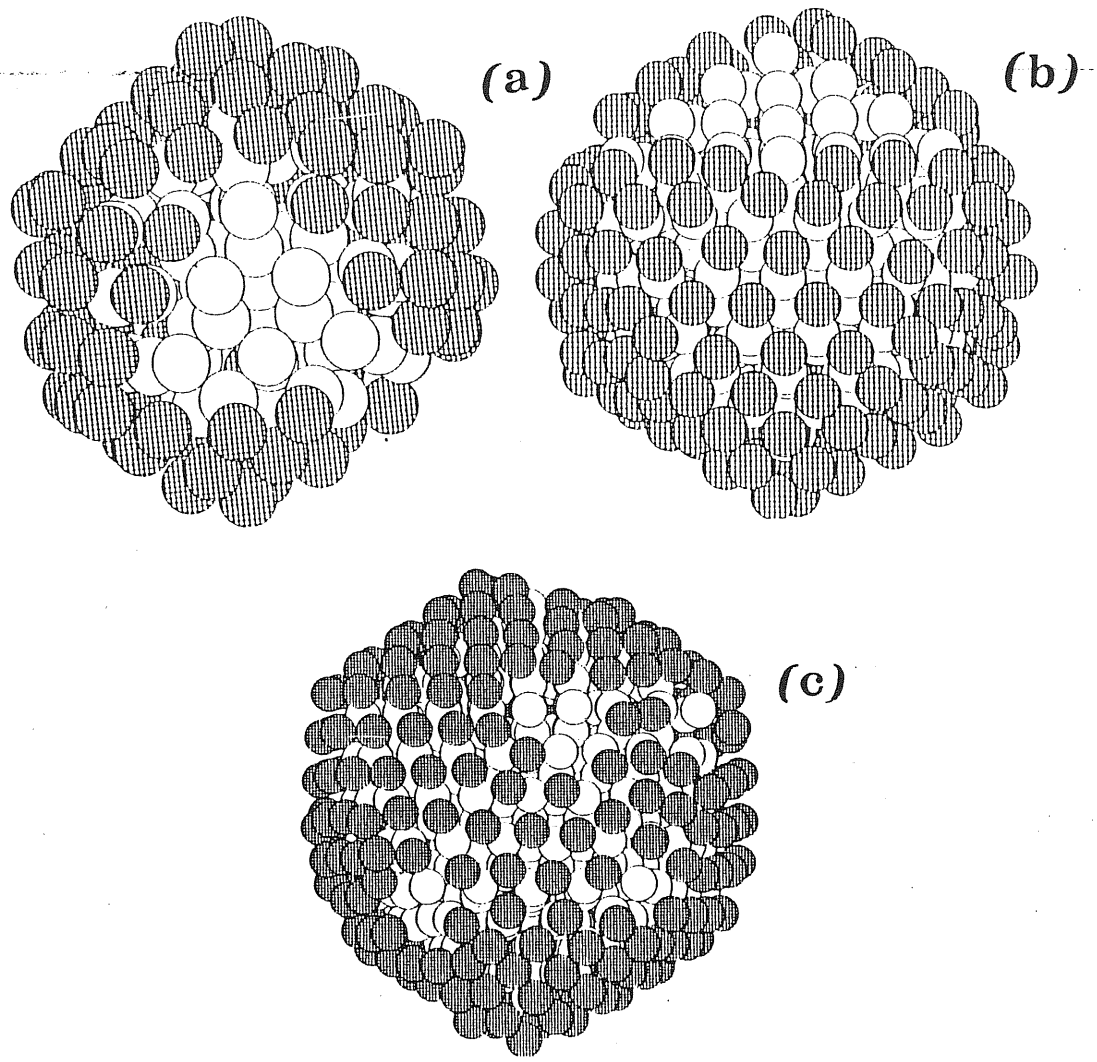

Figure 6.7:
$T = 0$ structures of $N = 147$ (a), $N = 309$ (b) and $N = 561$ (c) icosahedral clusters after high-temperature surface annealing (*HSA*). Shaded atoms were allowed to move during the annealing, all other atoms were kept fixed.

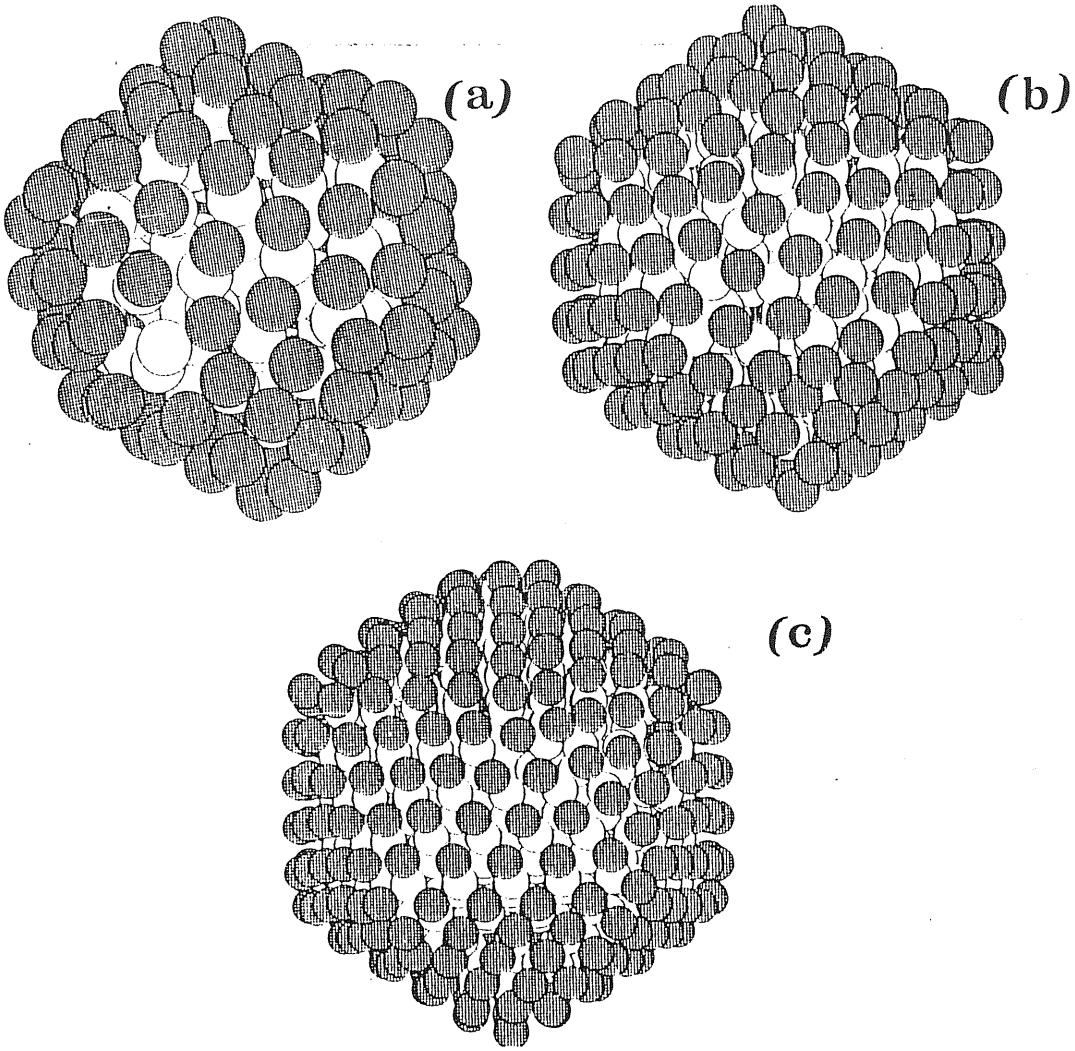

Figure 6.8:
$T = 0$ structures of $N = 159$ (a), $N = 329$ (b) and $N = 581$ (c) icosahedral clusters after high-temperature surface annealing (*HSA*). Shaded atoms were allowed to move during the annealing, all other atoms were kept fixed.

N	t	h	*SR*		*LA*		*HSA*	
			ϵ	ϵ^*	ϵ	ϵ^*	ϵ	ϵ^*
258	5	4	−3.1918	−3.6743	−3.2493	−3.7318	−3.2513	−3.7338
409	6	4	−3.2841	−3.6979	−3.3085	−3.7223		
605	7	4	−3.3501	−3.7133	−3.3700	−3.7332		
711	7	5	−3.3636	−3.7077	−3.3915	−3.7356	−3.4066	−3.7507
992	8	5	−3.4123	−3.7203	−3.4347	−3.7427		

Table 6.7:
Energies ϵ and effective energies ϵ^* (in eV/atom) of decahedral clusters at $T = 0$, using simple relaxation (*SR*), low-temperature annealing (*LA*) and high-temperature surface annealing (*HSA*) procedures.

6.4.4 Decahedral clusters

As discussed in Sec. 6.2, decahedra have ten (111) triangular facets with t atoms per side, and five (100) rectangular facets containing $t \times h$ atoms. The lengths t and h are controlled by the ratio $\sigma_{111}/\sigma_{100}$, in order to minimize the total free energy at constant volume accordingly to the Wulff theorem [164]. We have chosen $\sigma_{111}/\sigma_{100} = 88.1/102.2 = 0.862$ (using our values for reconstructed surfaces found in Chapter 4).

The results for the decahedra we have studied are reported in Table 6.7. The energies are only marginally poorer than those of cuboctahedra.

Figure 6.9 shows the configurations of the $N = 258$ and $N = 711$ decahedral clusters after the *HSA* procedure. Again, surface atoms tend to shrink and holes appear on the external shell. A remarkable feature is the triangular structure that (100) faces tend to assume (Fig. 6.9b). This suggest that the (100) ring around the decahedral particle might be reconstructed like the flat Au(100) surface (see Sec. 4.3). The $h = 5$ height of these faces in our $N = 711$ and $N = 992$ clusters seems ideal to accommodate one extra row, in order to give rise to the six-over-five stacking, characteristic of the Au(100) reconstruction. Such reconstruction could bring the energy of these decahedral clusters near

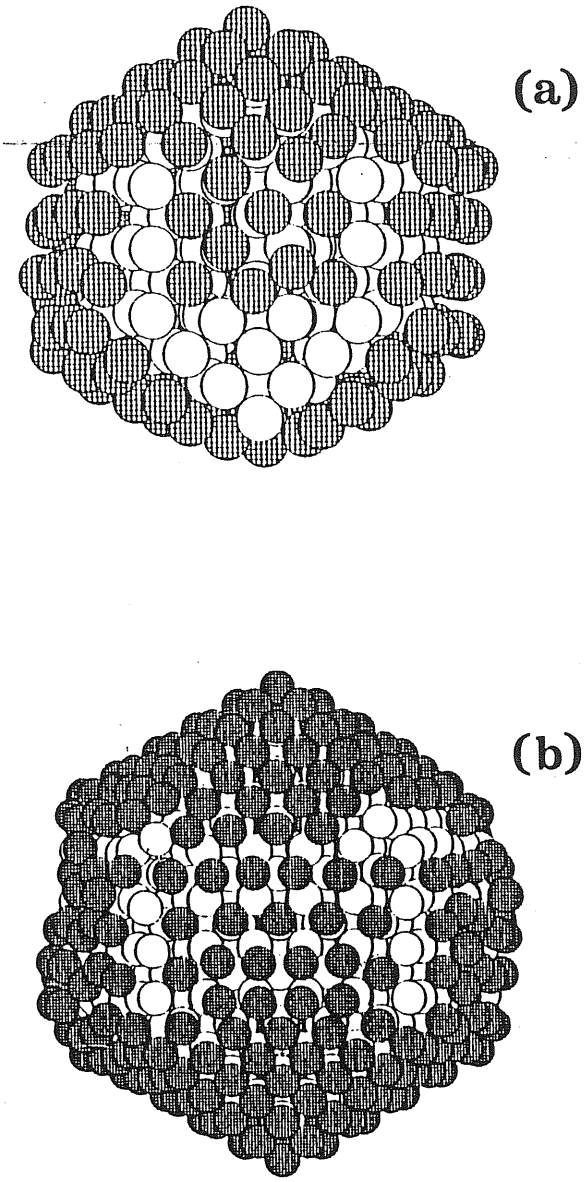

Figure 6.9:
$T = 0$ structures of $N = 258$ (a) and $N = 711$ (b) decahedral clusters after high-temperature surface annealing (HSA). Shaded atoms were allowed to move during the annealing, all other atoms were kept fixed.

or below that of cuboctahedra. We are presently extending our study in this direction. Interestingly, decahedra with $N \sim 1000$ are often observed in electron microscopy, while smaller decahedra rarely appear [159].

Overall, we find here that decahedra are only marginally higher in energy than cuboctahedra, and might be favoured when N does not a cuboctahedron. In particular, decahedra appear to be more favourable than either icosahedra and amorphous for $500 < N < 1000$.

6.4.5 Very small clusters ($N < 100$)

In clusters with $N < 100$, the number of "surface" atoms greatly exceeds the number of "bulk" atoms (if any atom at all can be regarded as such). Many of these "surface" atoms may have a very poor coordination, so that our potential, fitted in rather different physical situations, is not expected to give reliable results in this size region.

Moreover, "magic" numbers arising from closed-shell filling of cluster-sized orbitals, as seen by mass spectroscopy experiments [163], cannot of course be explained by a classical model like ours.

The atomic arrangements arising from simulated annealing MD runs of clusters with $N < 100$ are in fact rather odd and probably of little physical meaning. For $N < 60$, the minimal energy structures are elongated or disk-like. As an example, Fig. 6.10 shows a disk-like structure with $N = 28$. For $60 < N < 100$, amorphous aggregates are usually obtained, whose energy is appreciably lower than that of all the crystalline clusters of comparable size that we have tried.

A single exception, however, is worth mentioning. A stable, crystalline $N = 58$ cluster spontaneously appeared at the end of a *HA* procedure, *without* the use of a rigid core. This cluster, shown in Fig. 6.11, has a b.c.c.-like crystal structure, without the central atom, and with five shells containing respectively 8, 6, 12, 24, 8 atoms at distances 2.5, 3.5, 4.5, 4.8 and 5.4 Å from the center of the cluster. The average energy per atom is $\epsilon = -2.9791\,\mathrm{eV/atom}$, or $\epsilon^* = -3.7726\,\mathrm{eV/atom}$, which is remarkably good. Removal of the central atom from the $N = 59$ b.c.c.

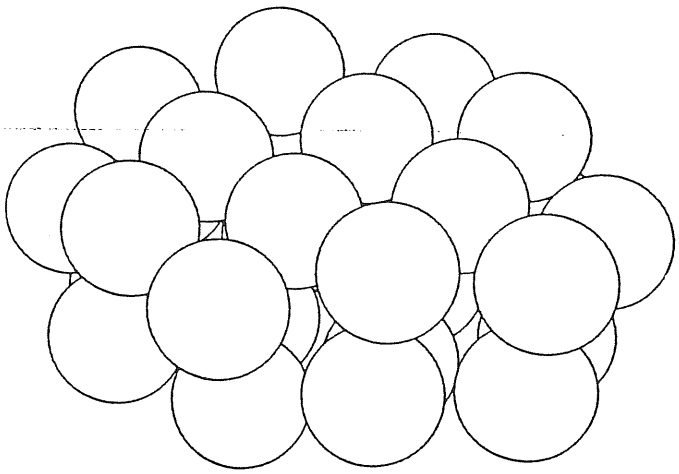

Figure 6.10:
$N = 28$ disk-like cluster.

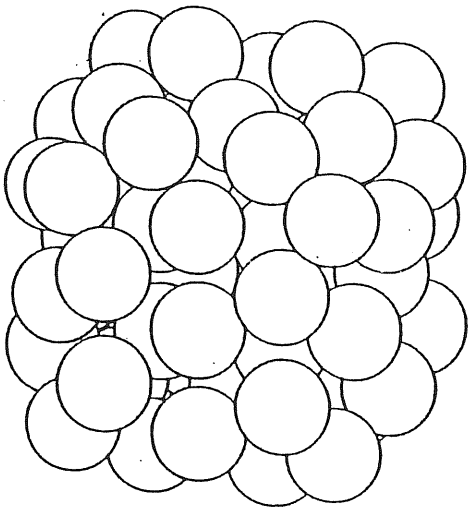

Figure 6.11:
$N = 58$ cluster with b.c.c. structure. The central atom is missing.

cluster allows a strong contraction to take place, reducing the energy. For an infinite bulk, the b.c.c. structure is unstable (and *not* metastable) in our model: relaxation effects related to its small size play a crucial role in the stability of this cluster.

For the reasons discussed above, the occurrence of this "magic" cluster should not be taken too seriously. It is interesting to note, however, that the $N = 59$ b.c.c. structure is a good candidate for explaining the EXAFS results of Montano *et al.* on Cu microclusters [183], as close examination of their Table I suggests.

6.5 Clusters: summary

The main results of this study can perhaps be condensed as follows.

- Rather *different* cluster structures, such as f.c.c.-cuboctahedra, decahedra and icosahedra, all yield very *similar* energies, with typical differences of the order of 0.2% at $N \sim 500$ between one and another.

- The lowest energies are obtained by heavily distorted cuboctahedra. Decahedra and icosahedra appear to be higher in energy (the latter being the worst), but the differences are small, generally in the order of 10–20 meV/atom. The $T = 0$ energetics is summarized in Fig. 6.12. In presence of thermal and electronic excitation, all these structures should become observable, which is experimentally confirmed.

- Surfaces exhibit a tendency to reconstruct. In cuboctahedra, the interatomic spacing within (111) faces tends to shrink. In icosahedra and decahedra, small improvements in the total energy may be obtained if the surface density is made higher by addition of extra atoms.

- There is always a "non-crystalline" state of the cluster, whose interior looks amorphous and whose surface structure reminds one of

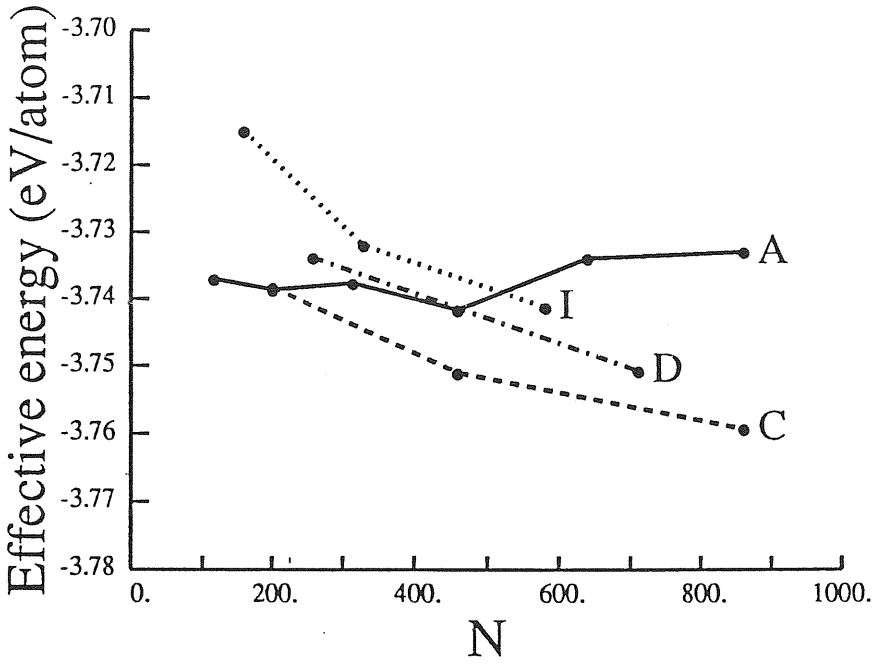

Figure 6.12:

Effective energies per atom ϵ^* (defined by Eq. (6.3)) at $T = 0$ as a function of the number of atoms N. **A** are amorphous, **I** icosahedral, **D** decahedral, and **C** f.c.c.-cuboctahedral clusters. The points represent the results of high-temperature annealing runs, with all atoms free to move (**A**), or with frozen crystalline germs (**I**, **D**, **C**). The lines connecting the points are provided only for visual convenience. $\epsilon_c = -3.78$ eV is the bulk crystalline cohesive energy, $\epsilon_a = -3.70$ eV is the $T = 0$ extrapolation of the energy of the supercooled bulk liquid.

somewhat rounded (111) crystal facets. Its energy is very close to the best crystalline cuboctahedral state. Starting with $N \gg 200$, the smaller the cluster, the closer the amorphous and crystalline energies are, until they merge for $N \sim 200$. The amorphous state becomes favoured at small sizes because of its lower total surface energy.

- The stable crystalline cluster structures are not trivial to obtain from the MD annealing procedure. They require a rather articulate strategy based on starting from a smaller crystalline germ, annealing the outermost shell of added atoms, and then relaxing the whole system. Simple high-temperature annealing done without these precautions usually leads irreversibly to an amorphous cluster.

This study is currently in progress, and an investigation of the melting properties as a function of size is being planned.

Chapter 7

Conclusions

The glue model is a novel empirical way to represent atomic interactions in a metallic system. As discussed in Chapter 1, the main difficulties associated with the use of two-body descriptions in metals are overcome without introducing a new significant computational overhead. Therefore, the model is particularly well suited to molecular dynamics or Monte Carlo computer simulations.

It has been shown that the glue Hamiltonian provides for a good unified description of bulk, defect and surface properties of gold. In particular, it is successful in predicting the occurrence of reconstruction on all its low index surfaces. Reconstructions arise from the tendency to increase surface coordination, induced by the glue forces. A highly detailed picture of all reconstructed gold surfaces has been obtained, which in several cases has a direct experimental confirmation.

The method of using computer simulation as part of the fitting procedure allows to model quite accurately also the thermal behaviour, so that realistic computer simulation studies of metal surfaces and defects at finite temperature are also feasible. In a first study of the melting behaviour of the Au(111) surface, we have found that surface melting does not occur on reconstructed Au(111), as a consequence of the good energetics of surface atoms and of the surface stiffening arising from the first-layer contraction.

The success in reproducing surface properties encouraged us to apply

the model also to small clusters of atoms, where surface forces presumably play a crucial role in determining the structure. We find that this is confirmed, and in particular that denser (or "reconstructed") surface layers quite often yield a better energetics. Generally, we find cuboctahedra to be energetically favoured. However, amorphous clusters of high stability are also uncovered, which for $N < 200$ become favoured over clusters with a "crystalline" structure.

On the negative side, the glue Hamiltonian has some intrinsic limitations. The lack of true angular forces, in particular, prevents a good fit of the phonon dispersion curves, which basically remain determined by the two-body part. For the same reason, the stacking-energy difference between the f.c.c. and h.c.p. crystal structures is zero in our simple first-neighbour scheme. Like for two-body forces, interactions extending at least to third neighbours would be required for a realistic description of these aspects.

Such an extension is of course possible, but has not been attempted here. It remains to be considered for the future, along with similar applications of many-body force schemes to other metals, as well as to non-elemental systems.

Appendix A

Glue forces in molecular dynamics

The purpose of this Appendix is to discuss some technical aspects of the molecular dynamics (MD) simulation program used to carry out the studies described in this thesis, with particular emphasis on the calculation of the glue forces.

A.1 The MD method

The molecular dynamics method for a classical system consists of following the time evolution of a N-particles system by numerical integration of Newton's equations of motion

$$\ddot{\vec{r}}_i = -\frac{1}{m_i}\vec{\nabla}_i V$$

where V is the total potential energy function (for a recent extensive survey on MD, see Ref. [55]).

From the phase space trajectory of the system obtained in this way, several statistical properties of the system may be obtained by time averaging. Moreover, MD may be effectively used as a tool for energy minimization, as discussed in Sec. 4.2 (page 66).

In MD calculations of bulk systems, the particles are enclosed in a box (usually a parallelepiped), and periodic boundary conditions (PBC)

are used to minimize boundary effects. PBC consist of repeating the computational box by rigid translation along the three directions parallel to the box edges, so that the whole space is filled. For surface studies, PBC are in effect only along directions parallel to the surface plane, whereas free conditions are used along the surface normal. This gives rise to a "slab" geometry, and care must be taken to define a number of atomic layers large enough to avoid excessive coupling between the two surfaces. This was not a serious problem in our case, where 10–20 layers always proved to be sufficient, owing to the short-range character of the functions in the glue Hamiltonian.

A.2 MD at constant volume

In the simplest version of the MD method, the box volume Ω is fixed, and the total energy E and number of particles N are conserved, meaning that the simulation is performed in the microcanonical or $E\Omega N$ ensemble.

For a system of identical particles interacting through the glue Hamiltonian, V is given by Eq. (1.5) and the equations of motion are

$$\ddot{\vec{r}}_i = -\frac{1}{m} \sum_{\substack{j=1 \\ (j\neq i)}}^{N} \left(\phi'(r_{ij}) + [U'(n_i) + U'(n_j)]\rho'(r_{ij})\right) \frac{\vec{r}_{ij}}{r_{ij}}$$

where $\vec{r}_{ij} = \vec{r}_i - \vec{r}_j$. Implementation of these equations in the simulation program requires to pass twice over all the interacting pairs. By "interacting pairs" we mean here all pairs of particles whose distance is less than $\max(r_c, r_m)$, where r_c is the range of $\phi(r)$ and r_m the range of $\rho(r)$. In the first pass, the two-body forces and the coordinations n_i are calculated for each particle. In the second pass, the glue forces are computed using the values for n_i previously obtained.

The algorithm is sketched in Table A.1. In the production program, the functions $\phi(r)$, $\rho(r)$ and $U(n)$, and the derivatives $-\phi'(r)/r$, $-\rho'(r)/r$ and $U'(n)$, are taken from numerical tables generated previously (once for all). To avoid square root computations, the functions of

```
Initialize to zero arrays forcex, forcey, forcez and coord
do i = 1, N − 1          (Two-body forces and coordinations loop)
    do j = i + 1, N
        Compute distance r_ij^2 = x_ij^2 + y_ij^2 + z_ij^2 between i and j
        if r_ij^2 < r_c^2 then
            Compute f = −φ'(r_ij)/r_ij
            forcex(i) = forcex(i) + f*x_ij
            forcey(i) = forcey(i) + f*y_ij
            forcez(i) = forcez(i) + f*z_ij
            forcex(j) = forcex(j) − f*x_ij
            forcey(j) = forcey(j) − f*y_ij
            forcez(j) = forcez(j) − f*z_ij
        endif
        if r_ij^2 < r_m^2 then
            Compute ρ_ij = ρ(r_ij)
            coord(i) = coord(i) + ρ_ij
            coord(j) = coord(j) + ρ_ij
        endif
    enddo
enddo
do i = 1, N              (Loop to evaluate and store U'(n_i))
    uderiv(i) = U'(coord(i))
enddo
do i = 1, N − 1          (Glue forces loop)
    do j = i + 1, N
        Compute distance r_ij^2 = x_ij^2 + y_ij^2 + z_ij^2 between i and j
        if r_ij^2 < r_m^2 then
            Compute g = −ρ'(r_ij)/r_ij
            f = g * ( uderiv(i) + uderiv(j) )
            forcex(i) = forcex(i) + f*x_ij
            forcey(i) = forcey(i) + f*y_ij
            forcez(i) = forcez(i) + f*z_ij
            forcex(j) = forcex(j) − f*x_ij
            forcey(j) = forcey(j) − f*y_ij
            forcez(j) = forcez(j) − f*z_ij
        endif
    enddo
enddo
```

Table A.1:
Algorithm for molecular dynamics glue forces calculation.

r are stored at constant intervals in r^2. A linear interpolation procedure between the values sampled in the tables is then used to evaluate the functions for a generic argument.

Actual code is slightly more complicated than that listed in Table A.1, owing to the implementation of Parrinello-Rahman motion equations (briefly discussed in Sec. A.3), and to neighbour-list handling (discussed in Sec. A.4).

A.3 MD at constant pressure

Recently, methods extending MD beyond the microcanonical ensemble have been developed. Among them, the isoenthalpic-isobaric (HPN) [58], isoenthalpic-isostress (HSN) [54,185], and the canonical ($T\Omega N$) [186] ensembles. Extension of MD to the grand canonical $T\Omega\mu$ ensemble remains an open problem.

The program used in the present work implements the $E\Omega N$, HPN and HSN ensembles. In the latter, the computational box, which is a generic parallelepiped, may vary in volume and in shape, driven by the instantaneous imbalance between the internal and the external stress. The advantages of this scheme, developed by Parrinello and Rahman [54], have been discussed in Sec. 3.1 (page 46).

In this method, the box is described by a 3×3 matrix $\mathbf{h}$, whose columns are the components of the three vectors $\vec{a}$, $\vec{b}$, $\vec{c}$ that span the edges of the box. Scaled coordinates $\vec{s}_i$ are introduced, such that the position of a particle $\vec{r}_i$ is written as

$$\vec{r}_i = \mathbf{h}\vec{s}_i$$

and the square distance between two particles as

$$r_{ij}^2 = (\vec{s}_i - \vec{s}_j)^T \mathbf{G} (\vec{s}_i - \vec{s}_j)$$

where the symbol T indicates transposition, and

$$\mathbf{G} \equiv \mathbf{h}^T \mathbf{h}$$

is the metric tensor in the new coordinate system. $\{\vec{s}_i\}$ and $\mathbf{h}$ are the $3N+9$ dynamical variables of the system, whose time evolution is given by the Lagrangian

$$\mathcal{L} = \frac{1}{2}m\sum_{i=1}^{N}\dot{\vec{s}}_i^{\,T}\mathbf{G}\dot{\vec{s}}_i - V(\vec{r}_1,\ldots,\vec{r}_N) + \frac{1}{2}W\,\mathrm{Tr}(\dot{\mathbf{h}}^T\dot{\mathbf{h}}) - p\Omega$$

where W is a constant parameter (controlling the inertia of the walls), p the external pressure, and $\Omega = \det \mathbf{h}$ the box volume. In case of an anisotropic external stress, $p\Omega$ is replaced by a more complex term.

When V is given by the glue expression (1.5), the equations of motion generated by $\mathcal{L}$ are

$$\ddot{\vec{s}}_i = -\mathbf{G}^{-1}\dot{\mathbf{G}}\dot{\vec{s}}_i - \frac{1}{m}\sum_{\substack{j=1\\(j\neq i)}}^{N}\frac{1}{r_{ij}}\Big(\phi'(r_{ij}) + [U'(n_i)+U'(n_j)]\rho'(r_{ij})\Big)\vec{s}_{ij}$$

$$\begin{aligned} W\ddot{h}^{\alpha\beta} &= m\sum_{i=1}^{N}\left(\mathbf{h}\dot{\vec{s}}_i\right)^{\alpha}\dot{s}_i^{\beta} \\ &\quad - \sum_{i=1}^{N}\sum_{j>i}\frac{1}{r_{ij}}\Big(\phi'(r_{ij}) + [U'(n_i)+U'(n_j)]\rho'(r_{ij})\Big)(\mathbf{h}\vec{s}_{ij})^{\alpha}s_{ij}^{\beta} \end{aligned}$$

where

$$\vec{s}_{ij} \equiv \vec{s}_i - \vec{s}_j$$

$$r_{ij}^2 = \vec{s}_{ij}^{\,T}\mathbf{G}\vec{s}_{ij}$$

$$n_i = \sum_{\substack{j=1\\(j\neq i)}}^{N}\rho(r_{ij})$$

The algorithm of Table A.1 can be easily modified accordingly.

Note that the forces depend upon both the positions and the velocities. The well-known Verlet (or leap-frog) integration algorithm [187] is not well suited to this situation, where positions and velocities must be *simultaneously* known. In the Verlet algorithm, in fact, knowledge of the positions at time $t+\Delta t$ (where Δt is the integration time step) is required to obtain the velocities at time t. For this reason, and for higher accuracy, a fifth-order (6-value, 1-step in the classification of Ref. [187]) predictor-corrector Gear integrator has been used instead. A good description of this algorithm can be found in Ref. [188].

A.4 Neighbour list on vector computers

In a simple force calculation algorithm (like that presented in Table A.1), all the $N(N-1)/2$ particle distances are computed at each time step. In systems with short-range interactions (such as the model for gold described in this thesis), when N is large, this constitutes a waste of time since only a minority of pairs are actually interacting.

Therefore, the performance of a MD program can be greatly improved by using bookkeeping mechanisms to keep track of the particle pairs which are close enough to interact. The usual method, invented by Verlet (see Ref. [188] and references therein), is the following. A list is made of the neighbours of each particle out to a distance $r_c + S$, where r_c is the interaction range and S a "skin" thickness. The formation of this list requires $O(N^2)$ time. For several time steps after that moment, only neighbours from the list are considered, and the force calculation runs in $O(N)$ time. The list is re-built when particle pairs excluded from the list may have moved within the interaction range.

Owing to the non-linear addressing of memory intrinsic in the list data structure, this technique inhibits vectorization of programs on recent vector computers such as the Cray X-MP or IBM 3090/VF, preventing an efficient utilization of such machines. A clever solution to this problem has been provided by Fincham and Ralston [189]. In their proposed algorithm for the formation of the neighbour list, shown in Table A.2, the non-linear access to memory is confined in a short and compact loop containing only integer arithmetics, while the distances are computed in a vectorized loop. This scheme leads to significant speed improvements on vector machines, and has been implemented in our program.

Once the neighbour list is formed, it has to be used for several time steps. Algorithms which compute the forces using the neighbour list are more difficult to vectorize efficiently. We have found the usual scalar algorithm, shown in Table A.3, to be the best choice in our case. In fact, the loop on the neighbours of particle i is very short ($\sim$ 10 iterations) when first-neighbour forces are used, as in the present glue

```
m = 1
marker(1) = 0
do i = 1, N − 1
    do j = i + 1, N
        Compute distance r²_ij = x²_ij + y²_ij + z²_ij between i and j
        index(j) = 0
        if r²_ij < r²_c then index(j) = 1
    enddo
    do j = i + 1, N
        list(m) = j
        m = m + index(j)
    enddo
    marker(i + 1) = m − 1
enddo
```

Table A.2:

Fincham-Ralston algorithm for the formation of the neighbour list. The first loop on j vectorizes. The second does not vectorize, but contains only a small amount of (integer) arithmetics.

```
do i = 1, N − 1
    do m = marker(i) + 1, marker(i + 1)
        j = list(m)
        Compute distance r²_ij = x²_ij + y²_ij + z²_ij between i and j
        Compute forces and/or coordinations and accumulate them
    enddo
enddo
```

Table A.3:

Conventional algorithm for force evaluation using the neighbour list. This algorithm does not vectorize.

model. Therefore, only a modest (if any) improvement could be achieved by vectorization (e.g., by use of gather/scatter operations as done in Ref. [189]). Moreover, since this algorithm takes $O(N)$ time, the total execution time becomes anyway dominated by the list formation when N is large.

Completely different strategies could perhaps lead to more efficient solutions to the force evaluation problem in molecular dynamics. Vectorizing MD algorithms for short-range forces which scale as N have been recently proposed [190]. Implementation of such algorithms in production programs could make practical simulations in the size range $N \sim 10^4$–10^6, allowing new kinds of physical problems to be attacked by computer simulation.

Bibliography

[1] A. A. Maradudin, in *Dynamical properties of solids*, Volume 1, ed. by G. K. Horton and A. A. Maradudin (North-Holland, Amsterdam, 1974), p. 1.

[2] R. Car and M. Parrinello, *Phys. Rev. Lett.* **55**, 2471 (1985); *Solid St. Commun.* **62**, 403 (1987).

[3] Parts of the results presented in this thesis can also be found in Refs. [34] (glue model); [33,89] (Au(100)); [110] (Au(110)); [131,132] (Au(111)); [84] (Au surface reconstructions); [148] (melting behaviour of Au(111)); [66] (vacancy); [182] (Au clusters).

[4] J. A. Barker, in *Rare gas solids* Volume I, ed. by M. L. Klein and J. A. Venables (Academic, London, 1976).

[5] V. Heine, in *Solid State Physics*, Volume 24, ed. by H. Ehrenreich, F. Seitz and D. Turnbull (Academic, New York, 1970), p. 1; M. L. Cohen and V. Heine, *ibid.*, p. 38.

[6] See, e.g., R. Taylor, *Physica* **131B**, 103 (1985), and references therein.

[7] V. Heine, in *Solid State Physics*, Volume 35, ed. by H. Ehrenreich, F. Seitz and D. Turnbull (Academic, New York, 1980), p. 1.

[8] D. G. Pettifor, in *Physical metallurgy*, ed. by R. W. Cahn and P. Haasen (North Holland, Amsterdam, 1983), Chapter 3.

[9] C. Kittel, *Introduction to solid state physics*, 3rd ed. (Wiley, New York, 1966).

[10] A. R. Ubbelohde, *The molten state of matter* (Wiley, Chichester, 1978).

[11] C. S. Jayanthi, E. Tosatti and A. Fasolino, *Phys. Rev. B* **31**, 470 (1985).

[12] A. J. C. Ladd and L. V. Woodcock, *Molec. Phys.* **36**, 611 (1978).

[13] G. Jacucci, in *Diffusion in crystalline solids*, ed. by G. E. Murch and A. S. Nowick (Academic, New York, 1984), Chapter 8.

[14] A. V. Chadwick and H. R. Glyde, in *Rare gas solids* Volume II, ed. by M. L. Klein and J. A. Venables (Academic, London, 1977).

[15] A. van den Beukel, in *Vacancies and interstitials in metals*, ed. by A. Seeger, D. Schumacher, W. Schilling and J. Diehl (North-Holland, Amsterdam, 1970), p. 427.

[16] R. Feder and A. S. Nowick, *Phil. Mag.* **15**, 805 (1967).

[17] A. Seeger and H. Mehrer, in *Vacancies and interstitials in metals*, ed. by A. Seeger, D. Schumacher, W. Schilling and J. Diehl (North-Holland, Amsterdam, 1970), p. 1.

[18] Ya. A. Kraftmakher and P. G. Strelkov, in *Vacancies and interstitials in metals*, ed. by A. Seeger, D. Schumacher, W. Schilling and J. Diehl (North-Holland, Amsterdam, 1970), p. 59.

[19] M. Born and K. Huang, *Dynamical theory of crystal lattices* (Oxford University Press, Oxford, 1954), chapter III.

[20] H. B. Huntington, in *Solid State Physics*, Volume 7, ed. by F. Seitz and D. Turnbull (Academic, New York, 1958).

[21] P. Korpiun and E. Luscher, in *Rare gas solids* Volume II, ed. by M. L. Klein and J. A. Venables (Academic, London, 1977).

[22] R. Benedek, *J. Phys. F* **8**, 1119 (1978).

[23] R. P. Gupta, *Phys. Rev. B* **23**, 6265 (1981).

[24] G. De Lorenzi and G. Jacucci, *Surf. Sci.* **164**, 526 (1985).

[25] F. Jona, *J. Phys. C* **11**, 4271 (1978).

[26] M. W. Finnis and V. Heine, *J. Phys. F* **4**, L37 (1974).

[27] A. Fasolino, G. Santoro and E. Tosatti, *Phys. Rev. Lett.* **44**, 1684 (1980); *Surf. Sci.* **125**, 317 (1983).

[28] J. Q. Broughton and L. V. Woodcock, *J. Phys. C* **11**, 2743 (1978).

[29] F. Ercolessi, Tesi di Laurea, University of Trieste (1983).

[30] R. A. Johnson, *J. Phys. F* **3**, 295 (1973), and references therein.

[31] M. W. Finnis, invited lecture at the *NATO Advanced Research Workshop on the Chemistry and Physics of Fracture*, Bad Reichenhall (1986).

[32] P. Wynblatt, *Surf. Sci.* **136**, L51 (1984).

[33] F. Ercolessi, E. Tosatti and M. Parrinello, *Phys. Rev. Lett.* **57**, 719 (1986).

[34] F. Ercolessi, M. Parrinello and E. Tosatti, *Phil. Mag.*, to appear.

[35] M. Garofalo, Magister Philosophiae thesis, International School for Advanced Studies, Trieste (1984).

[36] M. W. Finnis and J. E. Sinclair, *Phil. Mag. A* **50**, 45 (1984); erratum: *Phil. Mag. A* **53**, 161 (1986); G. J. Ackland and R. Thetford, *Phil. Mag. A* **56**, 15 (1987).

[37] G. Allan, in *Handbook of surfaces and interfaces*, Volume 1, ed. by L. Dobrzynski (Garland, New York, 1978), p. 299, and references therein.

[38] M. S. Daw and M. I. Baskes, *Phys. Rev. Lett.* **50**, 1285 (1983); *Phys. Rev. B* **29**, 6443 (1984).

[39] S. M. Foiles, *Phys. Rev. B* **32**, 3409 (1985); S. M. Foiles, M. I. Baskes and M. S. Daw, *Phys. Rev. B* **33**, 7983 (1986).

[40] M. J. Stott and E. Zaremba, *Phys. Rev. B* **22**, 1564 (1980).

[41] J. K. Nørskov, *Phys. Rev. B* **26**, 2875 (1982).

[42] E. Clementi and C. Roetti, *At. Data Nucl. Data Tables* **14**, 177 (1974); A. D. McLean and R. S. McLean, *At. Data Nucl. Data Tables* **26**, 197 (1981).

[43] K. W. Jacobsen, J. K. Nørskov and M. J. Puska, *Phys. Rev. B* **35**, 7423 (1987).

[44] K. Fuchs, *Proc. Roy. Soc.* **A153**, 622 (1936); **A157**, 444 (1936).

[45] R. A. Johnson, *Phys. Rev. B* **6**, 2094 (1972).

[46] D. Castiel, L. Dobrzynski and D. Spanjaard, *Surf. Sci.* **59**, 252 (1976).

[47] V. Bortolani and G. Santoro, in *Proc. of the Second Int. Conf. on Phonon Physics*, ed. by J. Kollar, N. Kroo, N. Menyhard and T. Siklos (World Scientific, Singapore, 1985), p. 566.

[48] A. R. Miedema, *Z. Metallk.* **69**, 287 (1978).

[49] J. W. Lynn, H. G. Smith and R. M. Nicklow, *Phys. Rev. B* **8**, 3493 (1973).

[50] W. B. Pearson, *A handbook of lattice spacings and structures of metals and alloys*, Volume 2 (Pergamon Press, Oxford, 1967), p. 648; the data set used is that of H. Warlimont, *Z. Metallk.* **50**, 708 (1959).

[51] R. P. Sahu, K. C. Jain and R. W. Siegel, *J. Nucl. Mat.* **69 & 70**, 264 (1978).

[52] J. R. Neighbours and G. A. Alers, *Phys. Rev.* **111**, 707 (1958).

[53] *Am. Inst. of Phys. Handbook*, 3rd ed. (McGraw-Hill, New York, 1972).

[54] M. Parrinello and A. Rahman, *Phys. Rev. Lett.* **45**, 1196 (1980); *J. Appl. Phys.* **52**, 7182 (1981); in Ref. [55], p. 204.

[55] *Molecular-dynamics simulation of statistical-mechanical systems*, Proc. of the Int. School "Enrico Fermi", Course XCVII, Varenna, 1985, ed. by G. Ciccotti and W. G. Hoover (North-Holland, Amsterdam, 1986).

[56] M. Parrinello, A. Rahman and P. Vashishta, *Phys. Rev. Lett.* **50**, 1073 (1983).

[57] J. Q. Broughton and G. H. Gilmer, *J. Chem. Phys.* **79**, 5095 (1983).

[58] H. C. Andersen, *J. Chem. Phys.* **72**, 2384 (1980).

[59] see, e.g., C. A. Croxton, *Liquid state physics* (Cambridge University Press, 1974), Chapter 5.

[60] N. H. Nachtrieb, in Proc. Second Int. Conf. on *The properties of liquid metals*, Tokyo, 1972 (Taylor & Francis, London, 1973), p. 521.

[61] M. Shimoji and T. Itami, *Atomic transport in liquid metals* (Trans Tech, Switzerland, 1986), Chapter 3.

[62] C. J. Smithells, *Metal reference book*, 5th Edition (Butterworths, London, 1976).

[63] Y. Waseda, *The structure of non-crystalline materials* (McGraw-Hill, Toronto, 1980), p. 276.

[64] A. D. Franklin, in *Point defects in solids*, Volume 1, Ed. by J. H. Crawford, Jr., and L. M. Slifkin (Plenum Press, New York, 1972), p. 1.

[65] N. L. Peterson, *Comments Sol. State Phys.* **8**, 107 (1978); *J. Nucl. Mat.* **69** & **70**, 3 (1978).

[66] G. De Lorenzi and F. Ercolessi, in preparation.

[67] A. M. Stoneham, *Theory of defects in solids* (Clarendon Press, Oxford, 1975), Chapter 8.

[68] J. Friedel, in *Vacancies and interstitials in metals*, ed. by A. Seeger, D. Schumacher, W. Schilling and J. Diehl (North-Holland, Amsterdam, 1970), p. 787.

[69] A. Schoen, *Phys. Rev. Lett.* **1**, 138 (1958).

[70] K. Tharmalingam and A. B. Lidiard, *Phil. Mag.* **4**, 899 (1959).

[71] K. Compaan and Y. Haven, *Trans. Faraday Soc.* **52**, 786 (1956); *Trans. Faraday Soc.* **54**, 1498 (1958).

[72] G. H. Vineyard, *J. Phys. Chem. Solids* **3**, 121 (1957).

[73] J. G. Mullen, *Phys. Rev.* **121**, 1649 (1961).

[74] A. D. LeClaire, *Phil. Mag.* **14**, 1271 (1966).

[75] C. P. Flynn, *Phys. Rev. Lett.* **35**, 1721 (1975).

[76] C. Herzig, H. Eckseler, W. Bussmann and D. Cardis, *J. Nucl. Mat.* **69** & **70**, 61 (1978).

[77] M. A. Van Hove, R. J. Koestner, P. C. Stair, J. P. Bibérian, L. L. Kesmodel, I. Bartoš and G. A. Somorjai, *Surf. Sci.* **103**, 189; 218 (1981).

[78] D. G. Fedak and N. A. Gjostein, *Phys. Rev. Lett.* **16**, 171 (1966); *Surf. Sci.* **8**, 77 (1967); *Acta Met.* **15**, 827 (1967).

[79] A. M. Mattera, R. M. Goodman and G. A. Somorjai, *Surf. Sci.* **7**, 26 (1967).

[80] P. W. Palmberg and T. N. Rhodin, *Phys. Rev.* **161**, 586 (1967); *J. Chem. Phys.* **49**, 134 (1968).

[81] V. Heine and L. D. Marks, *Surf. Sci.* **165**, 65 (1986).

[82] D. Tománek and K. H. Bennemann, *Surf. Sci.* **163**, 503 (1985).

[83] K.-P. Bohnen and K. M. Ho, (to be published); J. W. Davenport and M. Weinert, *Phys. Rev. Lett.* **58**, 1382 (1987).

[84] F. Ercolessi, A. Bartolini, M. Garofalo, M. Parrinello and E. Tosatti, *Physica Scripta*, in press.

[85] D. M. Zehner, B. R. Appleton, T. S. Noggle, J. W. Miller, J. H. Barrett, L. H. Jenkins and O. E. Schow III, *J. Vac. Sci. Technol.* **12**, 454 (1975).

[86] J. F. Wendelken and D. M. Zehner, *Surf. Sci.* **71**, 178 (1978).

[87] K. H. Rieder, T. Engel, R. H. Swendsen and M. Manninen, *Surf. Sci.* **127**, 223 (1983).

[88] G. K. Binnig, H. Rohrer, Ch. Gerber and E. Stoll, *Surf. Sci.* **144**, 321 (1984).

[89] F. Ercolessi, M. Parrinello and E. Tosatti, *Surf. Sci.* **177**, 314 (1986).

[90] P. Bak, *Rept. Progr. Phys.* **45**, 587 (1982).

[91] W. Moritz, Habilitationsschrift, University of Munich (1983).

[92] W. Moritz and D. Wolf, *Surf. Sci.* **88**, L29 (1979).

[93] J. R. Noonan and H. L. Davis, *J. Vac. Sci. Technol.* **16**, 587 (1979).

[94] K. H. Rieder, T. Engel and N. Garcia, in: Proc. 4th Intern. Conf. Solid Surfaces and 3rd European Conf. on Surface Science, Cannes, 1980 [Suppl. Le Vide, *Les Couches Minces* **201**, 861 (1980)].

[95] B. Reihl and B. I. Dunlap, *Appl. Phys. Lett.* **37**, 941 (1981).

[96] N. Müller, M. Erbüdak and D. Wolf, *Sol. St. Commun.* **39**, 1247 (1981).

[97] S. H. Overbury, W. Heiland, D. M. Zehner, S. Datz and R. S. Thoe, *Surf. Sci.* **109**, 239 (1981).

[98] M. Manninen, J. K. Nørskov and C. Umrigar, *Surf. Sci.* **119**, L393 (1982).

[99] D. P. Jackson, T. E. Jackman, J. A. Davies, W. N. Unertl and P. D. Norton, *Surf. Sci.* **126**, 226 (1983).

[100] G. Binnig and H. Rohrer, *Surf. Sci.* **126**, 236 (1983); G. Binnig, H. Rohrer, Ch. Gerber and E. Weibel, *Surf. Sci.* **131**, L379 (1983).

[101] I. K. Robinson, *Phys. Rev. Lett.* **50**, 1145 (1983).

[102] L. D. Marks, *Phys. Rev. Lett.* **51**, 1000 (1983); *Surf. Sci.* **139**, 281 (1984). See also J. M. Gibson, *Phys. Rev. Lett.* **53**, 1859 (1984).

[103] Y. Kuk, L. C. Feldman and I. K. Robinson, *Surf. Sci* **138**, L168 (1984).

[104] R. J. Culbertson, J. H. Barrett and S. P. Withrow, *Surf. Sci.* **157**, 451 (1985); S. P. Withrow, J. H. Barrett and R. J. Culbertson, *Surf. Sci.* **161**, 584 (1985).

[105] W. Moritz and D. Wolf, *Surf. Sci.* **163**, L655 (1985).

[106] H. Hemme and W. Heiland, *Nucl. Instrum. Methods B* **9**, 41 (1985); J. Möller, H. Niehus and W. Heiland, *Surf. Sci.* **166**, L111 (1986); J. Möller, K. J. Snowdon, W. Heiland and H. Niehus, *Surf. Sci.* **178**, 475 (1986).

[107] M. Copel and T. Gustafsson, *Phys. Rev. Lett.* **57**, 723 (1986); M. Copel, P. Fenter and T. Gustafsson, *J. Vac. Sci. Technol. A* **5**, 742 (1987).

[108] H. P. Bonzel, N. Freyer and E. Preuss, *Phys. Rev. Lett.* **57**, 1024 (1986).

[109] K. W. Jacobsen and J. K. Nørskov, preprint (1987).

[110] M. Garofalo, E. Tosatti and F. Ercolessi, *Surf. Sci.*, in press (1987).

[111] H. P. Bonzel and S. Ferrer, *Surface Sci.* **118**, L263 (1982).

[112] T. Halicioğlu, T. Takai and W. A. Tiller, in *The structure of surfaces*, ed. by M. A. Van Hove and S. Y. Tong, Springer Series in Surface Sciences Vol. 2 (Springer Verlag, Berlin, 1985), p. 231.

[113] H.-J. Brocksch and K. H. Bennemann, *Surf. Sci.* **161**, 321 (1985).

[114] K. H. Rieder, private communication.

[115] D. Wolf, H. Jagodzinski and W. Moritz, *Surface Sci.* **77**, 265, 283 (1978).

[116] J. C. Campuzano, M. S. Foster, G. Jennings, R. F. Willis and W. Unertl, *Phys. Rev. Lett.* **54**, 2684 (1985); J. C. Campuzano, G. Jennings and R. F. Willis, *Surface Sci.* **162**, 484 (1985).

[117] H. Derks, J. Möller and W. Heiland, *Surf. Sci.* **188**, L685 (1987).

[118] A. Morgante, K. C. Prince, G. Paolucci and E. Tosatti, Proc. 9th European Conf. on Surface Science, Luzern, 1987, to appear in *Surf. Sci.*

[119] M. S. Daw, *Surf. Sci.* **166**, L161 (1986).

[120] C. Y. Weng, R. B. Griffiths and M. E. Fisher, *Phys. Rev.* **162**, 475 (1967).

[121] N. Freyer and H. P. Bonzel, *Surface Sci.* **160**, L501 (1985).

[122] J. Perdereau, J. P. Bibérian and G. E. Rhead, *J. Phys. F* **4**, 798 (1974).

[123] D. M. Zehner and J. F. Wendelken, Proc. 7th Intern. Vac. Congr. and 3rd Intern. Conf. Solid Surfaces, Vienna, 1977, ed. by R. Dobrozemsky *et al.* (F. Berger and Söhne, Vienna, 1977), p. 517.

[124] H. Melle and E. Menzel, *Z. Naturforsch.* **33a**, 282 (1978).

[125] J. C. Heyraud and J. J. Métois, *Surf. Sci.* **100**, 519 (1980).

[126] Y. Tanishiro, H. Kanamori, K. Takayanagi, K. Yagi and G. Honjo, *Surf. Sci.* **111**, 395 (1981).

[127] K. Takayanagi and K. Yagi, *Trans. Jpn. Inst. Met.* **24**, 337 (1983).

[128] L. D. Marks and D. J. Smith, *Surf. Sci.* **143**, 495 (1984).

[129] U. Harten, A. M. Lahee, J. P. Toennies and Ch. Wöll, *Phys. Rev. Lett.* **54**, 2619 (1985).

[130] W. J. Kaiser and R. C. Jaklevic, *Surf. Sci.* **182**, L227 (1987).

[131] A. Bartolini, F. Ercolessi and E. Tosatti, Proc. 2nd Int. Conf. on the Structure of Surfaces, Amsterdam, 1987, ed. by J. F. van der Veen and M. A. Van Hove (Springer, in press).

[132] A. Bartolini, Magister Philosophiae thesis, International School for Advanced Studies, Trieste (1986).

[133] Y. Okwamoto and K. H. Bennemann, *Surf. Sci.* **186**, 511 (1987).

[134] X. Q. Wang, G. L. Chiarotti, F. Ercolessi and E. Tosatti, to be published; X. Q. Wang, Magister Philosophiae thesis, International School for Advanced Studies, Trieste (1987).

[135] D. Nenow, in *Progress in Crystal Growth and Characterization* **9**, 185, Ed. by B. R. Pamplin (Pergamon, Oxford, 1984), and references therein.

[136] L. Pietronero and E. Tosatti, *Sol. St. Comm.* **32**, 255 (1979).

[137] A. Trayanov and E. Tosatti, *Phys. Rev. Lett.*, to appear (1987); A. Trayanov and E. Tosatti, Proc. 2nd Int. Conf. on the Structure of Surfaces, Amsterdam, 1987, ed. by J. F. van der Veen and M. A. Van Hove (Springer, in press).

[138] J. W. M. Frenken and J. F. van der Veen, *Phys. Rev. Lett.* **54**, 134 (1985); J. W. M. Frenken, P. M. J. Marée, and J. F. van der Veen, *Phys. Rev. B* **34**, 7506 (1986); B. Pluis, A. W. D. Gon, J. W. M. Frenken and J. F. van der Veen, preprint (1987).

[139] E. Tosatti, Proc. 2nd Int. Conf. on the Structure of Surfaces, Amsterdam, 1987, ed. by J. F. van der Veen and M. A. Van Hove (Springer, in press).

[140] R. E. Allen, F. W. De Wette, and A. Rahman, *Phys. Rev.* **179**, 887 (1969).

[141] J. Q. Broughton and G. H. Gilmer, *J. Chem. Phys.* **79**, 5105, 5119 (1983).

[142] V. Rosato, G. Ciccotti and V. Pontikis, *Phys. Rev. B* **33**, 1860 (1986); V. Pontikis and V. Rosato, *Surf. Sci.* **162**, 150 (1985).

[143] S. Valkealahti and R. M. Nieminen, *Physica Scripta* **36**, 646 (1987).

[144] C. S. Jayanthi, E. Tosatti, and L. Pietronero, *Phys. Rev. B* **31**, 3456 (1985).

[145] D. M. Zhu and J. G. Dash, *Phys. Rev. Lett.* **57**, 2959 (1986).

[146] J. W. M. Frenken, F. Huussen, and J. F. van der Veen, *Phys. Rev. Lett.* **58**, 401 (1987).

[147] A. C. Levi and E. Tosatti, *Surf. Sci.* **178**, 425 (1986).

[148] P. Carnevali, F. Ercolessi and E. Tosatti, *Phys. Rev. B* **36**, in press (1987).

[149] E. G. McRae and R. A. Malic, *Phys. Rev. Lett.* **58**, 1437 (1987).

[150] *Elemental and compound clusters* (Erice Summer School), ed. by T. P. Martin and G. Benedek (Springer, in press).

[151] *Microclusters*, *Proc. 1st NEC Symposium on fundamental approaches to new material phases*, Hakone and Kawasaki, 1986, ed. by S. Sugano, Y. Nishina and S. Ohnishi (Springer, Berlin, 1987).

[152] I. D. Morokhov, V. I. Petinov, L. I. Trusov and V. F. Petrunin, *Sov. Phys. Usp.* **24**, 295 (1981).

[153] A. Balerna, E. Bernieri, P. Picozzi, A. Reale, S. Santucci, E. Burattini and S. Mobilio, *Phys. Rev. B* **31**, 5058 (1985); *Surf. Sci.* **156**, 206 (1985).

[154] J. Harada and K. Ohshima, *Surf. Sci.* **106**, 51 (1981).

[155] C. Solliard, *Surf. Sci.* **106**, 58 (1981); C. Solliard and M. Flueli, *Surf. Sci.* **156**, 487 (1985).

[156] L. D. Marks and D. J. Smith, *J. Crystal Growth* **54**, 425 (1981); D. J. Smith and L. D. Marks, *J. Crystal Growth* **54**, 433 (1981).

[157] L. R. Wallenberg, J.-O. Bovin and G. Schmid, *Surf. Sci.* **156**, 256 (1985); J.-O. Bovin, L. R. Wallenberg and D. J. Smith, *Nature* **317**, 47 (1985).

[158] S. Iijima and T. Ichihashi, *Phys. Rev. Lett.* **56**, 616 (1986).

[159] S. Iijima, in Ref. [151], p. 186.

[160] P. Gao and H. Gleiter (preprint).

[161] M. Flueli, R. Sommer, P. Stadelmann and Ph. Buffat, *Helv. Phys. Acta* **60**, 799 (1987).

[162] K. Sattler (to be published).

[163] I. Katakuse, T. Ichihara, Y. Fujita, T. Matsuo, T. Sakurai and H. Matsuda, *Int. J. Mass Spectrom. Ion Processes* **67**, 229 (1985).

[164] S. Ino, *J. Phys. Soc. Japan* **27**, 941 (1969).

[165] L. D. Marks, *Phil. Mag. A* **49**, 81 (1984); A. Howie and L. D. Marks, *Ibid.*, **49**, 95 (1984).

[166] J. C. Heyraud and J. J. Métois, *Acta Metall.* **28**, 1789 (1980).

[167] P. S. Bagus, C. J. Nelin and C. W. Bauschlicher, Jr. *Surf. Sci.* **156**, 615 (1985); M. H. McAdon and W. A. Goddard III, *Phys. Rev. Lett.* **55**, 2563 (1985); G. Pacchioni and J. Koutecký, *J. Chem. Phys.* **84**, 3301 (1986); K. Raghavachari, *J. Chem. Phys.* **84**, 5672 (1986); T. H. Upton, *J. Chem. Phys.* **86**, 7054 (1987); I. Boustani, W. Pewestorf, P. Fantucci, V. Bonačić-Koutecký and J. Koutecký, *Phys. Rev. B* **35**, 9437 (1987); C. W. Bauschlicher, Jr., and L. G. M. Pettersson, *J. Chem. Phys.* **84**, 2226 (1986).

[168] B. Delley, D. E. Ellis, A. J. Freeman, E. J. Baerends and D. Post, *Phys. Rev. B* **27**, 2132 (1983).

[169] J. L. Martins, L. Buttet and R. Car, *Phys. Rev. B* **31**, 1804 (1985).

[170] W. Andreoni and J. L. Martins, *Surf. Sci.* **156**, 635 (1985).

[171] D. Tománek and M. A. Schlüter, *Phys. Rev. B* **36**, 1208 (1987).

[172] R. Car, M. Parrinello and W. Andreoni, in Ref. [151], p. 134; W. Andreoni and P. Ballone, *Physica Scripta*, (in press); P. Ballone, W. Andreoni, R. Car and M. Parrinello (preprint).

[173] D. Hohl, R. O. Jones, R. Car and M. Parrinello, *Chem. Phys. Lett.* **139**, 540 (1987).

[174] S. N. Khanna, J. P. Bucher, J. Buttet and F. Cyrot-Lackmann, *Surf. Sci.* **127**, 165 (1983).

[175] D. Tománek, S. Mukherjee and K. H Bennemann, *Phys. Rev. B* **28**, 665 (1983); erratum: *Phys. Rev. B* **29**, 1076 (1984).

[176] F. Casula, W. Andreoni and K. Maschke, *J. Phys. C* **19**, 5155 (1986).

[177] J. Farges, M. F. de Feraudy, B. Raoult and G. Torchet, *J. Chem. Phys.* **78**, 5067 (1983); *J. Chem. Phys.* **84**, 3491 (1986).

[178] T. L. Beck, J. Jellinek and R. S. Berry, *J. Chem. Phys.* **87**, 545 (1987), and references therein.

[179] J. Diefenbach and T. P. Martin, *J. Chem. Phys.* **83**, 4585 (1985).

[180] R. Biswas and D. R. Hamann, *Phys. Rev. B* **34**, 895 (1986); E. Blaisten-Barojas and D. Levesque, *Phys. Rev. B* **34**, 3910 (1986); B. P. Feuston, R. K. Kalia and P. Vashishta, *Phys. Rev. B* **35**, 6222 (1987).

[181] L. Marville and W. Andreoni, *J. Phys. Chem.* **91**, 2645 (1987).

[182] W. Andreoni, F. Ercolessi and E. Tosatti, in preparation.

[183] P. A. Montano, G. K. Shenoy, E. E. Alp, W. Schulze and J. Urban, *Phys. Rev. Lett.* **56**, 2076 (1986).

[184] M. R. Hoare and J. A. McInnes, *Adv. Phys.* **32**, 791 (1983).

[185] S. Nosé and M. L. Klein, *Mol. Phys.* **50**, 1055 (1983).

[186] S. Nosé, *Mol. Phys.* **52**, 255 (1984); *J. Chem. Phys.* **81**, 511 (1984).

[187] H. J. C. Berendsen and W. F. van Gunsteren, in Ref. [55], p. 43.

[188] A. Rahman, in *Correlation functions and quasiparticle interactions in condensed matter*, NATO Advanced Study Institutes Series B, Vol. 35 (Plenum Press, New York, 1978), p. 417.

[189] D. Fincham and B. J. Ralston, *Comput. Phys. Commun.* **23**, 127 (1981).

[190] J. Boris, *J. Comput. Phys.* **66**, 1 (1986).

Acknowledgements

I wish to express my gratitude to Erio Tosatti and Michele Parrinello for suggesting the "glue" idea and constantly supporting this project throughout the period 1983–1987.

A substantial part of the material included in this thesis comes from work done in collaboration with Wanda Andreoni, Anna Bartolini, Paolo Carnevali, Giulia De Lorenzi and Mario Garofalo. I am grateful to them and to all the other people who have contributed ideas and helped to complete this work.

I thank the IBM Zürich Research Laboratory and the IBM Scientific Center in Rome for their hospitality and availability of computer time, and Alvise Nobile and his staff for their generous help in solving computer problems.

Part of the computations were carried out under the SISSA-CINECA joint project, sponsored by the Italian Ministry of Education.